Channel Modelling for Visible Light Communication Systems

by

Ahmed A. Abdulhussain Al-Kinani

A thesis submitted in partial fulfilment for the degree of Doctor of Philosophy

at

Heriot-Watt University
School of Engineering and Physical Sciences

February 2018

Abstract

Visible Light Communications (VLCs) have been identified as a potential solution for mitigating the looming Radio Frequency (RF) spectrum crisis. Having the ability to provide illumination and communication at the same time, this technology has been considered as one of the most promising communication technologies for future wireless networks. VLCs are a viable candidate for short-range indoor applications with very high data rates. In terms of outdoor applications, Vehicular VLCs (VVLCs) play an important role in vehicular ad hoc networks and Intelligent Transportation Systems (ITS). Adopting visible light in vehicular networks offers a great potential to enhance road safety and traffic efficiency towards accident-free driving. For the sake of VLC system design and performance evaluation, it is indispensable to develop accurate, efficient, and flexible channel models, which can fully reflect the characteristics of VLC channels.

In this thesis, we first give a comprehensive and up-to-date literature review of the most important indoor Optical Wireless Communications (OWCs) measurement campaigns and channel models, primarily for Wireless Infrared Communications (WIRCs) and VLCs. Consequently, we can identify that an appropriate channel model for VLC systems is currently missing in the literature. This Ph.D. project is therefore devoted to the modelling of VLC channels for both indoor and outdoor communication systems.

Second, a new Two-Dimensional (2D) stationary Field of View (FoV) one-ring Regular-Shape Geometry Based Stochastic Model (RS-GBSM) for VLC Single-Input Single-Output (SISO) channels is proposed. The proposed model considers the Line-of-Sight (LoS) and Single-Bounce (SB) components. VLC channel characteristics are analysed based on different positions of the Photodetector (PD) and FoV constraint.

Third, we propose a new 2D stationary multiple-bounce RS-GBSM for VLC SISO channels. The proposed model employs a combined two-ring and confocal ellipse model. This model is sufficiently generic and adaptable to a variety of indoor scenarios since the received signal is constructed as the summation of the LoS, SB, Double-Bounce (DB), and Triple-Bounce (TB) rays with different powers.

Fourth, a new 2D mobile RS-GBSM for vehicular VLC SISO channels is proposed. The proposed model combines a two-ring model and a confocal ellipse model, and considers SB and DB components in addition to LoS component. Unlike conventional

models, the proposed model considers the light that is reflected off moving vehicles around the Transmitter (Tx) and Receiver (Rx), as well as the light that is reflected off the stationary roadside environments. Vehicular VLC channel characteristics are analysed along different distance ranges between 0 and 70 m and different PD heights.

Fifth, we propose a novel Three-Dimensional (3D) mobile RS-GBSM for vehicular VLC Multiple-Input Single-Output (MISO) channels. The proposed model combines two-sphere and elliptic-cylinder models. Both the LoS component and SB components, which are reflected off moving vehicles and stationary roadside environments, are considered. The proposed 3D RS-GBSM has the ability to study the impact of the vehicular traffic density on the received power and jointly considers the azimuth and elevation angles by using the von Mises-Fisher (VMF) distribution.

In summary, this work proposes new realistic VLC channel models which are useful for the design, test, and performance evaluation of advanced indoor and outdoor VLC systems. Furthermore, it identifies important directions that can be considered in future research, and helps propose new applications that require the development of more realistic channel models before the actual implementation.

To the loving memory of my parents may Allah bless their souls and make our remembrance of them a means for their forgiveness

To my beloved wife Wijdan, who loves me and supports me in every turn of my life

To my lovely kids, Fatima, Ali, and Mohammed who are the true joy of my life

To my brother and sisters who have been always by my side

Acknowledgments

First of all, I thank Allah almighty for giving me strength and ability to complete this study. I would also like to express my special appreciation and thanks to the Republic of Iraq, represented by the Ministry of Higher Education and Scientific Research (MOHESR) and Ministry of Communications (MoC) for their sponsorship and support of my study.

I would like to gratefully acknowledge the distinguished supervision of Prof. Cheng-Xiang Wang for all the useful advice, expert knowledge, guidance and patience without which this work would not have materialised. My special thanks goes to my second supervisor, Prof. Harald Haas, from the University of Edinburgh, for his insightful discussions and invaluable support.

I am also deeply thankful to all my colleagues and friends in the Advanced Wireless Technologies (AWiTec) Lab, namely, Shangbin Wu, Ammar Ghazal, Rui Feng, Yu Liu, Qiuming Zhu, Yu Fu, Carlos Lopez, Li Zhou, Qianru Zhou, Jia Wang, Yi Tan, and Xiaojuan Yan, who are travelling alongside me on my Ph.D. journey, shared my struggles, provided laughter when it was most needed and special thanks to Fourat Haider who helped me throughout this study.

Lastly, and most importantly, I am forever indebted to my wife Wijdan for her tireless support, patience, and love.

Ahmed Al-Kinani
Edinburgh, February 2018.

Declaration of Authorship

I, Ahmed A. Abdulhussain Al-Kinani, declare that this thesis titled, 'Channel Modelling for Visible Light Communication Systems' and the work presented in it are my own. I confirm that:

- This work was done wholly while in candidature for a research degree at Heriot-Watt University.
- Where I have consulted the published work of others, this is always clearly attributed.
- Where I have quoted from the work of others, the source is always given. With the exception of such quotations, this thesis is entirely my own work.
- I have acknowledged all main sources of help.
- Where the thesis is based on work done by myself jointly with others, I have made clear exactly what was done by others and what I have contributed myself.

Signed: _____

Date: _____

Contents

List of Figures

List of Tables

Abbreviations

2D	Two-Dimensional
3D	Three-Dimensional
4G	Fourth Generation
5G	Fifth Generation
AAoA	Azimuth Angle of Arrival
AAoD	Azimuth Angle of Departure
AC	Alternating Current
ACF	Autocorrelation Function
ADC	Analog-to-Digital Converter
AoA	Angle of Arrival
AoD	Angle of Departure
AoS	Angle of Scattering
ASE	Area Spectral Efficiency
AUVs	Autonomous Underwater Vehicles
AWGN	Additive White Gaussian Noise
BC	Before Christ
BER	Bit Error Rate
BRDF	Bidirectional Reflectance Distribution Function
BS	Base Station

CBM	Ceiling Bounce Model
CDF	Cumulative Distribution Function
CFP	Call for Proposals
CIR	Channel Impulse Response
CvM	Cramér-von Mises
DAC	Digital-to-Analog Converter
DB	Double-Bounce
DC	Direct Current
DFT	Discrete Fourier Transform
DLoS	Directed LoS
DRLs	Daytime Running Lights
DSP	Digital Signal Processor
DSRC	Dedicated Short Range Communications
EM	Electromagnetic Spectrum
EMEDS	Extended Method of Exact Doppler Spread
EUV	Extreme Ultraviolet
F2F	Fixed-to-Fixed
F2M	Fixed-to-Mobile
FCC	Federal Communications Commission
FO	Frequency Offset
FoV	Field of View
FSONA	Free Space Optical Networking Architecture
GBDM	Geometry-Based Deterministic Models
GBSM	Geometry-Based Stochastic Models
GO	Geometrical Optics
GPS	Global Positioning System

IARC	International Agency for Research on Cancer
IBM	International Business Machines
IoAT	Internet of Aircraft Things
IR	Infrared
IRED	Infrared LED
IrSimIt	Infrared impulse response Simulator by Iteration
IS	Integrating Sphere
ISI	Intersymbol Interference
ITS	Intelligent Transportation Systems
LED-ID	LED-Identification
LEDs	Light-Emitting Diodes
Li-Cell	Light-Cell
Li-Fi	Light Fidelity
LOS	Line-of-Sight
LoS	Line-of-Sight
LSD	Light Shape Diffuser
LSH	Left-Side Headlight
LTE	Long-Term Evolution
LTE-A	LTE-Advanced
LTI	Linear Time-Invariant
M2M	Mobile-to-Mobile
MCA	Monte Carlo algorithm
MCBM	Modified CBM
MEV	Method of Equal Volume
MGD	Modified Gamma Distribution
MISO	Multiple-Input Single-Output
MIT	Massachusetts Institute of Technology
MMCA	Modified MCA
mmWave	Milli-meter Wave

MRD	Modified Rayleigh Distribution
MSE	Minimum Square Error
NDLoS	Non-Directed LoS
NDNLoS	Non-Directed Non-LoS
NIR	Near-Infrared
OCC	Optical Camera Communication
OFDM	Orthogonal Frequency Division Multiplexing
OLEDs	Organic LEDs
OS	Operating Systems
OWCs	Optical Wireless Communications
P2P	Point-to-Point
PAPR	Peak-to-Average Power Ratio
PAT	Pointing, Acquisition, and Tracking
PD	Photodetector
PDF	Probability Density Function
PL	Path Loss
PMTs	Photomultiplier Tubes
R2V	Road infrastructure-to-Vehicle
RCA	Radio Corporation of America
RF	Radio Frequency
RS-GBSM	Regular-Shape Geometry Based Stochastic Model
RSH	Right-Side Headlight
Rx	Receiver
SB	Single-Bounce
SET	Sensor Electronics Technology
SINR	Signal-to-Interference-plus-Noise Ratio

SIR	Signal to Interference Ratio
SISO	Single-Input Single-Output
SNR	Signal-to-Noise Ratio
SSL	Solid-State Lighting
SSS	Small Spatial Scale
SUV	Sport Utility Vehicle
TB	Triple-Bounce
TI	Texas Instruments
TIA	Transimpedance Amplifier
Tx	Transmitter
UMCs	Underground Mining Communications
UOWCs	Underwater Optical Wireless Communications
UTD	Uniform Theory of Diffraction
UV	Ultraviolet
UWCs	Underwater Wireless Communications
UWSNs	Underwater Sensor Networks
V2D	Vehicle-to-Device
V2G	Vehicle-to-Grid
V2H	Vehicle-to-Home
V2P	Vehicle-to-Pedestrian
V2R	Vehicle-to-Road infrastructure
V2V	Vehicle-to-Vehicle
V2X	Vehicle-to-Everything
VANET	Vehicular ad-hoc Network
VLCC	Visible Light Communications Consortium
VLCs	Visible Light Communications
VMF	von Mises-Fisher
VVLCs	Vehicular VLCs

WAVE	Wireless Access in Vehicular Environments
WBAN	Wireless Body Area Networks
WHL	Wireless Home Link
WIRCs	Wireless Infrared Communications
WLAN	Wireless Local Area Networks
WLED	White-LED
WLoS	Wide LoS
WPAN	Wireless Personal Area Networks
WUVCs	Wireless Ultraviolet Communications
WYSIWYS	What You See Is What You Send

Symbols

R_λ	photodetector responsivity
A_r	photodetector area
$\delta(.)$	Dirac delta function
ρ	reflectivity
ρ_Vehicles	vehicles reflectivity
ρ_Roadside	roadside reflectivity
m	mode number
δ_L	LSH separation
δ_R	RSH separation
ϕ_T	angle of irradiance
θ_R	angle of incidence
$R\left(\phi_\mathrm{T}\right)$	generalised Lambertian radiant intensity distribution
c	speed of light
t	time
τ	delay
N_0	noise spectral density
R_b	achievable bit rate
P_r	average received power
P_t	transmitted power
$H(0)$	channel DC gain
D_rms	RMS delay spread

$B_{\mathrm{c},50\%}$	channel coherence bandwidth with 50% correlation
μ_τ	mean excess delay
$H(f)$	channel frequency response
$f_{3-\mathrm{dB}}$	3-dB frequency
k	number of reflections
γ_{Tx}	angle of motion of Tx vehicle
γ_{Rx}	angle of motion of Rx vehicle
υ_{Tx}	the speed of Tx vehicle
υ_{Rx}	the speed of Rx vehicle
$\chi^2_{.05}$	χ^2 goodness-of-fit test at the 5% significance level
R_{c}	ceiling radius of horseshoe roadway
d_{v}	vertical separation between the Tx and Rx
d_{h}	horizontal separation between the Tx and Rx
$\mathrm{PL}_{\mathrm{LoS}}$	path loss of LoS component
$\mathrm{PL}_{\mathrm{Diffuse}}$	path loss of diffuse component
ε^{r}	elemental receiver
ε^{s}	elemental source
$\Delta\mathrm{A}$	area of ε^{s} and ε^{r}
N_{c}	number of elementary cells
$\phi_{\mathrm{T},ij}$	the angle from ε^{s} to ε^{r}
$\phi_{\mathrm{R},ij}$	the angle from ε^{r} to ε^{s}
D_{ij}	distance between ε^{s} and ε^{r}
P	spatial partitioning factor
$u(t)$	unit step function
a	environment related parameter
h_{c}	the height of the ceiling above the Tx and Rx
τ_{d}	decay time
$\langle\rho\rangle$	room average reflectivity
A_{room}	room area
χ^2	chi-square goodness test
N_{r}	the number of rays

Γ	gamma function
α_{sh}	the shape parameter
β_{me}	the measure parameter
h_{Rx}	PD height
$x(t)$	instantaneous optical intensity
$y(t)$	instantaneous current produced by the PD
$\circledast$	convolution
$n(t)$	signal-independent AWGN
h_{si}	height of the surface irregularities
Ψ_{FoV}	FoV angle
A_{eff}	effective collection area of the PD
$\phi_{1/2}$	LED half power emission angle
$\mathbf{\Phi}$	luminous flux
I	luminous Intensity
E	illumination
E_{hor}	horizontal illumination
sr	steradian
cd	candela
lm	lumen
lx	lux
L	luminance
$I(0)$	the centre luminous intensity
$D_{\text{TR}}^{\text{LoS}}$	LoS distance between the optical source and the PD
N	the number of scatterers
d_n^{SB}	distance between the WLED lamp and nth local scatterer S_n
G_n	scatterer reflection gain
$E[.]$	statistical expectation operator
$r_{h_{\text{TR}}^{\text{LoS}}}$	autocorrelation function of $h_{\text{TR}}^{\text{LoS}}$
$\phi_{\text{R},0}^{\text{SB}}$	angle-of-rotation
K_{rf}	Rician factor
$h^{ij}(t)$	component ij of the CIR, $i, j \in 1, 2, 3$

a_{e}	ellipse semi-major axis
b_{e}	ellipse semi-minor axis
f_{e}	half length of the distance between the two focal points of ellipse
I_{ls}	the number of related local scattering areas
$f_{I_{\mathrm{ls}}}(i)$	the total possible number of bonuses
m_{s}	the slope of the line
c_{int}	y-axis intercept
ϕ_{S}	the angle of scattering
ρ_{wall}	walls reflectivity
$\rho_{\mathrm{scatterers}}$	scatterers reflectivity
$\varepsilon_{\mathrm{Tx}-n_i}$	distances from the Tx to scatterers $n_i, (i = 1, 2, 3)$
$\varepsilon_{n_i-\mathrm{Rx}}$	distances from scatterers n_i to the Rx, $(i = 1, 2, 3)$
$\varepsilon_{n_1-n_2}$	distances from scatterer n_1 to scatterer n_2
I_{SB}	the number of probable SB subcomponents in two-ring model
$V(\phi_{\mathrm{T}})$	visibility function
$\phi^{n_2}_{\mathrm{T,max}}$	the maximum AoD $\phi^{n_2}_{\mathrm{T}}$ than can be seen by the Rx
$P_{\mathrm{t,R}}$	transmitted power of RSH
$P_{\mathrm{t,L}}$	transmitted power of LSH
$h(t)_{\mathrm{R}}$	CIR of RSH
$h(t)_{\mathrm{L}}$	CIR of RSH
$H(0)_{\mathrm{R}}$	DC gain of RSH
$H(0)_{\mathrm{L}}$	DC gain of LSH
$\alpha^{(n_i)}_{\mathrm{T}}$	AAoD of the waves that impinge on the effective scatterers $s^{(n_i)}$
$\alpha^{(n_i)}_{\mathrm{R}}$	AAoA of the waves traveling from the effective scatterers $s^{(n_i)}$
$\beta^{(n_i)}_{\mathrm{T}}$	EAoD of the waves that impinge on the effective scatterers $s^{(n_i)}$
$\beta^{(n_i)}_{\mathrm{R}}$	EAoA of the waves traveling from the effective scatterers $s^{(n_i)}$
$\xi_{\mathrm{p}-n_3}$	distances from the centre of Tx-sphere to scatterer n_3
$\xi_{n_3-\mathrm{q}}$	distances from scatterer n_3 to the Rx
$\varepsilon_{\mathrm{TR}}(t_0)$	the initial Tx-Rx distance
$\varepsilon(t)_{\mathrm{Tx}}$	Tx distance at the given speed after a specific time
$\varepsilon(t)_{\mathrm{Rx}}$	target Rx distance at the given speed after a specific time

$G(\beta_{\mathrm{R}})$	optical gain of non-imaging concentrator
$T(\beta_{\mathrm{R}})$	transmission coefficient of optical filter
n_{ind}	the refractive index of the concentrator
$f(\alpha, \beta)$	VMF PDF
k_{c}	a parameter that controls the concentration of the VMF distribution
σ_{sh}	shot noise variance
σ_{b}	background noise variance
σ_{d}	dark current noise variance
σ_{th}	thermal noise variance
σ_{total}	total noise variance
d_{SD}	stopping distance
R_{s}	load resistance
C_{PD}	capacitance of PD per unit area
I_2, I_3	noise bandwidth factors
Γ_{FET}	FET channel noise factor
k_{B}	Boltzmann's constant
T_{k}	absolute temperature
q	electric charge
G_{ol}	open-loop voltage gain
g_{m}	FET transconductance
B_{VLC}	VLC system bandwidth
I_{B}	background noise current

Chapter 1

Introduction

1.1 Background

1.1.1 The Next Generation of Wireless Communication Systems

With the increasing popularity and the use of smart devices such as smartphones, laptops, and tablets, the wireless data traffic of mobile devices is growing exponentially. There have been many independent warnings of a looming "Radio Frequency (RF) spectrum crisis" as mobile data demands continue to increase, while the network spectral efficiency saturates [1]. Therefore, researchers have started to focus on the Fifth Generation (5G) wireless systems that are expected to be standardised around 2020 [2]. Compared to the current Fourth Generation (4G) Long-Term Evolution (LTE)/LTE-Advanced (LTE-A) wireless communication networks, 5G wireless communication networks are expected to achieve 1000 times the system capacity [3]. Also, 5G networks should achieve 10 times spectral efficiency with respect to 4G LTE-A and 10 to 100 times higher data rates for typical users [4]. In order to satisfy the aforementioned requirements, various potential promising technologies for 5G wireless communication systems have been suggested. Some of these technologies include advanced multiple access schemes, cell densification, high-efficiency multiple antenna

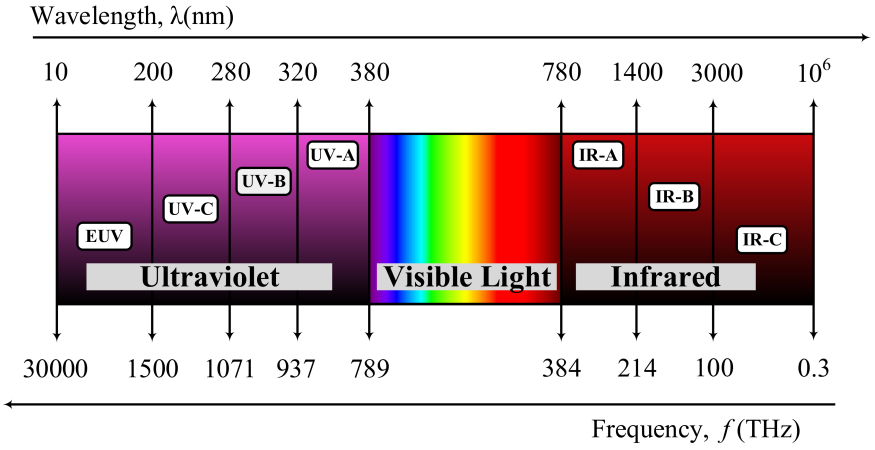

FIGURE 1.1: The optical spectrum.

techniques, and exploitation of the unlicensed spectrum that has not been used for wireless communications before [5], [6]. In terms of the later direction, shifting towards the higher frequencies of the Electromagnetic Spectrum (EM) is considered. In this context, the exploration of the underutilized Milli-meter Wave (mmWave) bands for future cellular communication networks is proposed [7]. For instance, the 60 GHz band has been considered as a part of the IEEE 802.11 ad. However, due to the inherently high Path Loss (PL), 60 GHz links are highly directional and therefore require sophisticated beamforming techniques and tracking algorithms for application in cellular networks. Further shifting beyond mmWave frequencies, there is about 0.3 –30000 THz of bandwidth that called optical spectrum [8]. Wireless communications in optical window is called Optical Wireless Communications (OWCs). OWCs identify three different regions of the EM, i.e., Infrared (IR), visible light, and Ultraviolet (UV). The optical spectrum window is illustrated in Fig. 5.1.

Wireless Infrared Communications (WIRCs) systems utilize the Near-Infrared (NIR) portion (IR-A) which occupies wavelengths from 780 nm to 1400 nm of the entire IR wavelength range (780–10^6 nm). The IR-A extends from the nominal red edge of the visible spectrum. Originally, IR-A was targeted for short-range wireless communications. IR-B (1400–3000 nm) is used mainly for long distance communications either guided (optical fibre) or free space optical communications. While, IR-C portion (3000 –10^6 nm), which is also called thermal imaging region, has been extensively used for

military applications like missiles homing and civilian purposes such as remote temperature sensing. On the other hand, Visible Light Communications (VLCs) use the entire visible light wavelength range between (380–780 nm). Whereas Wireless Ultraviolet Communications (WUVCs) employ UV-C (200–280 nm, the deep UV) segment of the entire UV wavelength range (10–380 nm) [1], [9]. Within UV window, UV-A and UV-B are suitable for a wide range of applications including commercial, military, medicine, and dentistry applications [10]. The last part of the UV spectrum called Extreme Ultraviolet (EUV). This range of wavelengths is absorbed almost completely by the earth's atmosphere [11]. Therefore, EUV requiring high vacuum for transmission. It can be concluded that the useful OWCs spectra that do not fall under the Federal Communications Commission (FCC) regulations include IR-A, IR-B, entire visible light, and UV-C. Hence, the equivalent bandwidth is around 1117 THz, which is a factor of 27000 larger than the RF (3 Hz–30 GHz) including the 60 GHz band (57 –66 GHz). Unlike WIRCs and WUVCs, VLCs possess the ability to provide illumination and wireless communication simultaneously. VLC is realized through the use of off-the-shelf Light-Emitting Diodes (LEDs) for signal transmission and illumination simultaneously. Most recently, VLCs have been identified as a potential solution for mitigating the looming RF spectrum crisis [1]. The vision is that VLCs networks would complement the existing of RF networks towards heterogeneous network convergence. Hence, provide significant spectrum relief by allowing RF wireless networks to off-load a significant portion of wireless data traffic.

1.1.2 Key features of VLCs

VLC is a very attractive technology as lighting sources have been integrated into virtually every inhabited environment. Therefore, there is wide diversity in the field of VLC applications, including Wireless Local Area Networks (WLAN), Wireless Personal Area Networks (WPAN), Wireless Body Area Networks (WBAN), heterogeneous networks, indoor localization and navigation (where current Global Positioning System (GPS) is not available), inter-vehicle networks, underground and underwater networks, offering a range of data rates from a few Mbps to 10 Gbps [12] [13]. There

are many notable features that make VLC technology as one of the most promising solutions within wireless communication landscape, these features can be summarised as below:

1.1.2.1 Sustainable and Green Technology

Although natural light has been around us for many millions of years and there are over 20 billion light bulbs in use around the world today [14], there have been no ecological or health concerns as long as eye safety regulations are fulfiled. This is due to the fact that the light is non-ionizing radiation. Whereas there are recent research argue that might be possible health risk caused by prolonged exposure to RF radiation. In 2011, the International Agency for Research on Cancer (IARC) classified RF electromagnetic fields as a "possible human carcinogen" [15]. Furthermore, LEDs (or Organic LEDs (OLEDs) for future VLCs) are much environmentally friendly compared to conventional incandescent and fluorescent light sources. LEDs have no Mercury or any other hazardous substances, less fragile, and with low heat radiation in case of long period of continuous usage. In the same context, VLC enable safe data transmission in specific environments where RF communication and EM radiation are prohibited or refrained to avoid interference with critical systems. This is due to the fact that the light does not interfere with other electromagnetic waves or with the operation of sensitive electronic equipments. Such environments include aviation and hospitals as well as petrochemical and nuclear power stations [1].

1.1.2.2 Secure Technology

VLCs have inherent security due to spatial confinement of optical beams. This is because in indoor environments the light cannot penetrate through walls and opaque objects. Consequently, there is no interference with similar systems operating next door and hence a higher degree of data security is afforded compared to RF systems [16]. This feature guarantees secure communications that cannot be intercepted and thus it is impossible to access the network covertly by a middleman. In this type

of communication, the user can take part in the communications process through direct the information flow in any desirable direction. Hence, the users can see information carrier channel that is why it so-called What You See Is What You Send (WYSIWYS) technology.

1.1.2.3 Energy-Efficient, Low-Cost Technology

VLCs are enabled by the emergence of the Solid-State Lighting (SSL) technology that evolved rapidly over the past two decades. SSL can offer energy-efficient and long-lasting LEDs. Visible LEDs have a high luminous efficiency (consumed electricity to provide the intended illumination) of 107 lumens/watt (LED T8 Tube) [17] compared to 15 lumens/watt and 60 lumens/watt for incandescent and fluorescent bulbs, respectively [18]. Similarly, LEDs have a long lifespan of 50000 hours compared to 1200 hours and 10000 for incandescent and fluorescent bulbs, respectively. Recently most of lighting systems employ LEDs rather than other types of illumination devices. Therefore no new infrastructure and additional costs of copper cables and labor for pulling cables are required for VLC systems which in turn further increases the cost-efficiency. Moreover, VLCs offer higher Area Spectral Efficiency (ASE) compared with RF communications [19].

1.1.2.4 License-Free Wide Spectrum

VLC utilize the entire visible light wavelength region (380–780 nm). Therefore, the total available bandwidth resource amounts to approximately 400 THz, which is a factor of 10, 000 larger than the RF spectrum including the 60 GHz band [12]. In addition to being operated over a huge license-free spectrum resource, VLCs are complementary noninterfering solution alongside the RF networks.

1.1.3 Challenges for VLCs

Despite all the advantages that offered by VLCs, there are a number of challenges that still need to be addressed. It is worthwhile to emphasise that VLC link impairments can have a significant impact on system performance and capacity. Such impairments include the distortion, which is introduced by the optical wireless channel into the received signal, the non-linear transfer characteristics of the front-ends, and the noise sources. In terms of the distortion induced by the optical wireless channel, it is imperative that the characteristics of the optical wireless channel are well understood in order to analyse and combat the effects of channel distortions. However, channel characteristic of a VLC link can be changed if the transmitter, receiver and intervening reflecting objects are moved by distances of the order of centimetres [20]. From the literature, it has been noticed that a considerable amount of work has been done in terms of WIRCs channel modelling and characterizing. While some of the previous work in WIRCs has been extended to VLCs without a solid justification. It has assumed that since the wavelengths of IR and visible light are contiguous, their channels have similar optical characteristics. This draws attention that the research endeavors on VLC channel modelling and characterisation are still in early stages and explicit generic channel models that can be adapted to wide range of VLC scenarios are still missing in the literature.

1.2 Motivation

Accurate and efficient channel models that are able to mimic key characteristics of optical wireless channels play an important role in designing and testing VLC systems. However, certain key characteristics of indoor VLC channels such as the distribution of surrounding objects and their spectral reflectance are missing in existing conventional indoor VLC channel models. This is due that the most existing indoor VLC channel models are actually an extension of conventional indoor IR channel models.

Furthermore, we extend the research to consider VLCs for unconventional indoor environments, i.e., underground mines environments. On the other hand, since VLCs are not only for indoor applications but could also be used for outdoor applications, one such promising emerging approach is Vehicular VLCs (VVLCs) as part of the Intelligent Transportation Systems (ITS). Since VVLCs are still in very early stages of research, explicit channel models that can be adapted for VVLC systems are still non-existent.

OWCs researchers may have diverse requirements on the optical wireless channel models. More accurate channel models are required for practical wireless system design and simulation. On the other hand, efficient and mathematically tractable channels are useful for theoretical analysis. Due to the lack of accurate generic VLC channel models that take into account indoor and outdoor applications of VLCs, this Ph.D. project is devoted to the modelling and simulation of VLC systems using GBSMs. In GBSMs, geometries are predefined in a stochastic fashion according to certain probability distributions. Hence, it is satisfying reasonable accuracy since it is geometry-based and it considers as an efficient model since it is a mathematically tractable approach.

1.3 Contributions

The key contributions of the thesis are summarised as follows:

- Extensively review channel measurement campaigns that conducted in OWCs and address the recent advances in OWCs channel models primarily in IR and visible light spectra. The important existing channel models are reviewed and classified. Consequently, research gaps in VLC channel models are discussed and outlined.

- Propose a new 2D one-ring FoV RS-GBSM for stationary VLC SISO channels. Based on the proposed model, the main VLC channel characteristics are investigated considering the Line-of-Sight (LoS) and Single-Bounce (SB) components.

- Propose a new 2D multiple bounce RS-GBSM for stationary VLC SISO channels. The proposed model employs a combined two-ring and confocal ellipse model. VLC channel characteristics are thoroughly investigated based on the proposed model. This model has the ability to consider SB, Double-Bounce (DB), and Triple-Bounce (TB) in addition to the LoS components.

- Propose a new 2D RS-GBSM for mobile VVLC SISO channels. The proposed model considered the LoS in addition to SB components, which are reflected off moving vehicles around the Tx and Rx as well as the stationary roadside environments. Furthermore, the model considers DB components that reflected off the surrounding vehicles.

- Propose a novel Three-Dimensional (3D) RS-GBSM for mobile VVLC MISO channels. The proposed model is jointly considered the azimuth and elevation angles by using VMF distribution. The impacts of the vehicular traffic on the received optical power and link performance are investigated.

1.4 Original Publications

The work presented in this thesis has led to the following publications:

1.4.1 Journals

1. **A. Al-Kinani**, C.-X. Wang, L. Zhou, and W. Zhang, "Optical wireless communication channel measurements and models," submitted for publication in *IEEE Commun. Surveys Tuts.* Manuscript first submitted June 12, 2017, accepted with major revisions, re-submitted Jan. 20, 2018.

2. **A. Al-Kinani**, J. Sun, C.-X. Wang, W. Zhang, X. Ge, and H. Haas, "A 2D non-stationary GBSM for vehicular visible light communication channels," submitted for publication in *IEEE Trans. Wireless Commun.* Manuscript first submitted Nov. 20, 2017, accepted with major revisions, Feb. 9, 2018.

3. **A. Al-Kinani**, C.-X. Wang, Q. Zhu, J. Sun, W. Zhang, and H. Haas, "A 3D non-stationary GBSM for vehicular visible light communication MISO channels,". Under final revision of co-authors, planned to be submitted in *IEEE Trans. Vehi. Technol.*

4. **A. Al-Kinani**, C.-X. Wang, and H. Haas, "A novel 3D GBSM for indoor visible light communication channels,". Under final revision of co-authors, planned to be submitted in *IEEE Trans. Commun.*

5. J. Wang, **A. Al-Kinani**, J. Sun, W. Zhang, C.-X. Wang, and L. Zhou, "A path loss channel model for visible light communications in underground mines," submitted for publication in *China Commun.* Manuscript first submitted Dec. 22, 2017, accepted with minor revisions, Jan. 18, 2018.

6. L. Zhou, C.-X. Wang, **A. Al-Kinani**, and W. Zhang, "Visible light communication system evaluations with integrated hardware and optical parameters," submitted for publication in *IEEE Trans. Commun.* Manuscript first submitted Aug. 9, 2017, accepted with major revisions, re-submitted Jan. 23, 2018.

1.4.2 Conferences

1. **A. Al-Kinani**, C.-X. Wang, H. Haas, and Y. Yang, "A geometry-based multiple bounce model for visible light communication channels," **invited paper**, in *Proc. IWCMC'16*, Paphos, Cyprus, Sept. 2016, pp. 31–37. – **Best Paper Award**

2. **A. Al-Kinani**, C.-X. Wang, H. Haas, and Y. Yang, "Characterization and modeling of visible light communication channels," in *Proc. IEEE VTC'16-Spring*, Nanjing, China, May 2016, pp. 1–5.

3. **A. Al-Kinani**, C.-X. Wang, F. Haider, H. Haas, W. Zhang, and X. Cheng, "Light and RF dual connectivity for the next generation cellular systems," in *Proc. IEEE ICCC'17*, Qingdao, China, Oct. 2017, accepted for publication at Aug. 3, 2017.

4. J. Wang, **A. Al-Kinani**, W. Zhang, and C.-X. Wang, "A new VLC channel model for underground mining environment," **invited paper**, in *Proc. IWCMC'17*, Valencia, Spain, June 2017, pp. 2134–2139.

5. J. Wang, **A. Al-Kinani**, J. Sun, W. Zhang, and C.-X. Wang, "A path loss channel model for visible light communications in underground mines," in *Proc. IEEE ICCC'17*, Qingdao, China, Oct. 2017, accepted for publication at Aug. 3, 2017.

1.5 Thesis Organisation

The remainder of this thesis is organised as follows:

Chapter 2 provides a comprehensive literature review of OWCs in terms of evolution, features, and channel scenarios. The main key characteristics of OWCs channels are thoroughly explained. Furthermore, recent advances in OWCs channel measurement campaigns and models in IR and visible light spectra are extensively reviewed. It also highlights the research gaps in VLCs channel models area.

Chapter 3 investigates indoor VLC SISO channel characteristic by proposing a 2D one-ring RS-GBSM. This chapter also defines the radiation pattern of LEDs and provides a brief explanation of photometry science.

Chapter 4 further extends the work in Chapter 3 by proposing a combined two-ring and confocal ellipse model. Unlike one-ring model, this model can model up to the third reflection in addition to the Line-of-Sight (LOS) component. In this chapter, simulation results are further compared with the existing channel models in IR spectrum.

Chapter 5 introduces VLCs to vehicular networks. It presents the key differences between VVLCs and their counterparts of vehicular RF standards. In this chapter, a 2D RS-GBSM for mobile VVLC SISO channels is proposed. The proposed model has the ability to model surrounding vehicles as well as the stationary roadside environments.

Chapter 6 considers 3D VVLCs channel modelling. A novel 3D RS-GBSM for mobile VVLC MISO channels is proposed. The proposed 3D RS-GBSM combining two-sphere and elliptic-cylinder model. This model considers the LoS component in addition to SB components, which are reflected off moving vehicles and stationary roadside environments.

Chapter 7 concludes the thesis by summarising our key research findings and points out future research directions that require further optical channel measurement campaigns and developing more realistic channel models before the actual implementation.

Chapter 2

OWC Channel Measurements and Models

2.1 Introduction

Looking back into history, OWCs predate RF communications by many centuries. Each nation had its own way of using fire signals to warn possible invasion or announce victory. About 800 Before Christ (BC), ancient Greeks and Romans used fire beacons in order to guide ships toward the mainland. In 1880, a light based telephone called photophone was innovated by Alexander Graham Bell to send and receive sound clearly over sunlight via unguided channel for a distance of some 213 m, while shorter ranges were covered using various lamps as a light source. Photophone was considered as the first VLC system [20]. For military purposes, German Army introduced IR photophones in 1935. The light source was a tungsten filament lamp combined with an IR transmitting filter. IR photophones succeeded in communicating over a range of 3 km at daylight and a clear weather [21]. In 1955, Rubin Braunstein, from the Radio Corporation of America (RCA), reported IR emission from a simple diode structured from gallium arsenide (GaAs). Two years later, in 1957, Braunstein further demonstrated that such a diode can be used for WIRCs through sending an audio signal to be detected by a lead sulfide (PbS) diode some distance away [22]. In 1962, Texas Instruments (TI) manufactured the first commercial Infrared LED (IRED) product, which was structured from GaAs compound with emission in the 900 nm wavelength

region [23]. By the fall of 1962, groups at International Business Machines (IBM) research laboratory, Massachusetts Institute of Technology (MIT) Lincoln laboratory, and general electric (GE) succeeded in demonstrating IR laser diode [24]. During the same year, unlike others in RCA, Nick Holonyak chose gallium arsenide phosphide (GaAsP) alloy rather than off-the-shelf GaAs to produce first visible lasing and non-lasing LEDs. Holonyak is seen as the "father of the light-emitting diode" [23]. Thenceforth, advanced visible LEDs, which are capable of switching between different light intensity levels at a very fast rate, became available. The switching speed was fast enough to be imperceptible by human eyes. In this chapter, VLCs evolution will be reviewed in some details since this work is focusing on VLCs channel modelling.

The idea of illumination and data transmission simultaneously by using White-LED (WLED) was first proposed, for Wireless Home Link (WHL), by a research group at Keio University in Japan [25]. In 2003, the Visible Light Communications Consortium (VLCC) was established by Nakagawa Laboratories in partnership with CASIO, NEC, and Toshiba in Japan [26]. VLC technology became sufficiently mature to be standardised by IEEE 802.17.5 working group in 2011 [27]. IEEE 802.17.5 included the link layer and physical layer design specifications. Based on VLC idea, Light Fidelity (Li-Fi) term is coined by [1]. Li-Fi providing bi-directional VLC system by utilizing IR or Wi-Fi for uplink. For instance, the first generation, commercially available full duplex Li-Fi modem using IR for the uplink channel was announced by pureLiFi [28]. OLEDCOMM was the first European company that started to commercialise Li-Fi communication solutions a worldwide level [29]. Most recently, IEEE 802.15.7 task group announced a Call for Proposals (CFP) for the development of the IEEE 802.15.7 r1 standard to be revealed by the end of 2017 [30]. IEEE 802.15.7 r1 technical consideration document aims to provide three main sections including Optical Camera Communication (OCC), Li-Fi, and LED-Identification (LED-ID). OCC is a VLC system but combined with a camera. OCC provide triple functions, i.e., illumination, data transmission/receiving, and positioning/localization.

On the other hand, studies on WUVC techniques date back to at least 1945 [9], mainly for long range communication based on UV-A sources such as carbon arcs,

TABLE 2.1: Features of WIRCs, VLCs, WUVCs, and RF Communications.

	WIRCs	**VLCs**	**WUVCs**	**RF Communications**
Transmitter	IRED, IR Laser	Phosphor-coated blue LED, RGB LED	UVTOP LED	Typical Tx RF Antenna
Receiver	PIN, APD	PIN, APD, SPAD	UVPMT, DUVAP Combined with a solar blind filter	Typical Rx RF Antenna
Standard	IrDA (P2P), IEEE 802.11 (Diffuse)	IEEE 802.15.7 r1 (In progress)	N/A	IEEE 802.11
Communication scenario	Mainly Indoor, secondarily outdoor	Mainly Indoor, secondarily outdoor and underwater	Mainly outdoor, secondarily underwater [9]	Indoor and outdoor
Link configuration	Mainly NDNLoS, secondarily DLoS	Mainly NDLoS	Mainly NDNLoS	NDLoS and NDNLoS
Dominant noise at the Rx	Background light	Background light	Virtually noiseless [9]	Interference noise
Multipath fading	No	No	No	Yes
Doppler effect	No	No	No	Yes
Path loss	High	High	Higher than WIRCs, VLCs and RF	High
Bandwidth	100 THz–384 THz, (IR-A & IR-B)	384 THz–789 THz	1071 THz–1500 THz (UV-C)	3 Hz–30 GHz
Bandwidth regulated	No	No	No	Yes
Cost	Low	Low	Moderate-to-high	High
Range	Short-range (IRED), Long-range (IR Laser) [34]	Short-range	Long-range if compared with WIRCs and VLCs	Short-range and long-range
Communication mode	Mainly unidirectional	Mainly unidirectional	Bidirectional	Bidirectional
Power consumption	Low	Low	Higher than VLCs and WIRCs	High
Eye & skin cafety	Potential eye hazard	Potential eye hazard	Potential eye & skin hazards	No obvious hazard
Penetration	Penetrate through glass but not walls, and opaque objects	Same as WIRCs	Do not penetrate through glass walls, and opaque objects	Penetrate through glass walls, and opaque objects
Security	Higher than RF	Higher than WIRCs, WUVCs, and RF	Lower than WIRCs and VLCs	Low

WLED: white-light-emitting diode; RGB LED: red, green, and blue LED; PIN: p-type/intrinsic/n-type diode; APD: avalanche photodiode; SPAD: single photon avalanche diode; UVPMT: UV photomultiplier tube; DUVAP: deep ultraviolet avalanche photodetector; P2P: point-to-point; N/A: not applicable

low pressure mercury arc lamps, gallium lamps, and nitrogen filled tubes. These devices are typically bulky, power hungry, or bandwidth limited [10], while receivers were, in most cases, Photomultiplier Tubes (PMTs) [31]. The first UV-A LED was reported by Jacques Pankove at RCA in 1972 using gallium nitride (GaN) alloy. Sensor Electronics Technology (SET) has developed a state-of-the-art miniaturized UV-C LEDs, called UVTOP series, in 2002 [32]. Since then, UV-C has the potential to be used in short-range wireless communication and sensing. The very latest UV LEDs-based communication test-bed was reported in [33]. The setup can reliably deliver a data rate of 2.4 kbps for a vertically pointing transmitter and receiver of 11 m separation. Rapid development in compound semiconductor design and fabrication of LEDs, PDs, and filters, has inspired recent research and development in the OWC technology. The key differences between WIRCs, VLCs, and WUVCs technologies are detailed in Table 2.1. Here, RF communication technology has been added to the comparison in order to make it more generic.

The rest of the chapter is organised as follows. In Section 2.2, various scenarios of OWCs links are presented and the trade-off between their features is thoroughly explained. OWCs channel characteristics have been detailed in Section 2.3. An overview

of OWC measurement campaigns is provided in Section 2.4. The state-of-the-art of OWC channel models is presented in Section 2.5. Conclusions are finally drawn in Section 2.6.

2.2 Channel Scenarios

The characteristics of the optical wireless channel can vary significantly depending on the optical wireless channel scenario (also called link configuration, link design or topology in many literature). This section presents the most common optical wireless link scenarios, their specifications, and the trade-off between them. In principle, all communication technologies within OWCs share common link designs. However, some link designs are only applicable for specific scenarios and such examples will be presented. Basically, it is convenient to classify OWC link configurations according to three criteria. Firstly, the degree of directionality of the Tx and Rx. Secondly, the existence of uninterrupted LoS path between the Tx and Rx. Thirdly, the Tx divergence angle and the FoV of the Rx. Accordingly, there are four common link configurations mostly referred in literature as 1) Directed LoS (DLoS); 2) Non-Directed LoS (NDLoS); 3) Non-Directed Non-LoS (NDNLoS); and 4) Tracked [20], [10], [35], [36]. Aforementioned link scenarios classifications are illustrated in Fig. 2.1.

2.2.1 DLoS

This link scenario is shown in Fig. 2.1(a). It is practicable in all OWCs technologies, especially in WIRCs. It is established when the Tx is oriented towards the Rx. This design is utilized in Point-to-Point (P2P) and simple peer-to-peer networking OWC links [37]. It is commonly used for indoor short-range communications. Whereas, for outdoor communications, lasers rather than LEDs are being employed in most cases, e.g., Free Space Optical Networking Architecture (FSONA) technology which utilizes IR-B band in WIRCs [34]. DLoS design offers low power requirement (maximizes power efficiency) because the optical channel loss will be limited only by free space

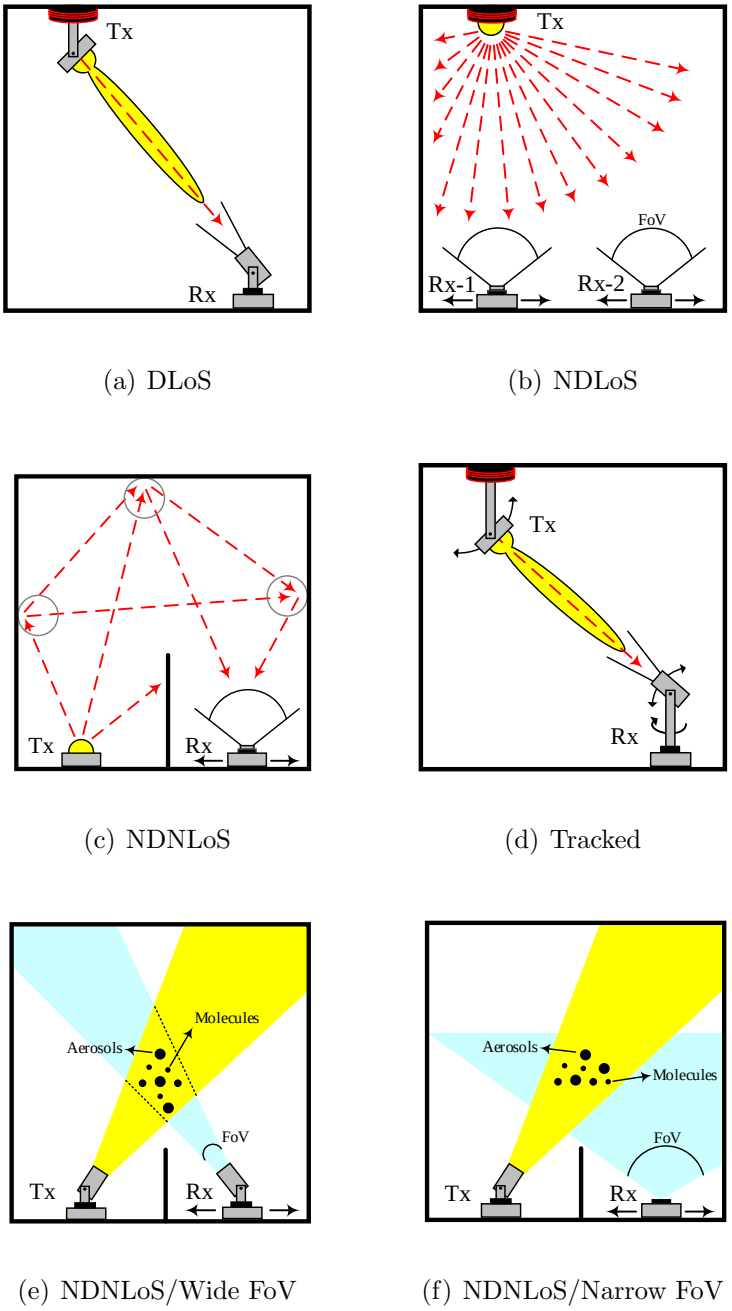

(a) DLoS (b) NDLoS

(c) NDNLoS (d) Tracked

(e) NDNLoS/Wide FoV (f) NDNLoS/Narrow FoV

FIGURE 2.1: OWC channel scenarios.

PL and hence higher data rate can be obtained. This is, however, at the cost of limited mobility, small coverage area, and stringent link alignment [38]. The main drawback of DLoS link is that it is sensitive to blockage and shadowing [36].

2.2.2 NDLoS

Sometimes called Wide LoS (WLoS) [39]. This link is most suitable for point to multi-point indoor communication applications. As seen in Fig. 2.1(b), this design exhibits more flexibility since both Tx and Rx have wide optical aperture, i.e., wide beam divergence angle for the Tx and wide FoV for the Rx. Accordingly, no alignment is necessary and therefore, NDLoS links may be more convenient to use, particularly for mobile terminals since they do not require orientation of the Tx or the Rx [36]. Furthermore, due to reflections form rooms walls, objects and fixtures, this link configuration shows more robustness to shadowing and blockage. However, reflections are considered the main reason for increasing the PL in addition to multipath dispersion which ultimately leads to the transmission bandwidth limitation [38]. NDLoS links are applicable in all OWCs technologies, particularly in VLCs, since it provides illumination in the first place.

2.2.3 NDNLoS

This link design does not impose LoS connection between the Tx and Rx. This design is well known as diffuse link configuration in WIRCs. In this configuration, Tx with wide beam divergence is pointed towards the ceiling. The diffuse reflections off ceiling, walls, and objects are used to establish a link to a wide FoV Rx that also faces the ceiling as shown in Fig. 2.1(c). Diffuse link maintains sustained connection between the Tx and Rx. Consequently, this will offer users a wide degree of mobility and high robustness against link loss due to blockage [40]. Since no LoS required, the diffuse configuration is considered the most convenient for both infrastructure and ad hoc networks. Unfortunately, diffuse configuration sustains high PL due to the absence of a direct path, typically 50-70 dB for a horizontal separation of 5 m in WIRCs [20]. In addition to high PL, diffuse configuration experiences multipath dispersion. Multipath dispersion induced Intersymbol Interference (ISI) and consequently Bit Error Rate (BER) degradation and hence limiting data rate [41]. Multipath power penalty is added in order to overcome ISI, therefore this link configuration is less power efficient

TABLE 2.2: Key features of OWCs channel scenarios.

Link design	**Technology**	**Capacity**	**Bandwidth**	**Power efficiency**	**End eser mobility**	**Coverage area**
DLoS	WIRCs	High	Highest	Highest	Stationary	Small
NDLoS	WIRCs, WUVCs, VLCs	Low	Low	Low	Mobile	Large
NDNLoS	WIRCs, WUVCs	Lower than NDLoS	Lowest	Lowest	Mobile	Largest
Tracked	WIRCs	High	High	High	Mobile	Larger than DLoS

than aforementioned links. NDNLoS link configuration is mainly used in WUVCs and WIRCs, but it is based on scattering from the particles in the atmosphere rather than diffuse reflection in WIRCs as illustrated in Figs. 2.1(e) and 2.1(f). Based on a specific application, the Rx can be of wide or narrow FoV. Furthermore, the distance between the Tx and Rx in case of WUVCs is further. NDNLoS link configurations are more viable in WIRCs and WUVCs than in VLCs [42].

2.2.4 Tracked

Tracked scenario is a special case of the DLoS scenario [43] as illustrated in Fig. 2.1(d). It is proposed to enable user mobility, improve power efficiency, reduce multipath induced ISI, and provide high data rate within one configuration [44]. A tracked system could be incorporated in either a ceiling-mounted transceiver (Base Station (BS)) or the mobile terminal or both [45]. Tracking mechanism is done through three main components: an acquisition unit to observe the presence of a new mobile station within a specific area, a tracking unit to track this new mobile station, and a pointing unit to aim the optical beam so that it is on or closely parallel to the required optical path (with tolerable offset). This technique is known as the Pointing, Acquisition, and Tracking (PAT). Tracked configuration is more feasible in WIRCs. However, mechanically steerable optics are expensive and difficult to miniaturize. Consequently, a solid-state tracking system that eliminates steering requirements was proposed in [45].

Key features of OWCs channel scenarios are summarised in Table 2.2.

2.3 Channel Characteristics

In order to design, implement and operate an efficient OWC system, it is essential that the characteristics of the optical wireless channel are well understood. Unlike RF channels, optical wireless channels do not experience multipath fading [20]. This is due to the fact that in OWCs, the PD dimensions are in the order of millions of optical wavelengths, which leads to an efficient spatial diversity that exhibits a high degree of immunity to multipath fading [20], [41], [46]. Therefore, there is no small-scale fading in OWCs. Furthermore, the use of IM/DD in OWC systems eliminates the transmitter and receiver local oscillators and hence no Frequency Offset (FO) in OWCs. While in terms of Doppler shift, it has been shown in [47] that Doppler frequency has negligible effects in OWC systems. This is because the corresponding wavelength shift is small enough to assume that bandwidth spreading and Signal-to-Noise Ratio (SNR) variation due to Doppler are insignificant problems in most IM/DD based applications [12], [47]. Although OWCs do not experience multipath fading, they do suffer from the effects of multipath dispersion, which manifests itself in a practical sense as ISI. On the other hand, large-scale fading due to PL and shadowing in addition to ambient noise and the non-linear transfer characteristics of the front-ends are considered the main challenges that greatly affect the OWC link performance.

OWC channel characteristics depend in the first place upon the type of communication environment, e.g., indoor, outdoor, and recently Underwater Optical Wireless Communications (UOWCs) [48]. Furthermore, environment details are affecting channel characteristics. For instance, indoor environment could be household, office building, factory, shopping mall, etc., and these differently affect the optical channel. Hence, the different environment would cause different optical channel characteristics. Secondly, the positions of the Tx and Rx. Therefore, applied indoor characterization techniques is not really effective for determining the outdoor (or underwater) channel characteristics and system performance [49]. Table 5.1 presents the most common environments and some of their examples. In the following subsections, we will present

TABLE 2.3: OWCs common environments.

Environment	**Field of Application**
Small-scale indoor	Typical rooms
Mid-scale indoor	Offices, labs, and workshops
Large-scale indoor	Factories, sport complexes, shopping malls and hospitals
Open indoor	Train stations, airports, museums, and exhibit halls
Intra-Vehicle	Vehicles, trains, and airplanes
Inter-Vehicle	Vehicle-to-Vehicle (V2V), Vehicle-to-Road infrastructure (V2R), and Road infrastructure-to-Vehicle (R2V)
Outdoor	P2P [34]
Underground	Subway stations, underground roads, and mines [50]
Underwater	Ocean-bottom

a brief explanation of the optical wireless channels characteristics.

2.3.1 Channel Impulse Response (CIR) $h(t)$

Characterization of the OWC channel is performed by its Channel Impulse Response (CIR) $h(t)$, which is then used to analyze and combat the effects of channel distortions. CIR $h(t)$ is the time evolution of the signal received by the Rx when an infinitely short optical pulse is sent from the Tx [51]. CIR $h(t)$ allows predicting what the system's output will look like in the time domain. Once the CIR $h(t)$ is known, any waveform distortion due to multipath propagation can be calculated and the output of the system can be predicted for any arbitrary input without even testing it (when the system is Linear Time-Invariant (LTI)). The mathematical expressions of the CIR $h(t)$ for DLoS and diffused scenarios will be detailed in Section 2.5.

2.3.2 Channel DC Gain $H(0)$

For intensity-in intensity-out channels, the DC value of their frequency responses can be expressed as [35]

$$H(0) = \int_0^\infty h(t)dt. \tag{2.1}$$

The latter expression is referred as channel DC gain, which is the fraction of power emitted from a continuous-wave transmitter that is detected by the receiver. Channel DC gain $H(0)$ is related to the average received power P_r, by $P_\mathrm{r} = P_\mathrm{t}\ H(0)$, where P_t is the average transmitted power. Furthermore, it determines the achievable SNR as [20]

$$\mathrm{SNR} = \frac{R_\lambda^2 H^2(0) P_\mathrm{r}^2}{R_\mathrm{b} N_0}. \tag{2.2}$$

Here, R_λ, N_0, R_b denote responsivity of the PD, the noise spectral density, and achievable bit rate, respectively. From (2.2), it can be seen that the SNR in VLC systems is proportional to P_r^2 compared with P_r in the conventional RF channels. Consequently, this necessitates the need for higher optical power requirement and a limited PL to deliver the same performance. Therefore, VLC technology is considered as a good candidate for future short range communications.

2.3.3 Root Mean Square (RMS) Delay Spread

In NDLoS and NDNLoS link configurations, due to the reflections off walls, ceiling, and furniture, the optical transmitted signal takes multipath to reach a fixed or mobile Rx. Due to the difference in propagation path length, the received signal appears as a sum of weighted, delayed copies of the transmitted signal [52]. Hence, the optical channel stretches the transmitted signal in time resulting in the so-called temporal dispersion. This major characteristic can be quantified by the RMS delay spread D_rms of CIR $h(t)$ as [53]

$$D_\mathrm{rms} = \sqrt{\frac{\int_{-\infty}^{\infty}(t-\mu_\tau)^2\ h^2(t)dt}{\int_{-\infty}^{\infty} h^2(t)dt}}. \tag{2.3}$$

Here, μ_τ is the mean excess delay: $\mu_\tau = \frac{\int_{-\infty}^{\infty} t\ h^2(t)dt}{\int_{-\infty}^{\infty} h^2(t)dt}$. RMS delay spread D_{rms} can be used to measure the severity of ISI created by a multipath channel [43].

Based on D_{rms}, channel coherence bandwidth can be expressed as [1]

$$B_{\text{c},50\%} = 1/(5D_{\text{rms}}). \tag{2.4}$$

Here, 50% denotes the decorrelation percentage. Likewise, based on D_{rms}, the maximum bit rate, which can be transmitted through the optical wireless channel, is given as [12], [54]

$$R_{\text{b}} \leq 1/10D_{\text{rms}}. \tag{2.5}$$

2.3.4 Frequency Response $H(f)$

The impact of multipath effect on the optical wireless channel bandwidth can be easily seen in frequency domain rather than time domain. Channel frequency response $H(f)$ can be estimated by using Fourier transform of CIR $h(t)$. The 3-dB frequency of the optical channel is obtained as [55], [56]

$$|H(f_{3-\text{dB}})|^2 = 0.5\,|H(0)|^2\,. \tag{2.6}$$

It has been proved that the higher-order reflections have significant impact only at low frequencies whereas the high-frequency magnitude response is characterized by the first-order reflection only [57]. In general, it has been shown that the variation of the received power in environments with different reflectivity and the available bandwidth are almost inverse to each other [1].

2.3.5 Path Loss (PL)

In DLoS and tracked channel scenarios, indirect propagation paths contribution can be neglected. Thus, unshadowed LoS PL model is expressed based on the knowledge

of the radiated pattern, Rx size and separation distance as [41]

$$\mathrm{PL_{LoS}\ (optical\ dB)} = -10\log_{10}\left[\frac{A_\mathrm{r}}{\pi}\frac{d_\mathrm{v}^2}{(d_\mathrm{v}^2+d_\mathrm{h}^2)^2}\right] \tag{2.7}$$

Here, d_v, d_h, and A_r denote the vertical separation between the Tx and Rx, horizontal separation, and the area of the PD, respectively. However, for NDLoS and NDNLoS channel scenarios, the prediction of the optical PL is more complex since it depends on environment parameters such as room dimensions, furniture, reflectivity, orientation and position of the Tx and Rx. The PL of unshadowed diffuse configurations can be estimated using the expression [41], [58]

$$\mathrm{PL_{Diffuse}\ (optical\ dB)} = -10\log_{10}\left(\int_0^\infty h(t)\ dt\right). \tag{2.8}$$

Therefore, to estimate the optical channel PL, it is necessary to analyze the CIR $h(t)$ for a given environment. There are different attempts to accurately estimate the optical PL in different environment and scenarios, e.g., [20], [41], [59].

2.3.6 Shadowing

Channel PL is increased further if a temporary obstruction, such as a person obscures the Rx such that the main signal path is blocked or partially obstructed. This situation is referred to as shadowing, which is another vital factor that affects the performance of OWC systems. Unlike RF waves, optical waves cast clear shadows (hard shadow). This is due to the fact that the optical waves have very short wavelengths compared to the size of the human body (i.e., the obstruction), and hence they do not diffract noticeably [60]. It has been shown that signal path obstruction by furniture can be easier predicted and hence avoided through the implementation of the appropriate channel scenario and Tx/Rx orientation. However, most current studies primarily focus on the modelling and analyzing the shadowing and blockage that caused by moving or stationary people, such as in [60]–[61].

It is also worth to mention that some studies have modelled PL and shadowing for NDLoS and diffuse scenarios using curve-fitting methods based on experimental data such as in [1], [41], [62], [59]. For instance, the authors in [59] adopted the already existing PL model that including shadowing of RF transmission to OWCs. Consequently, the PL exponent and shadowing standard deviation values have been estimated for different propagation paths and scenarios for a specific environment.

2.4 Channel Measurements

This section presents a brief survey of the conducted measurement campaigns of OWCs, mainly for WIRCs and VLCs. However, a complete survey of WUVCs channel measurements and models is beyond the scope of this thesis. This is due to that WUVCs are mainly used for outdoor communications [63]. Furthermore, unlike WIRC and VLC channels, WUVC channels exhibits different propagation characteristics due to molecular and aerosol scattering. For instance, in the case of DLoS channels, the multiple scattering is more pronounced than in an NDNLoS channels. Furthermore, decreased visibility range may result in enhanced NDNLoS channels, the opposite of conventional optical channels [10]. Therefore, WUVCs are mainly NDNLoS. Here, the authors would like to draw the reader's attention to the fact that there has been a long history of research on WUVCs channel measurements and modelling reported in the literature that can be found in [9], [10], [31], [64], [42], [65].

In order to understand the underlying physical phenomenon of optical wireless signal propagation in indoor environments and validate the proposed optical wireless channel model, measurement campaigns need to be carried out. A perfect channel model is a model, that perfectly fits against the measured channel [52]. Therefore, some proposed channel models were combined with experimental measurements to verify the proposed channel model, e.g., [57], [66]. On the other hand, some channel models have been verified based on the measurement campaign of the others, such as in [67]. In general, measurements results showed that indoor WIRC channels are very dynamic with significant variations in the channels' characteristics. These results were based

on the data that collected from, firstly, various rooms. Secondly, in different Rx locations within the same room. Thirdly, for different orientations of the Rx at the same location of the same room [68].

There is a rich history of relevant studies on measurement based WIRC channel modelling conducted since the 1990s, e.g., [41], [68]–[69]. The research work on measurements and modelling of indoor RF channels in [70] has been extended by the same working group to consider diffuse indoor WIRCs. The results of the analysis emphasize that WIRCs are a suitable candidate for high speed wireless data communication inside buildings. Since the early experimental measurements of WIRC channels that done by J. R. Barry *et al.* [57], many other research groups have begun to investigate more WIRC channel characteristics. Although Barry's derived optical wireless channel models have been verified by measurements, that models were applicable only to particular room environments and scenarios, which are detailed in [57]. Consequently, Barry *et al.* could not make general statements about all room configurations. In [41], more generalised measurements based research on approximately 100 different WIRC channels. Both NDLoS and diffuse link configurations have been considered, with and without shadowing. The latter study pointed out that the unshadowed NDLoS configurations generally have smaller optical PL, D_{rms}, and power penalties compared with their unshadowed diffuse counterparts. On the other hand, shadowed NDLoS configurations, generally exhibit larger values of the above three characteristics compared with the corresponding shadowed diffuse configurations. Another measurement campaign is reported in [71] to examine the WIRC channel characteristics and system performance. The measurements were conducted in the absence of ambient light and under different lighting conditions, to quantify the impact of ambient light noise.

Measurement-based stochastic approach in OWCs was first introduced in [69] to compute the diffuse CIR $h(t)$ of indoor WIRCs. Compared with iterative method in [35], stochastic approach offers increased flexibility and reduced computational complexity. The authors have utilized about 14000 measures of CIR $h(t)$ to fit the shape of certain well-known distributions, i.e., Rayleigh and Gamma. The fitting process was carried out using Cramér-von Mises (CvM) and Minimum Square Error (MSE) criteria. The

study, however, has not considered the presence of LoS components. Based on their previous work in [68], the same working group have performed further comprehensive measurements campaign to investigate the impacts of receiver rotation and shadowing on the indoor WIRC channels. The measurements have been executed in nine different rooms in the Colonel By Hall (CBY) at the University of Ottawa [62]. The study adopted both NDLoS and diffuse link configurations. The measurements results have presented several outcomes that are helpful in the characterization of WIRC channels. It has been observed that the variations of optical wireless channel PL for small changes of Rx rotation in NDLoS channels, is well approximated by a Gamma distribution. The results have also demonstrated a correlation between the channel D_{rms} and channel PL for both NDLoS and diffuse link configurations. Consequently, a simple formula has been provided to express that correlation. Furthermore, measurements have also been proved that shadowing reduces the received optical power and increases the channel D_{rms}. The authors in [44], have conducted measurement campaigns to verify the spherical channel model for WIRC channels. Both tracked and diffuse configurations have been considered. Likewise, in [66], HAYASAKA-ITO channel model, has been verified by channel measurements. More details regarding the outcomes of previous two models will be given in next section. On the other hand, in terms of VLC channel measurements, it has been noticed that there is a few measurement campaigns have been conducted for the indoor VLC channels and they are mostly confined to NDLoS link configuration. An early experimental work on VLC channel measurements was performed by Samsung Electronics [72]. The authors in [73], have derived the PL in the photometric domain for short range NDLoS channel. In [56], VLC channel measurements were carried out in a rectangular empty room. In the later study, for the comparison purpose, the iterative site-based modelling technique [74] was adopted for the CIR $h(t)$ simulation of the indoor VLCs. Despite the impact of higher-order reflections consideration in measurements, the results showed a good agreement between simulation and measurements. Another measurements campaign is conducted in [38] in order to investigate diffuse indoor VLC channel characteristics. It has been demonstrated that the coverage area in indoor VLC systems can be increased by using holographic Light Shape Diffuser (LSD) with suitable angles.

TABLE 2.4: The most important OWC channel measurement campaigns.

Ref.	Year	Environment	Scenario	Channel Characteristics	No. Of Bounces	Operating Wavelength
[57]	1993	Empty conference room	NDLoS and diffuse	$h(t)$, $H(f)$	3	NIR LD (λ= 832 nm)
[68], [76]	1994	8 Different furnished rooms at the uOttawa	NDLoS and diffuse	$H(f)$, PL	NA	NIR LD (λ= 810 nm)
[41]	1995	5 Different rooms: 2 empty, and 3 furnished rooms	NDLoS and diffuse	$h(t)$, $H(f)$, D_{rms} PL, Shadowing	NA	NIR LD (λ= 832 nm)
[71]	1996	4 Different empty rooms	NDLoS and diffuse	$h(t)$, $H(f)$, D_{rms}, PL	NA	NIR LD (λ= 806 nm)
[69]	1997	Empty square room	Diffuse	$h(t)$, D_{rms}, μ_τ	NA	NIR IRED (λ= 832 nm)
[62]	2001	9 Different furnished rooms at the uOttawa	NDLoS and diffuse	$h(t)$, $H(f)$, D_{rms}, PL	NA	NIR LD (λ= 808 nm)
[44]	2002	Rectangular empty lab	Tracked and diffuse	$H(f)$, PL	$1 \geq$	NIR LD (λ= 993 nm)
[66]	2007	Empty rectangular room	Diffuse	$h(t)$, $H(f)$, PL	1^{st}, $3 \geq$	NIR LD (λ= 784 nm)
[72]	2008	Rectangular furnished room	NDLoS	$h(t)$,	1^{st}	Red LED (λ= 650 nm)
[73]	2010	Rectangular empty room	NDLoS	$H(0)$, PL	NA	White LED (λ= 380–780 nm)
[38]	2012	Rectangular empty room	NDLoS	$H(0)$	NA	Blue LED (λ= 455 nm)
[56]	2012	Rectangular empty dark room	Diffuse	$h(t)$, $H(f)$	3	Blue LD (λ= 445 nm)
[60]	2014	Furnished meeting room	NDLoS and diffuse	$h(t)$, D_{rms}, μ_τ PL, Shadowing	NA	White LED (λ= 380–780 nm)
[75]	2015	Corridor, empty hall furnished office room	NDLoS	$H(0)$, D_{rms}, μ_τ	NA	White LED (λ= 380–780 nm)

NDLoS: Non-directed LoS; $h(t)$: channel impulse response; $H(f)$: channel frequency response; PL: path loss; D_{rms}: root mean square delay spread; μ_τ: mean excess delay; NIR: near-infrared; LD: laser diode; LED: light-emitting diodes; IRED: infrared light-emitting diode; uOttawa: University of Ottawa; N/A: not applicable

In terms of shadowing, the authors in [60] have considered the effect of channel PL and shadowing. They used human body as a temporary obstruction to model the shadowing in VLCs. In [75], the effect of people movement on indoor VLC channel characteristics, such as received power and D_{rms}, was investigated in three different environments. Measurement results showed that VLC technology is robust enough for indoor communications since it is offering excellent mobility even when considering an environment with high people density. Here, we classify (in chronological order) the important measurements campaigns for WIRC and VLC channels according to the publishing year, environment, scenario, measured channel characteristics, the number of bounces, and the operating wavelength as detailed in Table 2.4.

2.5 Channel Models

In terms of channel modelling approaches, there are many channel models for conventional WIRCs reported in [16], [44], [57], [59], [77]–[78]. On the other hand, in terms of VLC channel modelling, an explicit state-of-the-art of VLC channel models has not been investigated adequately yet. Although few literary works related to VLC channel modelling have been reported in [58], [79]–[80], research in this area is still at an early stage. Furthermore, the IEEE 802.17.5 does not specify VLC channel models to be used for technology evaluation yet [81]. Therefore, an explicit generic channel model that can be adapted to a wide range of VLC scenarios is still missing in the literature. In order to summarise what has been done so far in the literature, the most important OWC channel models, primarily for WIRCs and VLCs, are presented in Table 2.5. As can be seen, the OWCs channel models are briefly reviewed and tabled according to the year of publishing, modelling approach, environment, scenario, investigated channel characteristics based on each approach, the number of bounces, and the operating wavelength. The OWC channel models that are presented in Table 2.5 can be classified as deterministic and stochastic models. For instance, different approaches are included in the deterministic approach, e.g., recursive [57], iterative [74], DUSTIN [67], Geometry-Based Deterministic Models (GBDM) based on ray-tracing [79]–[82], and Ceiling Bounce Model (CBM) [83]. On the other hand, the stochastic models can be further classified into Geometry-Based Stochastic Models (GBSM) and non-GBSM. Channel models such as spherical model [44] and Regular-Shape Geometry Based Stochastic Model (RS-GBSM) [80] can be classified as GBSMs. While, channel models such as Monte Carlo algorithm (MCA) [77], and Modified CBM (MCBM) [84] are classified as non-GBSMs. MCBM uses a combination of the traditional CBM and a stochastic approach in order to mitigate the computational complexity in deterministic models. Fig. 2.2 illustrates OWC channel models classification for most common channels models. Here, we have highlighted some of OWC channel models with related literature, while in the following subsections, we will give a descriptive overview of each channel model individually.

TABLE 2.5: The most important OWC channel models.

Ref.	Year	Modelling Approach	Environment	Scenario	Channel Characteristics	No. of Bounces	Operating Wavelength
[16]	1979	Cavity Model	Empty rectangular small office, large office and hall	Diffuse	$H(0)$, μ_τ	1	NIR IRED (λ= 950 nm)
[57]	1993	Recursive Method	Empty conference room	NDLoS and diffuse	$h(t)$, $H(f)$	3	NIR LD (λ= 832 nm)
[85]	2002	Recursive Method	Empty rectangular room	NDLoS	$H(0)$, SNR	0	White LED (λ= 380–780 nm)
[86]	2004	Recursive Method	Empty rectangular room	NDLoS and diffuse	$H(0)$, SNR	2	White LED (λ= 380–780 nm)
[74]	2002	Iterative Method	Rectangular room with arbitrary number of boxes	Diffuse	$h(t)$, PL	10	NIR LD (λ= 832 nm)
[67]	1997	DUSTIN	Empty rectangular room	Diffuse	$h(t)$	1 $\geq$	NIR LD (λ= 832 nm)
[83]	1997	Ceiling-Bounce Model (CBM)	5 Offices and single large room	NDLoS and diffuse	$h(t)$, $H(f)$, D_{rms} PL, Shadowing	1	NIR LD (λ= 832 nm) and (λ= 806 nm)
[78], [84]	2008, 2009	Modified Ceiling-Bounce Model (MCBM)	2 Empty rooms of different sizes	Diffuse	$h(t)$, $H(0)$, $H(f)$ D_{rms}, μ_τ, PL	1	NIR IRED (λ= 800–900 nm)
[87]	2015	Ceiling-Bounce Model (CBM)	Furnished rectangular rooms	NDLoS	$h(t)$	1	White LED (λ= 380–780 nm)
[79]–[82]	2014–2016	Ray-tracing (Zemax®)	Empty/furnished rooms of different sizes and shapes	NDLoS	$H(0)$, D_{rms}, μ_τ	1 $\geq$	White LED (λ= 380–780 nm), NIR IRED (λ= 880 nm)
[88]	2013	Ray tracing	Sports utility vehicle	NDLoS and diffuse	$h(t)$, $H(f)$, D_{rms}	N/A	NIR IRED (λ= 1330 nm)
[77]	1998	Monte Carlo Algorithm	2 Empty rooms of different sizes	Diffuse	$h(t)$, D_{rms}	40	NIR LD (λ= 832 nm)
[89]	1998	Modified Monte-Carlo Algorithm	2 Empty rooms of different sizes	Diffuse	$h(t)$, D_{rms}	40	NIR LD (λ= 832 nm)
[59]	2009	Modified Monte-Carlo Algorithm (Rhinoceros® 3D)	Aircraft cabin	NDLoS and diffuse	PL	N/A	NIR IRED (λ= 870 nm)
[90]	2010	Modified Monte-Carlo	Empty rectangular room and cubic furnished office	NDLoS	$h(t)$, $H(f)$, D_{rms}	4	White LED (λ= 380–780 nm)
[44] [91]	2002	Spherical Model	Rectangular empty lab	Tracked and diffuse	$H(f)$, PL	1 $\geq$	NIR LD (λ= 993 nm)
[92] [93]	2012, 2014	Spherical Model	Empty office room	NDLoS and diffuse	$h(t)$, $H(f)$	1 $\geq$	White LED (λ= 380–780 nm)
[94]	2005	Carruthers Model	11 Empty rooms of different sizes	NDLoS and diffuse	$H(0)$, D_{rms}, μ_τ	3	NIR IRED (λ= 800–900 nm)
[66]	2007	HAYASAKA-ITO Model	Empty rectangular room	Diffuse	$h(t)$, $H(f)$, PL	1st, 3 $\geq$	NIR LD (λ= 784 nm)
[95]	2016	RS-GBSM (One-ring)	Furnished Office room	NDLoS	$h(t)$, $H(0)$, D_{rms}, μ_τ, K_{rf}	1	White LED (λ= 380–780 nm)
[80]	2016	RS-GBSM (two-ring and ellipse)	Furnished Office room	NDLoS	$h(t)$, $H(0)$, D_{rms}, μ_τ, K_{rf}	3	White LED (λ= 380–780 nm)
[96] [58]	2015 2017	Ray-tracing (Zemax®)	Empty/furnished rooms of different sizes	NDLoS	$h(t)$, $H(0)$, D_{rms} μ_τ, B_c, PL	8: Diffuse 14: Specular	White LED (λ= 380–780 nm)

SNR: signal-to-noise ratio; RS-GBCM: regular-shaped geometry-based channel model; N/A: not applicable

2.5.1 Deterministic Channel Models

Deterministic channel models are usually based on the detailed description of specific propagation environment, channel scenario, and the position and orientation of the Tx and Rx. The CIR $h(t)$ of the OWC system is obtained using intensive simulations that incorporate details of propagation environments like rooms, offices, buildings, roads, etc. Therefore, these models are site specific, physically meaningful and potentially

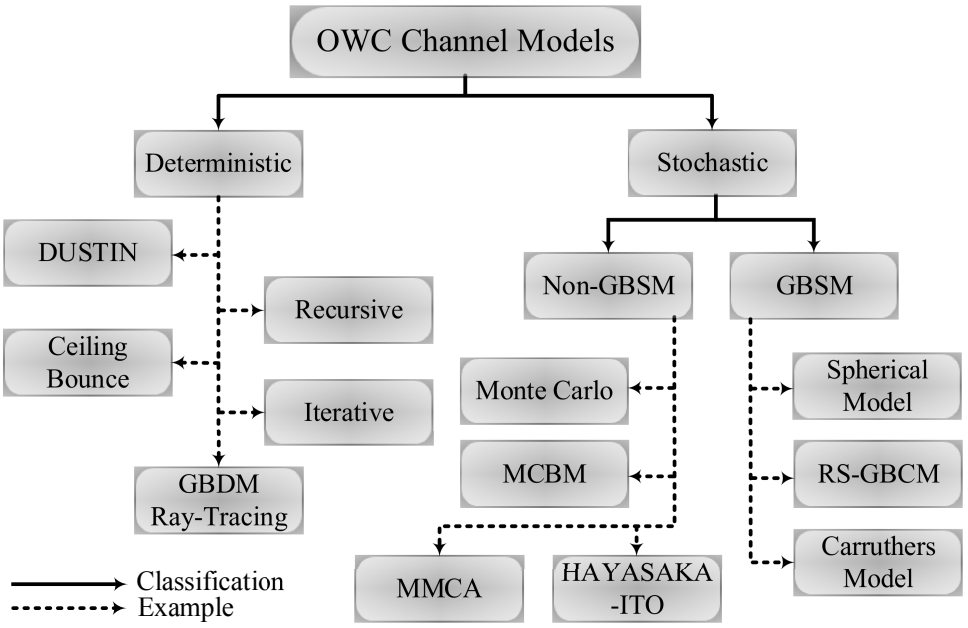

FIGURE 2.2: Classification of OWC channel models.

accurate. Below is a brief review of various approaches of deterministic channel models for OWCs.

2.5.1.1 Recursive Model

This model was presented by J. R. Barry *et al.*, [97], [36], [57]. The recursive approach is advised primarily to evaluate the CIR $h(t)$ of multiple-bounce (more than two reflections) for WIRC channels. It has been considered as an extension of the single reflection cavity model which proposed by Gfeller and Babst in [16]. Here, much interest has been given to recursive approach comparing with cavity model since it is more comprehensive in terms of WIRCs channel modelling. In this model, the radiation intensity pattern $R(\phi)$ for a particular Tx can be modelled using a generalised Lambertian radiation pattern as [16]

$$R(\phi_{\mathrm{T}}) = \frac{m+1}{2\pi} \cos^{m}(\phi_{\mathrm{T}}), \ \phi_{\mathrm{T}} \in [-\pi/2, \pi/2]. \tag{2.9}$$

Here, ϕ_{T} is the angle of irradiance which is commonly denoted as the Angle of Departure (AoD) and m is mode number of the radiation lobe, which specifies the directionality of the optical source. At the receiving side, the PD is modelled as an active

area A_{r} collecting radiation which is incident at angle ϕ_{R} smaller than the PD's FoV. The incident angle is commonly denoted as the Angle of Arrival (AoA). Therefore, the received optical signal is proportional to $A_{\mathrm{r}}\cos(\phi_{\mathrm{R}})$. Only rays that are incident within PD' FoV will be captured. For a particular optical source **S** and optical receiver **R** in a room with Lambertian reflectors, light from the Tx can reach the Rx through direct or multiple paths (number of bounces). Therefore, the CIR $h(t)$, scaled by time domain, can be expressed as the superposition of the LoS and an infinite sum of multiple-bounce components as [20]

$$h(t;S,R) = h^0(t;S,R) + \sum_{k=1}^{\infty} h^k(t;S,R). \tag{2.10}$$

Here, $h^k(t)$ is the CIR of the components undergoing exactly k reflections. The LoS response $h^0(t)$ is approximately a scaled and delayed Dirac delta function $\delta(.)$ expressed as [57]

$$h^0(t) \approx \frac{(m+1)A_{\mathrm{r}}}{2\pi {D_{\mathrm{TR}}^{\mathrm{LoS}}}^2}\cos^m(\phi_{\mathrm{T}})\cos(\phi_{\mathrm{R}})\ \delta(t - D_{\mathrm{TR}}^{\mathrm{LoS}}/c). \tag{2.11}$$

Here, $D_{\mathrm{TR}}^{\mathrm{LoS}}$ and c are the Tx-Rx LoS distance and the speed of light, respectively. The recursive approach is used to solve a given problem by breaking it up into smaller pieces, solve it and then combine the results. Therefore, the implementation of this algorithm is done by breaking the reflecting surfaces into numerous small Lambertian reflecting elements ε (cells), each with an area ΔA as shown in Fig. 2.3. Each cell plays the role of both an elemental receiver (ε^{r}) and an elemental source (ε^{s}). Accordingly, $h^k(t)$ for higher-order terms ($k > 0$) can be calculated recursively and approximated as [57]

$$\begin{aligned} h^k(t;S,R) &\approx \sum_{i=1}^{N_{\mathrm{c}}} \rho_{\varepsilon_i^{\mathrm{r}}} h^{(0)}(t;S,\varepsilon_i^{\mathrm{r}}) \circledast h^{(k-1)}(t;\varepsilon_i^{\mathrm{s}},R) \\ &= \frac{m+1}{2\pi}\sum_{i=1}^{N_{\mathrm{c}}} \frac{\cos^m(\phi_{\mathrm{T}})\cos(\phi_{\mathrm{R}})}{(D_{\mathrm{TR}}^{\mathrm{NLoS}})^2} \\ &\quad \times \mathrm{rect}(2\phi_{\mathrm{R}}/\pi)\ h^{(k-1)}\ (t - D_{\mathrm{TR}}^{\mathrm{NLoS}}/c; s_i, R)\Delta\mathrm{A}. \end{aligned} \tag{2.12}$$

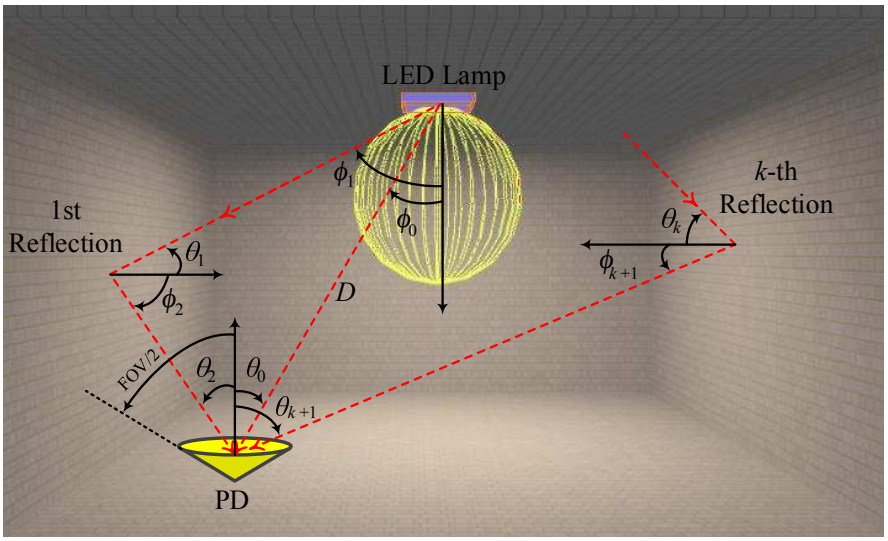

FIGURE 2.3: Recursive channel model.

Here, the symbol $\circledast$ denotes convolution. While, N_c, ρ and s_i denote the number of cells, cell reflectivity coefficient, and the position of each cell, respectively. According to (2.12), in order to calculate $h^k(t; S, R)$, firstly, all possible $h^{(k-1)}(t; \varepsilon_i^s, R)$ must be calculated. Then directly apply (2.12) for the intended Tx. Fig. 2.4(a), illustrates Barry's approach for computing the CIR $h^{(k)}$ of multiple bounce ($k > 0$) recursively. For example, if ($k = 3$), $h^2(t; S, R)$ can be obtained by first computing N impulse responses of $h^1(t; \varepsilon_i^s, \varepsilon_i^r)$. Using these to compute $h^2(t; \varepsilon_i^s, R)$. The latter result then directly applied to (2.12) for the intended Tx.

After a gap of ten years, Barry's model in WIRCs has been first extended to model NDLoS VLC channels in order to make use of the existing power-line network for VLCs [85]. The same researchers of the latter work have adopted Barry's model in VLCs considering up to second order reflection [86]. The previous study discussed the effect of SNR and Rx FoV on data rate. Thereafter, many studies utilized the recursive model for VLC channels, e.g., [55], [98], [86] without solid justification. An improved recursive channel model for VLCs is presented in [99]. This model considers the total path length including electrical signal path passing through a wiring topology in addition to the optical wireless path. Authors in [100] generalised the Barry's model by including wavelength-dependent WLED characteristics and spectral reflectance of indoor reflectors. Their study showed that VLCs provides a larger transmission

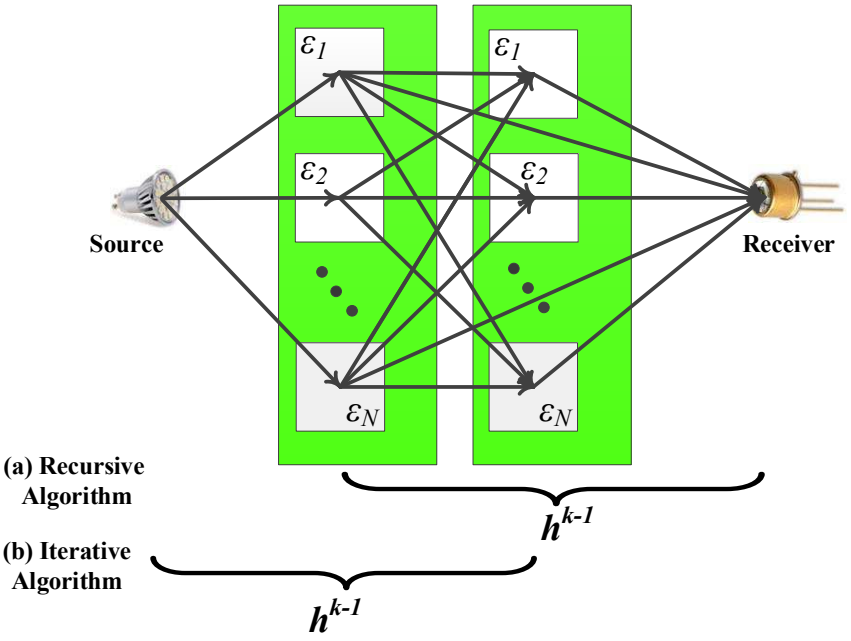

FIGURE 2.4: Recursive and Iterative models.

bandwidth compared with WIRCs. It is worth mentioning that recursive model is still used for VLCs channel modelling so far, e.g., [75]. In recursive approach, although the reliability of results improves with the number of reflections taken into account, the computing time increases exponentially. Moreover, when too few reflections are taken into account, PL and bandwidth are systematically overestimated [44].

2.5.1.2 Iterative Model

Iterative based algorithm was introduced in [74] by J. B. Carruthers. In this method, CIR $h(t)$ calculation follows the basic methodology that outlined in [57] with extensions for an arbitrary number of boxes inside the environment. The LoS CIR $h^0(t)$ can be computed using (2.11). While, the k-bounce response $h^k(t)$ is given as

$$h^k(t;S,R) \approx \sum_{i=1}^{N_c} \rho_{\varepsilon_i^r} h^{(k-1)}(t;S,\varepsilon_i^r) \circledast h^0(t;\varepsilon_i^s,R). \tag{2.13}$$

According to iterative algorithm, (2.13) can be applied with $R = \varepsilon_j^{\mathrm{r}}$ to get

$$h^k(t, S, \varepsilon_i^r) = \sum_{j=1}^{N_{\mathrm{c}}} \alpha_{ij} h^{(k-1)}(t - D_{ij}/c; S, \varepsilon_j^r) \tag{2.14}$$

where

$$\alpha_{ij} = \mathrm{rect}(2\phi_{\mathrm{R}}/\pi)\ \frac{\rho_{\varepsilon_j^r} \cos^m(\phi_{\mathrm{T},ij}) \cos(\phi_{\mathrm{R},ij})}{P^2 D_{ij}^2}. \tag{2.15}$$

Here, the quantities $\phi_{\mathrm{T},ij}$, $\phi_{\mathrm{R},ij}$, D_{ij}, and P denote the source's angle to the receiver, the receiver's angle to the source, the source ($\varepsilon_i^{\mathrm{s}}$)-receiver ($\varepsilon_j^{\mathrm{r}}$) distance, and cells spatial partitioning factor, respectively. For example, if ($k = 3$), $h^2(t; S, R)$, can be obtained by first computing N_{c} impulse responses of $h^1(t; S, \varepsilon_i^{\mathrm{r}})$. Using these to compute $h^2(t; \varepsilon_i^{\mathrm{s}}, \varepsilon_j^{\mathrm{r}})$. The latter result then directly applied to (2.13) for the intended Rx. Fig. 2.4(b) illustrates iterative algorithm. It has been reported that the iterative method is about 92 times faster compared with recursive method when three-bounce considered [74].

2.5.1.3 DUSTIN Algorithm

In order to reduce the computational complexity of the previous models, the authors in [67] developed an efficient simulation approach called DUSTIN algorithm. Similar to recursive and iterative models, this approach was based on a discretization of the reflecting surfaces into cells. However, in DUSTIN approach, the simulation has been done by slicing into time steps rather than into a number of reflections. This method was proposed to simulate the CIR $h(t)$ of indoor WIRCs. DUSTIN algorithm was considered faster compared with traditional iterative and recursive approaches [101]. For instance, in the recursive approach, the time required to compute $h^k(t)$ is roughly proportional to N_{c}^k [57], while it is proportional, in the DUSTIN algorithm, to N_{c}^2 and hence get the advantage of simulating any number of reflections. However, the drawback of this approach is that it is incapable of adapting to different environments. This is due to wireless channel part calculations are saved in a disk file before calculating the response of the Rx and hence it is considered as a site-specific model. DUSTIN approach, on the other hand, has not been utilized in VLCs so far.

2.5.1.4 Ceiling Bounce Model (CBM)

This model came up with a closed-form solution for the CIR $h(t)$, PL, and D_{rms} of diffuse indoor WIRC channels [20], [83]. It was assumed that the Tx and Rx are collocated. It is the most used approach in simulation because of its excellent matching with the measured data and simplicity. Based on this model, WIRC channels can be characterized only by the optical wireless channel PL and D_{rms}. The diffuse CIR $h(t)$ based on CBM is given as [83]

$$h(t,a) = H(0)\ \frac{6a^6}{(t+a)^7}\ u(t). \tag{2.16}$$

Here, $u(t)$ is the unit step function and a is environment related parameter, $a = 2h_{\text{c}}/c$, where h_{c} is the height of the ceiling above the Tx and Rx. The delay spread and approximate 3-dB cut-off frequency for the CBM are given by the following relations $D_{\text{rms}} = \frac{a}{12}\sqrt{\frac{13}{11}}$ and $f_{3-\text{dB}} = \frac{0.925}{4\pi D_{\text{rms}}}$, respectively. It has been noticed that this model can be more realistic with multiple reflections and it accurately models the relationship between D_{rms} and multipath power requirement for diffuse shadowed and unshadowed channels by modifying a as detailed in [83]. On the other hand, when the LoS path dominates, the unshadowed LoS CIR $h(t)$ can be computed, based on cavity model, as [16]

$$h(t) = \frac{A_{\text{r}} d_{\text{v}}^2}{\pi (D_{\text{TR}}^{\text{LoS}})^4} \delta(t - D_{\text{TR}}^{\text{LoS}}/c). \tag{2.17}$$

Here, the Tx is a Lambertian of first-order and it is pointed down, while the Rx is pointed up. For being simple and easy to use, CBM has been employed in VLCs. For example, the authors in [87] utilized CBM to propose a grouped Discrete Fourier Transform (DFT) precoding scheme for reduction of Peak-to-Average Power Ratio (PAPR) for Orthogonal Frequency Division Multiplexing (OFDM)-based VLC systems.

2.5.1.5 GBDMs Based on Ray-Tracing

Most advanced ray-tracing tools are based on the theory of Geometrical Optics (GO) and the Uniform Theory of Diffraction (UTD) [102]. Ray-tracing computing all rays for each receiving point individually, which is the most time-consuming part of a prediction based on this method. For instance, in WIRCs, PL estimation requires about 10^8 trials while estimating the CIR $h(t)$ takes up to 10^{10} trials with subnanosecond time resolution [91]. Based on a specific ray-tracing software, ray-tracing guarantees the specifications of the created environment including geometry, furnishing, and the reflection characteristics of the surface materials as well as the specifications of the Tx and Rx. There is a wide range of available free and licensed ray-tracing software and their platform Operating Systems (OS) are listed in [103]. Moreover, as will be seen later in this subsection, some site-specific ray-tracing software that developed in the field of image processing or illumination design purposes may be useful for optical wireless channel modelling. In [104], ray-tracing based channel modelling created similar results as Barry's recursive model when the simulation is stopped after three reflections. Furthermore, ray-tracing based on ray-quadrilateral intersection algorithm was proposed for intra-vehicle channel modelling in order to investigate WIRC channel characteristics in a Sport Utility Vehicle (SUV) of 15-passenger capacity [88].

In terms of VLC channel modelling, a pure ray-tracing based channel modelling for VLCs has recently presented in [79]. In order to express the CIR $h(t)$ of NDLoS indoor VLC links in rectangular empty rooms of different sizes, the authors exploited the ray-tracing features of a licensed optical software called Zemax® [105]. Originally, Zemax® is a windows-based software able to create a 3D indoor environment where the main purpose of such software is optical and illumination system design. The data which are created by Zemax® are imported into Matlab® to produce the CIR $h(t)$ through considering a proper normalization. The same work has been extended to consider empty rooms with L-shaped and circular shape, furnished rooms, and different wall materials, i.e., brick, wood, and plaster [106]. More generalised study for indoor VLC channel modelling is conducted in [82] including 15 different NDLoS links. The latter studies have demonstrated that the presence of furniture

leads to decrease channel DC gain and D_{rms}. Furthermore, based on comparisons between WIRC and VLC channels, the results further reveal that, for the same configurations, DC gain and D_{rms} of WIRC channels are larger than that of VLC channels. In [96], ray-tracing using Zemax® has been used for VLC channel modelling considering $k = 8$ in the case of purely diffuse reflections and $k = 14$ in the case of mostly specular reflections. In that study, the relation between coherence bandwidth B_c and D_{rms} (for IR and visible light channels) was expressed through curve fitting. While the authors in [58] have extended the work in [96] to model the PL for VLC channels. Based on the above facts, ray-tracing requires a detailed description of the propagation environment and consequently cannot be easily generalised to a wider class of scenarios, therefore, it is also considered as a site-specific model.

2.5.2 Stochastic Channel Models

In stochastic models, the impulse responses of OWC channels are characterized by the law of wave propagation applied to specific Tx, Rx, and scatterer geometries, which are predefined in a stochastic fashion according to certain probability distributions. Compared to the deterministic, the stochastic approach offers increased flexibility, reduced computational complexity, and considered as non site-specific but with lower accuracy.

2.5.2.1 GBSMs

2.5.2.1.1 The Spherical Model

This approach was proposed to model WIRC channels that utilizing diffused link configurations. The model provides a quick rule of thumb in order to approximate prediction of optical wireless channel PL and $H(f)$ for the higher order reflections in indoor environments [44], [91], [104]. This model is inspired by the traditional approach of Integrating Sphere (IS) photometry which is introduced in [107]. A simple analytic formula for CIR $h(t)$ is derived from the integrating sphere and scaled to a specific room as detailed in [91]. Still, the LoS CIR $h^0(t)$ can be computed using (2.11).

While, according to spherical model, the diffused CIR $h_{\text{diff}}(t)$ is given as [20]

$$h_{\text{diff}}(t) = \frac{H_{\text{diff}}}{\tau} \exp(-t/\tau_{\text{d}}). \tag{2.18}$$

Apparently, the CIR $h_{\text{diff}}(t)$ is exponential with decay time τ_{d}. The term H_{diff} denotes diffused channel gain, which is expressed as

$$H_{\text{diff}} = \frac{A_{\text{r}}}{A_{\text{room}}} \frac{\rho}{\langle \rho \rangle}. \tag{2.19}$$

Here, the paramerers A_{room} and $\langle \rho \rangle$ denote the room area and the average reflectivity, respectively. The latter parameter is defined as [44]

$$\langle \rho \rangle = \frac{1}{A_{\text{room}}} \sum_{i} \Delta \text{A}_i \times \rho_i. \tag{2.20}$$

Here, the individual reflectivity ρ_i of the cells weighted by their individual areas ΔA_i. Furthermore, the corresponding channel PL and $H(f)$ have been derived. By using spherical model, it is shown that a highly reflective geometry resulting in a high delay spread, hence low channel bandwidth. In contrast, if the geometry reflectivity is low, this leads to low delay spread and thus high channel bandwidth. The reliability of the spherical model for WIRC channels for the higher order reflections has been confirmed by stochastic based ray-tracing simulation, which takes all diffuse reflections into account [44], [91]. The spherical model, on the other hand, has been employed to investigate VLC channel characteristics based on a new design of LED lighting [93]. While in [92], the accuracy of the spherical model for VLC channels has been examined compared with Barry's model. The simulation results showed that the impulse response of the diffuse portion was overestimated when considering the spherical model. Furthermore, the diffuse portion has no much influence on 3-dB bandwidth.

2.5.2.1.2 Carruthers Model

In this model, the channel responses were generated based on geometrical modelling of indoor environments together with an iterative technique for calculating multiple

reflections [94]. A comprehensive study has examined the characteristics of more than 80000 CIRs of indoor WIRC channels, which are generated using a channel simulator called Infrared impulse response Simulator by Iteration (IrSimIt) [108]. It has been demonstrated that LoS channels must be modelled separately from those fully diffuse channels, which have no such path. Compared to [69], the study declared that the LoS channel gain following a Modified Gamma Distribution (MGD) for $D_{\mathrm{TR}}^{\mathrm{LoS}} < 0.4$ m. While the channel gain for LoS channels including all reflections, follows a Modified Rayleigh Distribution (MRD) for most Tx-Rx distances. The channel gain is measured in decibel (dB) and the fitting process is carried out using chi-square (χ^2) goodness test. Furthermore, the study has recommended a road-map for generating a stochastic realistic impulse response for any given Tx-Rx separation in an indoor environment. On the other hand, the authors in [109] have followed the similar methodology to that used in [94] to model the channel gain and the D_{rms} of diffuse channels. They showed that the shifted lognormal distribution was the best distributions to model diffuse channel gains while the gamma distribution was the best for diffuse D_{rms}.

2.5.2.1.3 RS-GBSM

This models is widely used in RF channel modelling, e.g., [110]–[111]. In this model, the effective scatterers are located on regular shapes, such as a ring, an ellipse [52] or even a combination of both as reported in [110], in case of Two-Dimensional (2D) models. While in case of 3D models, the effective scatterers are lying on a sphere or an ellipsoid, e.g., [112], [111]. Different from physical scatterers, an effective scatterer may include several physical scatterers which are unresolvable in delay and angle domains [111]. RS-GBSM is a mathematically tractable approach, therefore, it has been employed in VLCs. In terms of indoor VLC channel modelling, the authors in [95] used 2D one-ring model to investigate VLC channel characteristics. The results have been verified with [57] (configuration A). In [80], a 2D combined two-ring and confocal ellipse model was proposed to model VLC channels. Simulation results have shown comparable results with [40] up to three reflections. A 3D RS-GBSM combines a sphere and an ellipsoid is proposed to characterise indoor VLC channels in [113].

Whereas, in terms of outdoor VLC channel modelling, 2D and 3D RS-GBSMs have been used to model vehicular VLC channels [114], [115].

2.5.2.2 Non-GBSMs

2.5.2.2.1 Monte Carlo Algorithm (MCA)

After a year of introducing DUSTIN algorithm, the same working group has introduced MCA in order to further reduce the intensive computational effort required to compute the CIR $h(t)$ for indoor WIRC channels [77]. In MCA, the generalised Lambertian radiation pattern is assumed and the same link configurations in [67] and [57] (configuration A), are employed in order to compare the results. The simulation in this method is neither sliced into a number of reflections as in [57], nor in time steps as in [67]. It can be implemented through three steps: ray generation, wall processing and calculation of the PD response. MCA allows evaluation of impulse response for not only Lambertian ($m \geq 1$) but also specular reflections. The computational complexity and simulation time of Monte Carlo approach is less compared with the recursive and DUSTN models [101]. However, the main drawback of MCA is that, for a regular sized room, it requires to send many more rays than the number that will be received. This is because that not all rays will be intercepted by the Rx. Therefore, the same working group has developed MCA approach as detailed in the next subsection.

2.5.2.2.2 Modified Monte Carlo algorithm (MMCA)

The authors in [77] developed MCA and came up with a mixed ray-tracing-Monte Carlo algorithm for simulating multipath response for indoor WIRC channels [89]. The new method called Modified MCA (MMCA) which is faster and more accurate than classic Monte Carlo method. This is due that MMCA ensures that each ray contributes to the final channel response function each time it bounces off an obstacle. MMCA was more accurate and faster enough to calculate the room dispersion within few minutes, which is 20 times faster than DUSTIN algorithm [51]. In contrast with the recursive model [57], MMCA, is faster and more concise algorithm to simulate

the CIR $h(t)$ for indoor WIRC channels. Its computational complexity is kN_cN_r, where N_r is the number of rays [116]. MMCA is preferable in terms of reliability but might be less efficient than cavity model [44]. In [117], MMCA is extended to examine Phong reflection [118] model. Simulation results showed that the use of Phong model can lead to differences compared to Lambert model in the evaluation of the impulse response when surfaces exhibit a high specular component. The use of Bidirectional Reflectance Distribution Function (BRDF) on MMCA is reported in [119]. This is allowed for more general and accurate modelling of the reflection properties of the different reflecting surfaces. In terms of WIRC channel modelling in transportation means, the authors in [59] adopted Monte Carlo ray-tracing simulation in order to estimate the PL of WIRC channels inside an aircraft cabin. The simulation is performed based on a geometric computer-aided design (CAD) cabin model. On the other hand, in terms of VLCs, MMCA based on the Lambert-Phong pattern for single source and multiple source systems is presented in [90].

2.5.2.2.3 Modified Ceiling Bounce Model (MCBM)

The traditional CBM, however, ignored (as an approximation) the contribution of the walls to the total CIR $h(t)$. Therefore, the authors in [78] developed a MCBM based on combining the traditional CBM in [83] with the stochastic model in [69]. MCBM presents a more accurate CIR $h(t)$ with less computational complexity compared to the traditional CBM [84].

2.5.2.2.4 HAYASAKA-ITO Model

According to this model, the CIR $h(t)$ of WIRC channels is decomposed into primary reflection $h^1(t)$ $(k = 1)$ impulse response and higher-order reflections $h^{\text{high}}(t)$ $(k \geqslant 3)$ impulse response [66]. Based on the used link design, the second-order reflection has been neglected. The authors have selected the Gamma distribution to model $h^1(t)$ and hence the normalized impulse response is given as [20]

$$h^1(t) = \frac{\beta_{\text{me}}^{-\alpha_{\text{sh}}}}{\Gamma(\alpha_{\text{sh}})}\, t^{\alpha_{\text{sh}}-1}\, \exp(-\frac{t}{\beta_{\text{me}}}). \tag{2.21}$$

Here, $\Gamma(\alpha_{\mathrm{sh}})$ is the Gamma function while α_{sh} and β_{me} are characteristic parameters related to the physical parameters of the channel. On the other hand, $h^{\mathrm{high}}(t)$ has been modelled using spherical model that was mentioned previously. The most important outcomes of HAYASAKA-ITO model, that it has demonstrated that the bandwidth characteristics are dominated by the response of the primary reflection rather than the higher-order reflections, and the PL within the communications range does not depends on the FoV of the Rx.

2.6 Summary

This chapter has provided a survey of OWCs in terms of evolution, features, channel scenarios, and channel characteristics. Furthermore, we have comprehensively reviewed OWC channel measurements and models, primarily in the IR and visible light spectra. It has been shown that NDLoS link configuration can be considered as the most suitable link configuration for VLC technology. On the other hand, NDNLoS is considered as the main link design for WUVC and WIRC technologies. However, WUVCs rely upon the scattering from the particles in the atmosphere rather than diffuse reflection in WIRCs and VLCs. For WIRCs and VLCs, the main optical channel characteristics that affect the OWC link performance have been studied, including channel DC gain, RMS delay spread, frequency response, PL, and shadowing. Both channel measurement campaigns and channel models have been classified according to the environment, channel scenario, channel characteristics, the number of bounces, and the operating wavelength. It has been noticed that most VLC channel models have been extended from WIRC channel models, with the assumption that IR and visible light bands have similar optical properties due to their contiguous wavelengths. Therefore, we can conclude that more channel measurements in visible light spectrum should be carried out and explicit generic VLC channel models should be developed in order to adapt to a wide range of VLCs scenarios.

Chapter 3

A 2D Stationary One-Ring Single-Bounce RS-GBSM for VLC Single-Input Single-Output (SISO) Channels

3.1 Introduction

Although VLC channels exhibit a high degree of immunity to multipath fading, the performance of VLC systems may potentially be degraded by channel distortions and additive noise. Channel distortions due to path loss and multipath dispersion and associated ISI and the interference with the ambient light considered the main challenges that tackle VLC technology. The typical VLC link that using IM/DD is depicted in Fig. 3.1. It comprises an optical source as the Tx and a large-area PD as the Rx. The instantaneous optical intensity of the Tx is $x(t)$. While $y(t)$ is the instantaneous current that can be produced by the PD, which is the product of the PD responsivity R_λ and the integral over the PD surface. Based on propagation scenario, the light arrives the Rx through LoS path, NLoS paths, or both.

In an indoor environment, the optical wireless channel can be modelled as a LTI system with input intensity $x(t)$, output current $y(t)$, and an impulse response $h(t)$, which is fixed for a certain physical design for the Tx, Rx, and reflectors [83]. Here, the

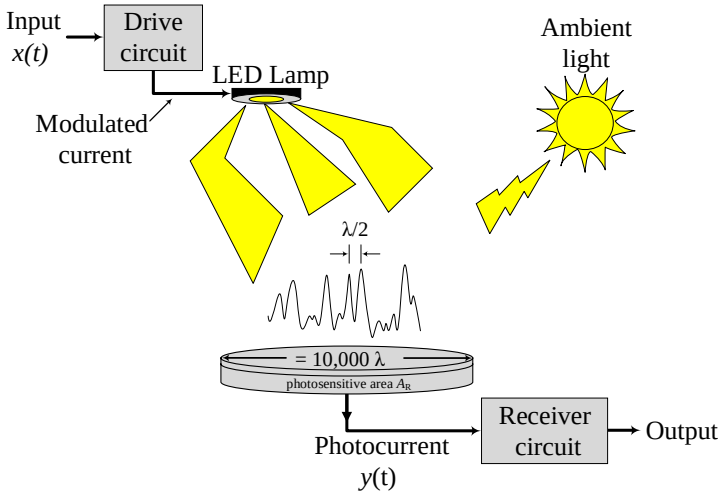

FIGURE 3.1: A generalised block diagram of VLC link using IM/DD

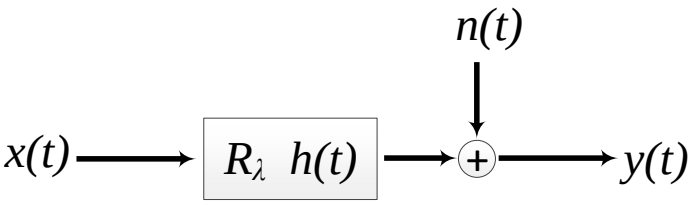

FIGURE 3.2: Equivalent baseband model of an optical wireless system using IM/DD

background light noise can be modelled as Additive White Gaussian Noise (AWGN). For An IM/DD-based optical wireless system, the equivalent baseband model that hides the high- frequency nature of the optical carrier can be shown in Fig. 3.2. Mathematically, the equivalent baseband model of an IM/DD optical wireless link can be expressed as [20]

$$y(t) = R_\lambda \; x(t) \circledast h(t) + n(t) \tag{3.1}$$

Here, $\circledast$ denotes convolution and $n(t)$ is a signal-independent AWGN. A linear time-invariant system is completely characterised by its CIR $h(t)$ [52], [20], which is then used to analyse and combat the effects of channel distortions. Therefore, the starting point for capturing VLC channel characteristics is to propose an accurate channel model and determine its CIR $h(t)$.

A considerable amount of work has been published in terms of channel modelling in IR spectrum, e.g., [16], [35], [44], [57], [59], [67], [74]–[78], [83]. Some models have been extended to VLCs such as [87], [90], [92], [93]. But visible light and IR bands exhibit different characteristics, which necessitates the development of VLC channel models. M. Uysal *et al.* investigated VLC channels using the deterministic ray tracing approach based on Zemax® in [58], [79]– [82], [96], [106], [120]. However, in this thesis we initiate a new direction of research in optical wireless channel modelling, primarily for VLCs. Here, we have extended the concept geometry-based channel models which are proposed for RF channels to model VLC channels. To the best of the authors' knowledge, this is the first geometry-based model for VLC channels. A nice feature of geometry-based channel models is that they allow a simple physical interpretation. Geometry-based and conventional ray-tracing models share the common idea to determine the relevant rays from the Tx to the Rx. The key difference between geometry-based and ray-tracing approches is that geometry-based channel models assume the scatterers are randomly distributed according to a certain probability density function, while in the ray-tracing approach the scatterer locations are stored in a database, and thus they are deterministic [52]. In terms of 2D channel modelling, the most commonly reported geometry-based models are one-ring model, two-ring model, ellipse model, and combined ellipse and two-ring model [52], [110]. Here, the first channel model forms the core of the present chapter.

This chapter is organised as follows. Section 3.2 describes the main components of a typical VLC link. Section 3.3 presents the proposed indoor VLC system model. The fundamental difference between radiometry and photometry concepts is presented in Section 3.4. The new one-ring geometry-based channel model for VLCs is introduced in Section 3.5. In Section 3.6, simulation results and analysis are presented. The comparison between the proposed one-ring model and the existing models illustrated in Section 4.6. Conclusions are finally drawn in Section 3.8.

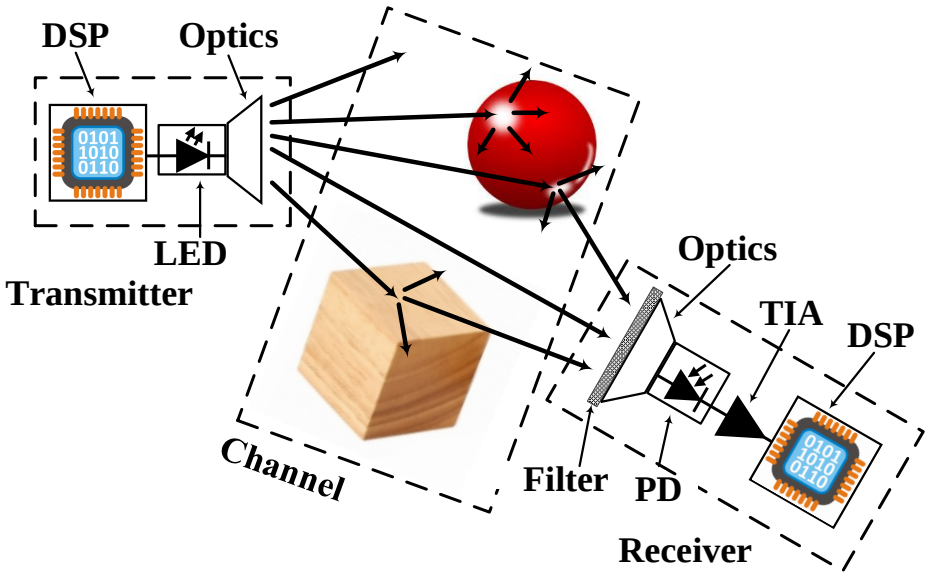

FIGURE 3.3: Typical VLC link-level.

3.2 VLC Link Model

The typical VLC link including the optical wireless channel is illustrated in Fig. 3.3. At the optical transmitter front end, the baseband signal can be manipulated by using a Digital Signal Processor (DSP). The resulting digital values are converted to an analog current using a Digital-to-Analog Converter (DAC), and this current is used to drive a LED or an array of LEDs to generate intensity-modulated light signal. Depending on the desired communication scenario, the optical signal can be passed through optical components in order to further shape the transmitted beam such as an optical collimator or a diffuser that can be employed to concentrate or broaden the beam, respectively. Thereafter, the optical signal is transmitted over the optical wireless channel. Light can arrive the optical receiver through either direct path (LoS), or indirect path (NLoS). In LoS scenario, the transmitted signal will be attenuated due to free-space path loss. While in the case of NLoS scenario, there will be additional optical losses due to absorption and reflection at the objects' surfaces.

At the optical receiver front end, an optical filter can be deposited onto the concentrator surface or inserted between the concentrator and the PD. The optical filter is normally used to reduce all out-of-band natural and artificial light signals. The optical

filter is followed by a truncated spherical non-imaging concentrator, which is attached to the PD in order to increase overall effective collection area. Using of optical filter and concentrator can highly decrease ambient noise and increase the detected power, respectively and thus improve SNR [20]. After detection, the optical signal is converted back to an electrical current which in turn is converted to an analog voltage by means of a Transimpedance Amplifier (TIA). Finally, an Analog-to-Digital Converter (ADC) is used to digitize the signal in order to extract the original transmitted bits.

3.3 Indoor VLC System Model

The proposed indoor VLC system model is illustrated in Fig. 3.4. Here, the optical source employs incoherent WLEDs as signal transmitters. Incoherent WLED lamps can increase coverage area and alleviate the need for alignment with the receiver. Here, both LoS and NDLoS communication scenarios are considered. WLED lamps usually consist of a significant number of single chips, each presenting an angular distribution following generalised Lambertian radiation pattern.

In terms of light source radiation pattern, for isotropic sources, the light intensity is the same in all directions. However, for a flat radiating surface, known as a Lambertian, the intensity falls off as the cosine of the observation angle with respect to the surface normal. The radiation characteristics of LEDs are generally modelled by means of a generalised Lambertian radiation pattern [1]. Likewise in radiation mode, the reflection pattern can be modelled using a generalised Lambertian pattern when reflecting surfaces defined as diffuse reflectors. A surface can be considered diffuse or non-specular if the maximum height of the surface irregularities h_{si} conforms to the following [20]

$$h_{\text{si}} > \frac{\lambda}{8 \sinh(\phi_{\text{R}})} \tag{3.2}$$

This roughness makes surface properties are independent of direction. Fig. 3.5(a) illustrates ideal Lambertian reflector.

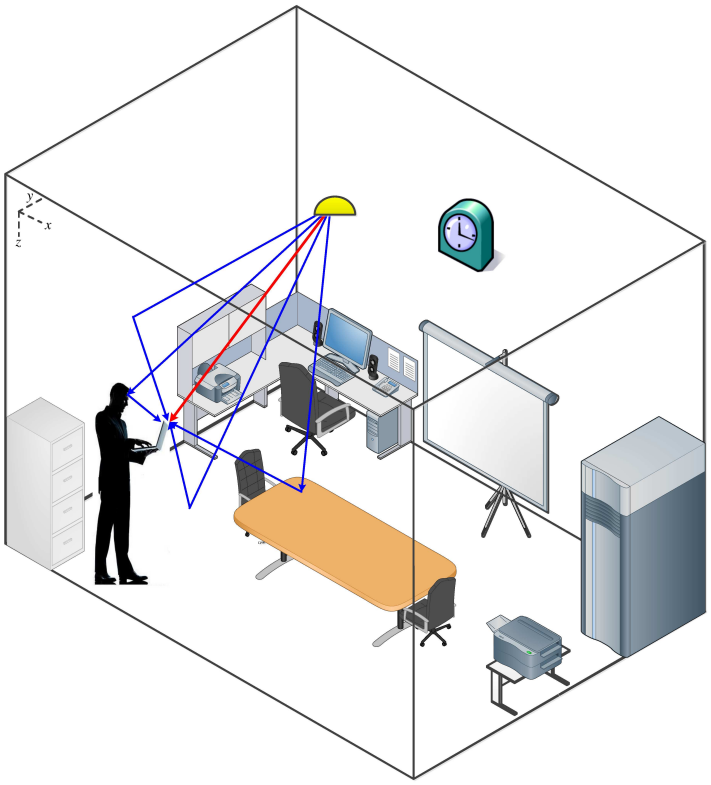

FIGURE 3.4: The proposed indoor VLC system model.

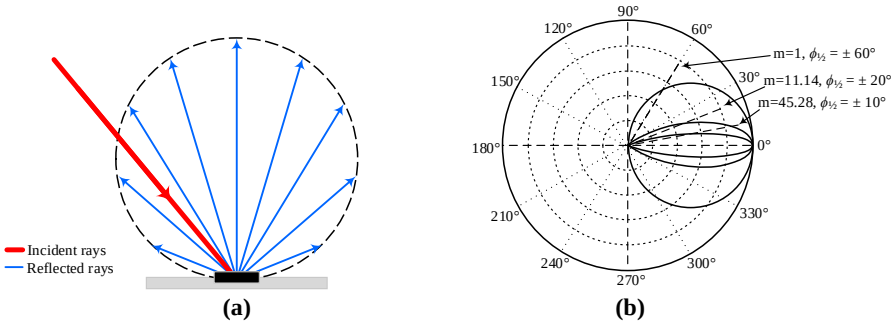

FIGURE 3.5: Normalized Lambertian pattern. (a) ideal Lambertian (diffuse) reflection. (b) Lambertian patterns with $\phi_{1/2}$ of $\pm 10°$, $\pm 20°$, and $\pm 60°$, including the respective Lambertian mode numbers m

The intensity angular distribution of generalised Lambertian pattern can be expressed as [16]

$$R(\phi_{\mathrm{T}}) = \begin{cases} \frac{m+1}{2\pi} \cos^m(\phi_{\mathrm{T}}), & \phi_{\mathrm{T}} \in [-\pi/2, \pi/2] \\ 0, & \phi_{\mathrm{T}} > \pi/2. \end{cases} \tag{3.3}$$

TABLE 3.1: Half-power angles $\phi_{1/2}$ and their respective m parameters

$\phi_{1/2}$	10°	15°	20°	30°	40°	45°	50°	60°	70°	80°
m	45.28	20	11.14	4.82	2.6	2	1.57	1	0.646	0.396

Here, ϕ_{T} is the AoD and m is mode number of the radiation lobe. Mode number can be calculated as [16]

$$m = -\frac{0.693}{\ln(\cos(\phi_{1/2}))} \tag{3.4}$$

Here, $\phi_{1/2}$ is the angle of half-power emission of the LED, namely it is the view angle when radiant intensity is half of the intensity value at 0°. Model number is specifying the directionality of the optical source, where higher m means higher directionality of the optical source. Most of LEDs have $\phi_{1/2} = 60°$, namely $m = 1$ [39]. The concepts of m and $\phi_{1/2}$ are illustrated in Fig. 3.5(b). Table 3.1 presents some m values for various values of $\phi_{1/2}$ for a generalised Lambertian pattern [39].

On the other hand, at the receiving side, the PD is modelled as a photosensitive area A_{r} as illustrated in Fig. 3.1. The PD is collecting the radiation incident at AoA ϕ_{R} smaller than the PD's FoV Ψ_{FoV}. Therefore, only rays that incident within Ψ_{FoV} will be captured. The effective collection area A_{eff} of the PD is given as [16]

$$A_{\mathrm{eff}} = \begin{cases} A_{\mathrm{r}} \cos(\phi_{\mathrm{R}}), & 0 \leq \phi_{\mathrm{R}} \leq \Psi_{\mathrm{FoV}} \\ 0, & \phi_{\mathrm{R}} > \Psi_{\mathrm{FoV}}. \end{cases} \tag{3.5}$$

Consequently, the channel DC gain can be generalised based on the Lambertian source of specific m, a PD with a certain A_{eff}, and at a specific distance between the optical source and the PD. Channel DC gain is inversely proportional to the square of the distance between the optical source and the PD (the inverse square law). As illustrated in Fig. 3.4, the PD can be integrated with end-user devices such as laptops or smartphones.

3.4 Photometry and Radiometry

Since VLCs are used for the dual propose of illumination and communication in a specific environment, it is necessary to keep the light intensity within the standard illumination criteria for that environment and to maintain the eye safety. The science of measurement of light intensity is photometry rather than radiometry. Radiometry and photometry are twin scientific disciplines concerned with the measurement of electromagnetic radiation. Radiometry is the science of measuring the radiation in any portion of the electromagnetic spectrum including optical spectrum. While photometry is the science of measuring visible light in units that are weighted according to the sensitivity of the human eye. This is due to the fact that the human eye is not equally sensitive to all wavelengths of visible light [121]. When dealing with visible light, we are mainly focusing on two types of information, namely, source information and surface information. In terms of source information, the amount of light emanating from a light source within a solid angle of one steradian (sr) is called luminous Intensity (I) and it is measured in candela (cd). Luminous flux ($\mathbf{\Phi}$), however, is often the most common measurement used to compare different light sources and can usually be found written on the pack or in the data sheets of light bulbs. Luminous flux unit of measurement is the lumen (lm). The difference between luminous Intensity and luminous flux is that luminous flux is used to measure the amount of light emitted in all directions as shown in Fig. 3.6.

In terms of surface information, the total luminous flux falling on a unit area of a surface is termed illumination (E) or illuminance. Illumination unit of measurement is lumen per square meter and commonly called lux (lx). Since it is a measurement from the source of the light, the illumination is independent of the type of surface. However, when the light bouncing off that surface towards the observer, the amount of light reflected off the surface is called luminance (L) and measured in candela per square meter ($\mathrm{cd/m^2}$). Different surfaces reflect light differently and hence, luminance is a function of reflective characteristics for each surface. Fig. 3.6 illustrates the concepts of photometric terms.

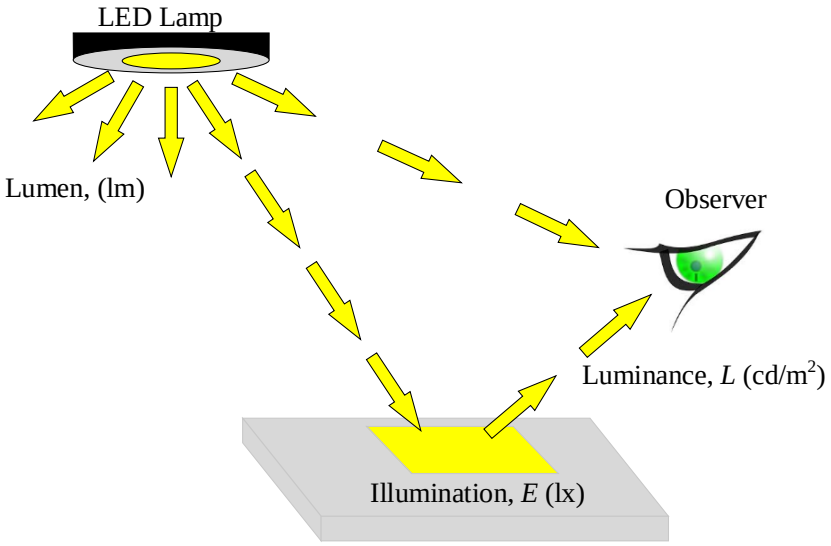

FIGURE 3.6: Photometric terms.

In order to fulfill the lighting function for the proposed VLC indoor system model, the horizontal illumination E_{hor} is assessed within in the selected environment. The luminous intensity for a Lambertian source is given as [86]

$$I = I(0)\,\cos^{m}(\phi_{\text{T}}) \tag{3.6}$$

The LoS E_{hor} at a point (x,y) is given as [98]

$$E_{\text{hor}} = \frac{I(0)\,\cos^{m}(\phi_{\text{T}})\,\cos(\phi_{\text{R}})}{(D_{\text{TR}}^{\text{LoS}})^{2}} \tag{3.7}$$

Here, $I(0)$ is the centre luminous intensity of the optical source and it is provided by the manufacturers and $D_{\text{TR}}^{\text{LoS}}$ is the LoS distance between the optical source and the PD.

3.5 Field of View (FoV) one-ring RS-GBSM

The key features of geometry-based channel models are that they provide a simple physical interpretation due to their close relationship with physical channels (real-world). Furthermore, they are mathematically tractable, flexible, and applicable to a wide range of propagation environments [52]. In this chapter, VLC channel characteristics, such as DC channel gain, RMS delay spread, and angular spread will be studied using geometry-based modelling approach. This approach provides a reasonable starting point to describe the distribution of scattering objects within an indoor environment which is lit by a WLED lamp. Here, a new 2D stationary FoV one-ring RS-GBSM for VLC SISO channels is proposed, as shown in Fig. 3.7. This model is a developed version of the well-known one-ring model, which was first introduced in [122] to model 2x2 radio MIMO wireless channels. According to this model, the location of the Tx and the Rx, as well as the location of the of local scatterers are geometrically described. Theoretically, the number of scatterers N is usually infinite and they are randomly distributed in the 2D plane.

For convenience, let us now consider a general narrowband optical wireless system in which the transmitter is a WLED lamp which acts as a fixed BS while the receiver is a PD acts as an end user device. Each transmitted wave is further assumed to be scattered (reflected off) only once. The FoV model is appropriate for describing environments, in which the BS is elevated and unobstructed, whereas the receiver is surrounded by a large number of local scatterers $S_n (n = 1, 2, ..., N)$. In case if the LoS link is interrupted, the receiver will receive signals from different directions determined only by the distribution of the local scatterers. Unlike in classical one-ring model, where the local scatterers are distributed around a ring centred on the Rx, in the proposed FoV model, the local scatterers are distributed along an arc, with radius R_{R}, centred on the PD. Here, the arc boundaries are constrained by PD's FoV Ψ_{FoV}. The direct distance between the WLED lamp and the PD is denoted by $D_{\mathrm{TR}}^{\mathrm{LoS}}$, while the indirect distance of nth transmitted light ray between the WLED lamp and nth

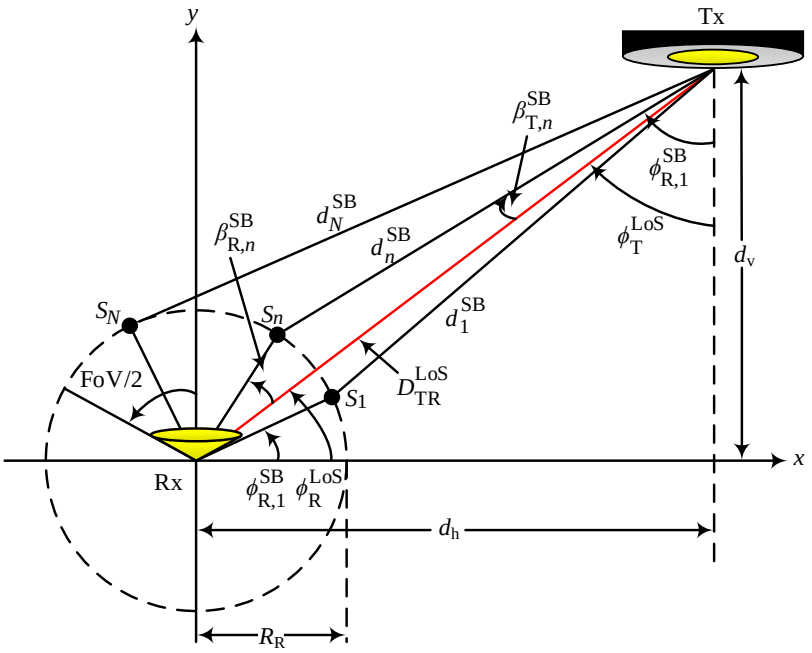

FIGURE 3.7: The proposed FoV one-ring model.

local scatterer S_n is denoted by d_n^{SB}. The AoD of the nth transmitted light ray is denoted by $\phi_{T,n}$, and the corresponding AoA is described by $\phi_{R,n}$ $(n = 1, 2, ..., N)$.

3.5.1 Reference Model for FoV one-ring RS-GBSM

In the proposed model, the LoS component of the CIR $h^{LoS}(t)$ is deterministic and given as [35]

$$h^{LoS}(t) = \frac{(m+1)\ A_r}{2\pi (D_{TR}^{LoS})^2} \cos^m(\phi_T^{LoS}) \cos(\phi_R^{LoS})\ \delta(t - \frac{D_{TR}^{LoS}}{c}). \tag{3.8}$$

Here, $\delta(.)$ is Dirac delta function and $m = 1$. In order to derive the reference model based on the proposed geometry-based model that shown in Fig. 3.7, we suppose a situation in which the nth light ray emitted from the WLED lamp travels over S_n effective scatterers, which are lying on an arc of radius R_R centred at the PD and then impinge on the PD. The reference model is based on the assumption that the number of local scatterers is infinite $S_n(n = 1, 2, ..., \infty)$. Consequently, the diffuse components

at the PD can be represented as a superposition of an infinite number of plane waves coming from different directions determined by the distribution of the local scatterers. Each scatterer S_n introduces a gain G_n. This parameter is dependent on the surface reflection coefficient ρ of the scatterer S_n and the direction of the nth incoming plane wave. To simplify the reference model, we assume that each scatterer S_n introduces an infinitesimal gain inversely proportional to the number of scatterers N, while directly proportional to the reflection coefficient parameter ρ. Hence, G_n can be expressed as $G_n = \rho/\sqrt{N}$. For SB path $(\mathrm{Tx} - S_n - \mathrm{Rx})$, the SB component of the CIR for the nth transmitted plane wave traveling from the optical source, interacting with the local scatterer S_n and then arriving at the PD, can be written as

$$h^{\mathrm{SB}}(t) = \lim_{N\to\infty} \sum_{n=1}^{N} \frac{G_n A_{\mathrm{R}}}{\pi (D_n^{\mathrm{SB}})^2} \cos(\phi_{\mathrm{T},n}) \cos(\phi_{\mathrm{R},n}). \tag{3.9}$$

With the help of Fig. 3.7, the path lengths D_n^{SB} can be expressed as $D_n^{\mathrm{SB}} = d_n^{\mathrm{SB}} + R_{\mathrm{R}}$, where d_n^{SB} can be determined by using the law of cosines as

$$d_n^{\mathrm{SB}} = \sqrt{R_{\mathrm{R}}^2 + (D_{\mathrm{TR}}^{\mathrm{LoS}})^2 - 2R_{\mathrm{R}} D_{\mathrm{TR}}^{\mathrm{LoS}} \cos(\phi_{\mathrm{R},n}^{\mathrm{SB}})}. \tag{3.10}$$

Here, D_n^{SB} represents the total distance that the nth ray travels from the Tx via S_n to the PD. From Fig. 3.7, the angle $\beta_{\mathrm{R},n}^{\mathrm{SB}}$ is the angle between $\phi_{\mathrm{R}}^{\mathrm{LoS}}$ and the $\phi_{\mathrm{R},n}^{\mathrm{SB}}$. The symbols d_{v} and d_{v} represent the vertical and horizontal distances between the optical source and the PD, respectively. Consequently, we have

$$\beta_{\mathrm{R},n}^{\mathrm{SB}} = \begin{cases} \phi_{\mathrm{R}}^{\mathrm{LoS}} - \phi_{\mathrm{R},n}^{\mathrm{SB}}, & \phi_{\mathrm{R}}^{\mathrm{LoS}} > \phi_{\mathrm{R},n}^{\mathrm{SB}} \\ \phi_{\mathrm{R},n}^{\mathrm{SB}} - \phi_{\mathrm{R}}^{\mathrm{LoS}}, & \phi_{\mathrm{R}}^{\mathrm{LoS}} < \phi_{\mathrm{R},n}^{\mathrm{SB}}. \end{cases} \tag{3.11}$$

Likewise, at the optical source side we get

$$\beta_{\mathrm{T},n}^{\mathrm{SB}} = \begin{cases} \phi_{\mathrm{T}}^{\mathrm{LoS}} - \phi_{\mathrm{T},n}^{\mathrm{SB}}, & \phi_{\mathrm{T}}^{\mathrm{LoS}} > \phi_{\mathrm{T},n}^{\mathrm{SB}} \\ \phi_{\mathrm{T},n}^{\mathrm{SB}} - \phi_{\mathrm{T}}^{\mathrm{LoS}}, & \phi_{\mathrm{T}}^{\mathrm{LoS}} < \phi_{\mathrm{T},n}^{\mathrm{SB}}. \end{cases} \tag{3.12}$$

Since AoD $\phi_{\mathrm{T},n}^{\mathrm{SB}}$ and AoA $\phi_{\mathrm{R},n}^{\mathrm{SB}}$ are interdependent for single bounced rays, the relationship can be expressed by applying the law of sines in the triangle $\mathrm{Tx} - S_n - \mathrm{Rx}$ to get

$$\phi_{\mathrm{T},n}^{\mathrm{SB}} = \arcsin(R_{\mathrm{R}} \sin(\phi_{\mathrm{R},n}^{\mathrm{SB}})/d_n^{\mathrm{SB}}). \tag{3.13}$$

Therefore, if AoD $\phi_{\mathrm{T},n}^{\mathrm{SB}}$ is assumed, it will be straightforward to determine AoD $\phi_{\mathrm{R},n}^{\mathrm{SB}}$, and the other way around.

3.5.2 Simulation Model for FoV one-ring RS-GBSM

The simulation has been carried out using MATLAB®. For simulation purposes, the number of partitions is set to 50 with special resolution 0.1 m and temporal resolution 0.5 ns. Office and meeting rooms with typical dimensions as reported in [20], [57], [96] have been considered. Commercially available LEDs [123] and PIN PD [20] have been used for simulation purposes. For both rooms, the Tx assumed to be located in the centre of the ceiling. According to [52], the reasonable value of the number of discrete scatterers N is in the range from 40 to 50 scatterers. Other simulation parameters are given in Table 3.2.

Since the number of effective scatterers is assumed to be infinite, i.e., $N \to \infty$, it results in the infinite complexity and hence the reference model cannot be implemented in practice. Therefore, a realizable simulation model that has a reasonable complexity, i.e., only finite values of N is required. In this work, AoAs $\phi_{\mathrm{R},n}^{\mathrm{SB}}$ are realizations of a random variable uniformly distributed over the interval $(-\Psi_{\mathrm{FoV}},\Psi_{\mathrm{FoV}})$. Here, the discrete AoAs $\phi_{\mathrm{R},n}^{\mathrm{SB}}$ have been computed using a modified version of Extended Method of Exact Doppler Spread (EMEDS), which is reported in [52]. The modification is done to make EMEDS fits the proposed FoV model. Modified EMEDS produces a set of discrete AoAs $\left\{\phi_{\mathrm{R},n}^{\mathrm{SB}}\right\}_{n=1}^{N}$

$$\phi_{\mathrm{R},n}^{\mathrm{SB}} = \frac{\pi}{N}(n - \frac{1}{2}) + \phi_{\mathrm{R},0}^{\mathrm{SB}}, \qquad n = 1, 2, 3....N. \tag{3.14}$$

TABLE 3.2: Link parameters used in computer simulations.

Parameters	**Office**	**Meeting Room**
Width (W)	5 m	7.5 m
Length (L)	5 m	5.5 m
Height (H)	3 m	3 m
Reflection coefficient (ρ)	0.8 [57]	
Source		
Coordinates (x, y, z)	2.55, 2.55, 3	3.75, 2.75, 3
Elevation, Azimuth	$-90°$, $0°$	
Mode number (m)	1 [123]	
Photodiode		
Elevation, Azimuth	$90°$, $0°$	
Area	1 cm^2 [20]	
Field of view (Ψ_{FoV})	$80°$ [20]	
Receive plane	1 m	
Others		
Arc radius (R_{R})	0.5 m	
Number of scatterers (N)	40 [52]	
Spatial resolution	0.1 m	
Temporal resolution	0.5 ns	

where $\phi_{\text{R},0}^{\text{SB}}$ is called the angle-of-rotation. The EMEDS reveals its best performance if the angle-of-rotation $\phi_{\text{R},0}^{\text{SB}}$ is defined as [52]

$$\phi_{\text{R},0}^{\text{SB}} = \frac{\phi_{\text{R},n}^{\text{SB}} - \phi_{\text{R},n-1}^{\text{SB}}}{4} = \frac{\pi}{4N}. \tag{3.15}$$

3.6 Results and Analysis

3.6.1 Environment Illuminance

Since VLC technology is designed to provide illumination and data transmission concurrently, lighting levels need to convenient based on environment size and the type of activity inside that environment. This concept is termed as task lighting. For typical offices or meeting rooms, daily tasks involve the use of computers, mobile phones,

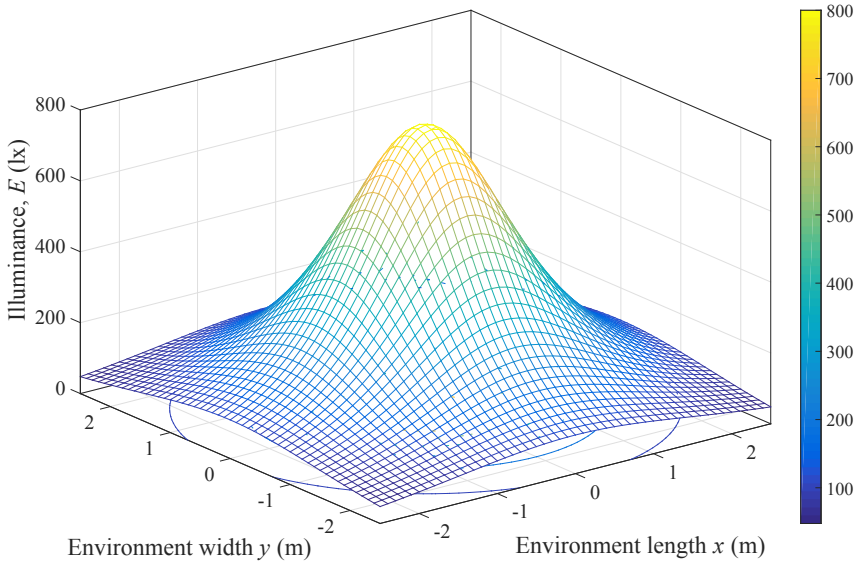

FIGURE 3.8: Illuminance (lx) of the office room with one WLED lamp located at (2.55,2.55,3).

tablets, and high quality printed paper-reading. For such environments and in accordance with the lighting standard [98], a 200-800 lx span is suitable to illuminate the environment.

In terms of office room, the illumination was assessed at 1 m above the floor. Simulation results of applying (3.7) is illustrated in Fig. 3.9. The results clearly show that the proposed environment has been lit with most effective task lighting within the standard levels. Theoretically, based on above illumination distribution we can estimate the number of LED chips that uniformly distributed per lamp. It has been estimated that we need for 1000 LED chips of a maximum luminous intensity of 10 cd and $\phi_{1/2}$ angle of 120° (commercially available LED chip) [123]. Furthermore, in order to validate our results, this figure is comparable to the results in [124].

On the other hand, it is intuitive that one WLED lamp would be not enough to light up the meetings room. Therefore, we suggested deploying four WLED lamps which are located as detailed in Table 3.2. Fig. 3.9 illustrates the simulations results of the suggested design. It can be seen that the environment has been well lit within the standard illumination levels. Furthermore, simulations results showed a good match with the experimental results in [20].

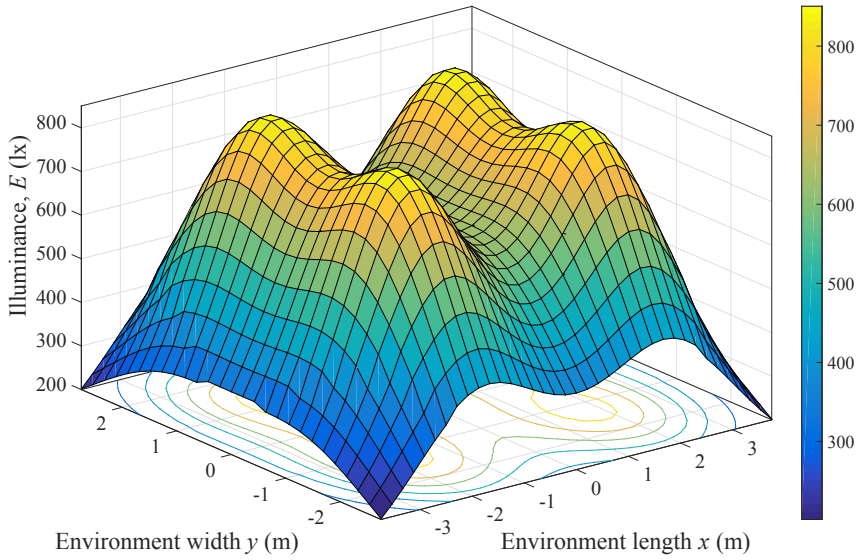

FIGURE 3.9: Illuminance (lx) of the meeting room equipped with four WLED lamps.

3.6.2 VLC Channel Characteristics

3.6.2.1 Channel Impulse Response

Regarding office room, the LoS component of the CIR is deterministic and can be expressed in (3.8). Result shows that the $h^{\mathrm{LoS}}(t)$ is a delta function scaled by 1.38×10^{-5} at 2 m distance compared to infrared $h^{\mathrm{LoS}}(t)$ of 1.2318×10^{-6} at 3.9051 m for configuration (A) in [35]. Regarding LoS and SB components of the CIR, channel characteristics have been examined in the office room at five different positions for the PD within the office, namely, A, B, C, D, and E as illustrated in Fig. 3.10. The x-y coordinates of the PD are given in Table 4.3. These coordinates represent the most probable positions of the PD. Consequently, the corresponding impulse responses are presented in Fig. 3.11.

It can be noticed from Fig. 3.11 that VLC channel can be characterised (under specific reflection coefficient ρ assumption) firstly by the distance between the optical source and the PD and secondly by the AoA with respect to the normal to the PD plane where higher received power at shorter optical path and smaller AoA. The power is

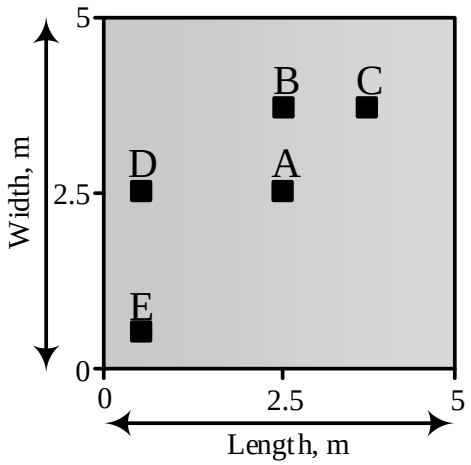

FIGURE 3.10: Top view of the proposed office room with different positions of the PD.

seen to decrease for SB impulse responses; however, they tend to add a significant amount to the total power as shown in Fig. 3.11. Also, the powers of SB components arrive much later than that from LoS component. Furthermore, in terms of AoA effect, Fig. 3.12 illustrates the behaviour of distance and AoA with respect to the PD locations for the proposed model.

3.6.2.2 Channel DC gain

Optical wireless channel DC gain can be expressed as [20]

$$H(0) = \int_0^{\infty} h(t)dt. \tag{3.16}$$

Channel DC gain in dB is related to the received power in dbW when 1 W is transmitted [94]. Consequently, VLC channel gain in dB is given as [41]

$$\mathrm{PL}_{\mathrm{LoS}}\ (\text{optical dB}) = -10\ \log_{10}\left(\int_0^{\infty} h\,(t)\,dt\right). \tag{3.17}$$

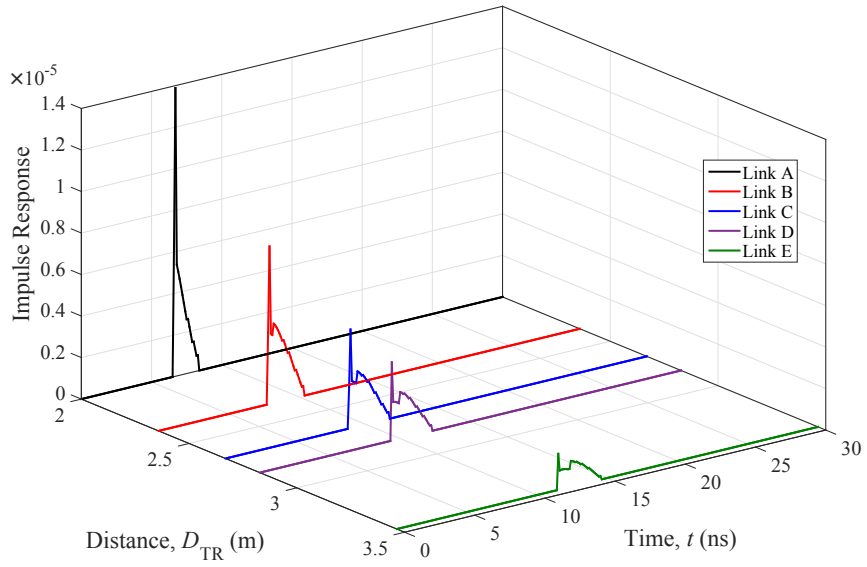

FIGURE 3.11: LoS and SB components of the CIR for links A, B, C, D, and E.

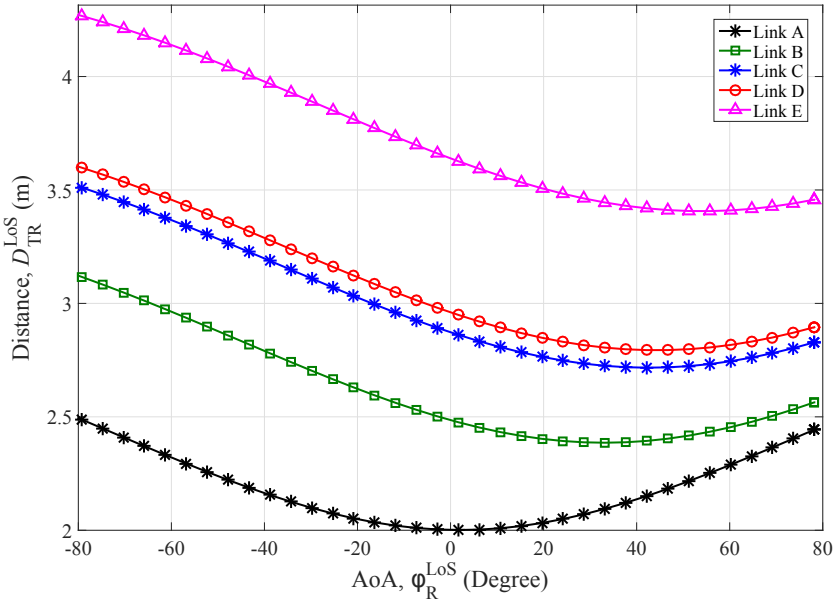

FIGURE 3.12: AoA and Distance behaviour for links A, B, C, D and E.

For the LoS link scenario, the effect of free space distance and AoA are illustrated in Fig. 3.13(a) and Fig. 3.13(b), respectively. These figures reveal that lower channel loss can be obtained when the optical rays travel shorter path and impinge the PD at closer AoA with respect to the normal of the PD plane.

In terms of the meeting room, the LoS channel gain in dB has been illustrated in

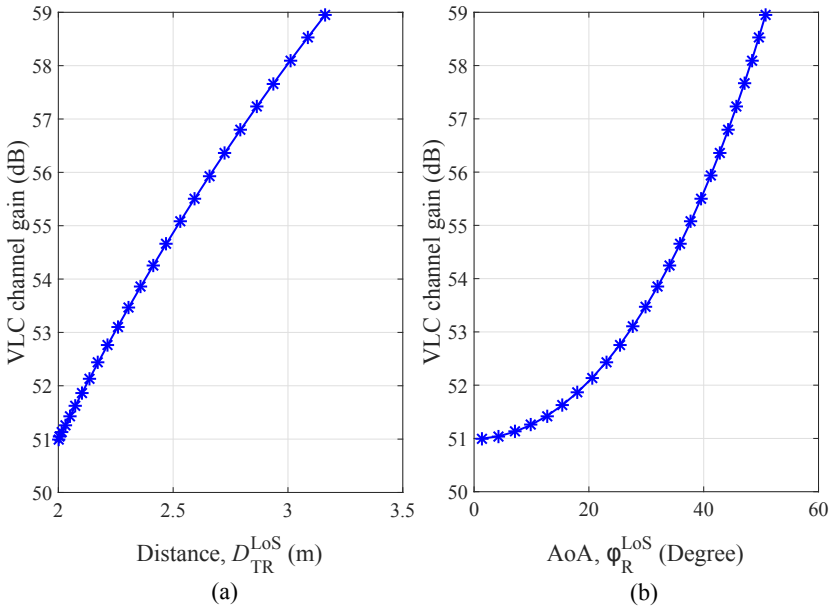

FIGURE 3.13: VLC Channel gain in dB for LoS link with respect to (a) path distance and (b) AoA.

Fig. 3.14. It can be noticed that the meeting room exhibits higher path loss compared to office room due to longer optical path length. Therefore, VLC technology is considered as a good candidate for future short-range communications.

In terms of SB link scenario, there are additional losses because, firstly, the SB optical rays travel long distance compared to LoS path before impinging the PD. Secondly, there is a portion of the optical energy will be absorbed by the scatterers, and the rest is reflected back in a diffuse fashion towards the PD. Fig. 3.15(a) and Fig. 3.15(b) illustrate VLC channel gain for link (C) when considering optical path length and AoA, respectively. Compared with Fig. 3.13, it can be observed that the SB scenario experiences higher losses. However, a different behaviour can be noticed since the shorter optical path is not necessarily experiences lower optical loss. This is due to the fact that the optical channel is characterised not only by path length but by the AoA as well.

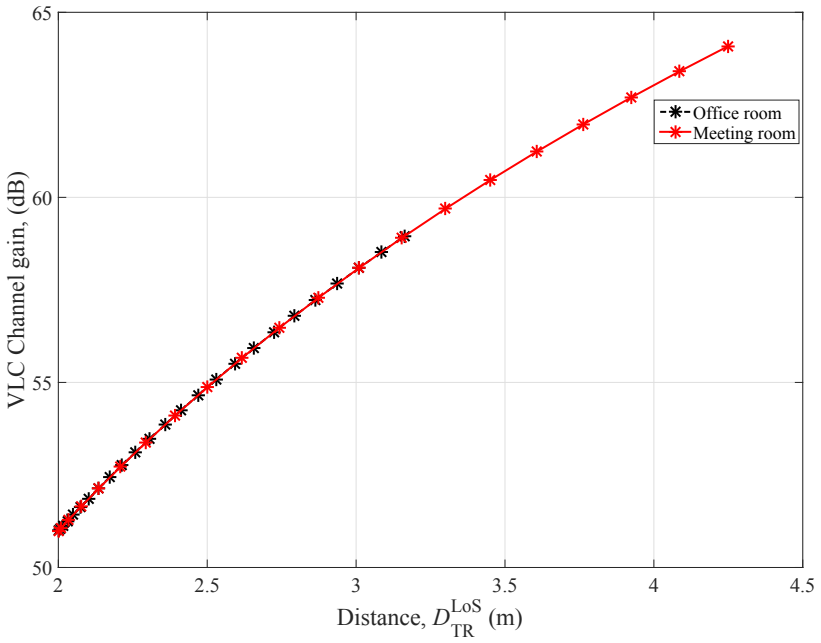

FIGURE 3.14: VLC Channel gain in dB for LoS link in office and meeting rooms with respect to optical path distance.

3.6.2.3 RMS Delay Spread

In addition to optical path length, AoD, and AoA, VLC channels are characterised by delay spread. From Fig. 3.7, we can observe that the transmitted signal travels over local scatterers along multiple paths before impinging on the PD from various directions. Consequently, one major characteristic of a multipath channel is that the optical wireless channel stretches the transmitted signal in time, so that the duration of the received signal is greater than that of the transmitted signal. This effect is known as temporal dispersion and it can be quantified by RMS delay spread D_{rms} of CIR $h(t)$ as [53]

$$D_{\text{rms}} = \sqrt{\frac{\int_{-\infty}^{\infty}(t-\mu_\tau)^2\ h^2(t)dt}{\int_{-\infty}^{\infty} h^2(t)dt}}. \tag{3.18}$$

Here, μ_τ is the mean delay spread: $\mu_\tau = \frac{\int_{-\infty}^{\infty} t\ h^2(t)dt}{\int_{-\infty}^{\infty} h^2(t)dt}$. RMS delay spread is critical in high-speed applications, where the maximum bit rate is $R_{\text{b}} \leq 1/10D_{\text{rms}}$ [54]. Furthermore, multipath dispersion will set the limit on the symbol length that can be used

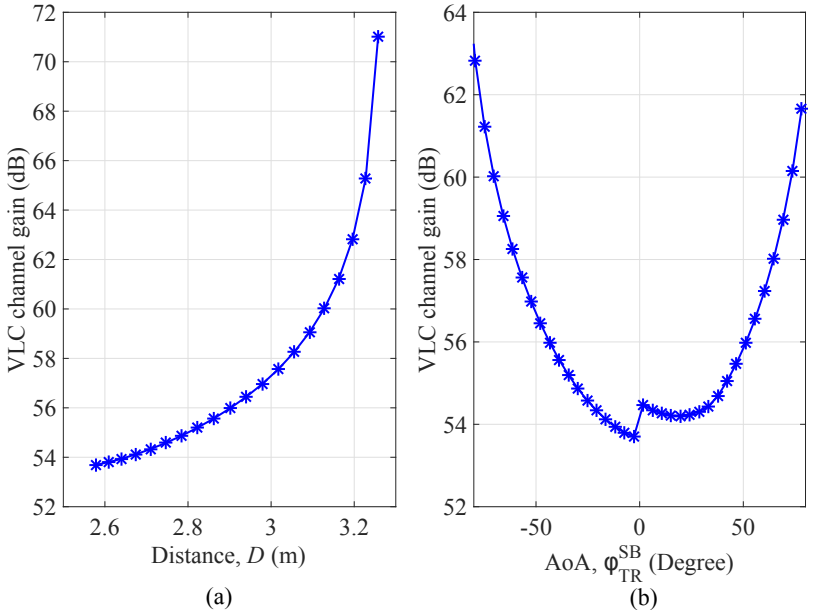

FIGURE 3.15: VLC Channel gain in dB for SB scenario (link C) with respect to (a) path distance and (b) AoA.

in order to avoid ISI [20]. Table 4.3 presents the corresponding mean delay spread for links A–E. It can be observed that the delay spread increases as PD moves away from the room centre when the optical source is fitted at the ceiling centre. The mean delay spread μ_τ for the proposed VLC channel varies from 6.91 ns to 12.46 ns with corresponding D_{rms} 0.29 ns to 0.71 ns. Hence, the maximum achievable R_{b} vary from 140 Mbps to 340 Mbps. This, in turn, illustrates the impact of delay spread on the achievable bit rate.

3.6.2.4 Rician Factor

As long as we still assume that the transmitted power is 1 W, the power ratio between the LoS and SB components can be quantified by the Rician factor K_{rf} as [20]

$$K_{\text{rf}} = \frac{P_{\text{LoS}}}{P_{\text{SB}}} \tag{3.19}$$

Rician factor and all aforementioned fundamental VLC channel characteristics for links A, B, C, D, and E are detailed in Table 4.3. It can be seen the effect of the

TABLE 3.3: VLC channel characteristics.

Link	**Distance (m)**	**PD (x,y)**	**Channel Characteristics**			
			$H(0)$	μ_τ (ns)	D_{rms}(ns)	K_{rf}
A	2.0000	2.55,2.55	1.412e-04	6.9166	0.2954	1.02
B	2.3585	2.55,3.80	0.864e-04	8.3316	0.5048	1.59
C	2.6693	3.80,3.80	0.594e-04	9.5229	0.5979	2.32
D	2.8284	0.55,2.55	0.499e-04	10.1223	0.6313	2.76
E	3.4641	0.55,0.55	0.272e-04	12.4610	0.7136	5.07

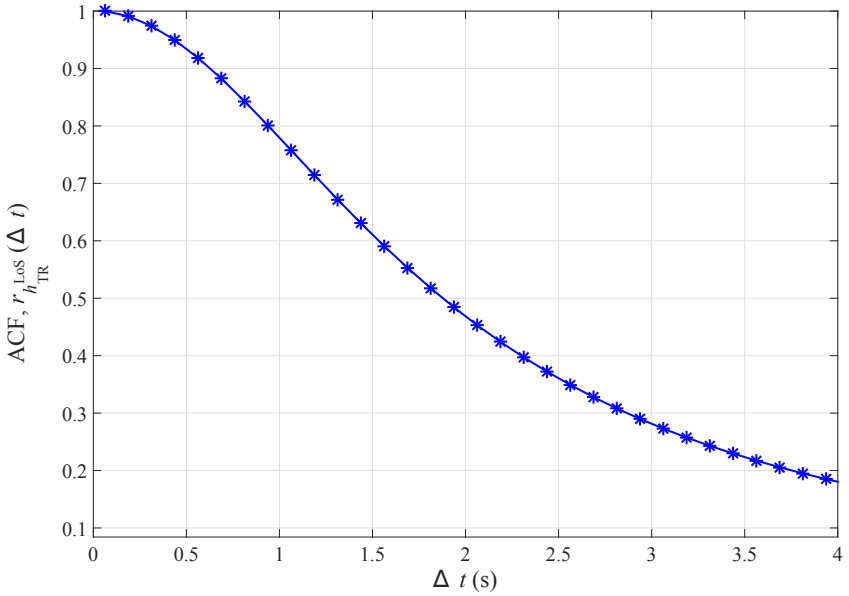

FIGURE 3.16: Time ACF of the LoS link.

position of the optical source and the PD with respect to each other in terms of optical path length, AoD, and AoA. For instance, if the PD has been moved from the room centre (Link A) to the corner (link E), the optical path length will increase and hence, DC gain will be remarkably decreased. While Rician factor and RMS delay spread will increase.

3.6.2.5 VLC Channel Time Correlation

Since VLC technology is a viable candidate for short-range indoor applications, it is expected to encounter high correlation. Therefore, channel correlation is another factor to characterise VLC channels since it highly affects VLC system performance. Thus, in this subsection, the time Autocorrelation Function (ACF) of the LoS link

will be investigated. The ACF can be expressed as [52]

$$r_{h_{\mathrm{TR}}^{\mathrm{LoS}}}(\Delta t) = E[h_{\mathrm{TR}}^{\mathrm{LoS}}(t) h_{\mathrm{TR}}^{*\mathrm{LoS}}(t+\Delta t)]. \tag{3.20}$$

Here E[.] is the statistical expectation operator. Assuming that the user is moving at a speed of 8.0 m/s, Fig. 3.16 shows that VLC channels can be highly correlated. This is due the fact that IM/DD has no frequency and phase information. This key observation leads us to conclude that VLC channel correlation is more pronounced when utilizing MIMO VLCs, and hence more efforts should be directed towards correlation mitigation in MIMO VLC channels.

3.7 Comparison of One-Ring Model with the Existing Models

In terms of one-ring model validation, Fig. 3.17 compares the impulse response computations of the proposed model with the recursive model [20], experiment results in [57], and MCB model [78], [84]. The configuration and the transceiver positions considered in the above computations were the same as in [57]. It is worthwhile emphasizing that the previous models were based on IR spectrum rather than the visible light spectrum, therefore the same IR source and refractive index have been considered to verify the validation of the proposed one-ring model. From Fig. 3.17, it can be seen that for the given transceiver positions the results obtained using one-ring model match reasonably well with those obtained in [20], [57], [78], [84]. However, the small differences between the tails of the proposed model and the other models are due to the fact that we assumed the number of scatterers N=40. Therefore, for a larger number of N, the results will be much better.

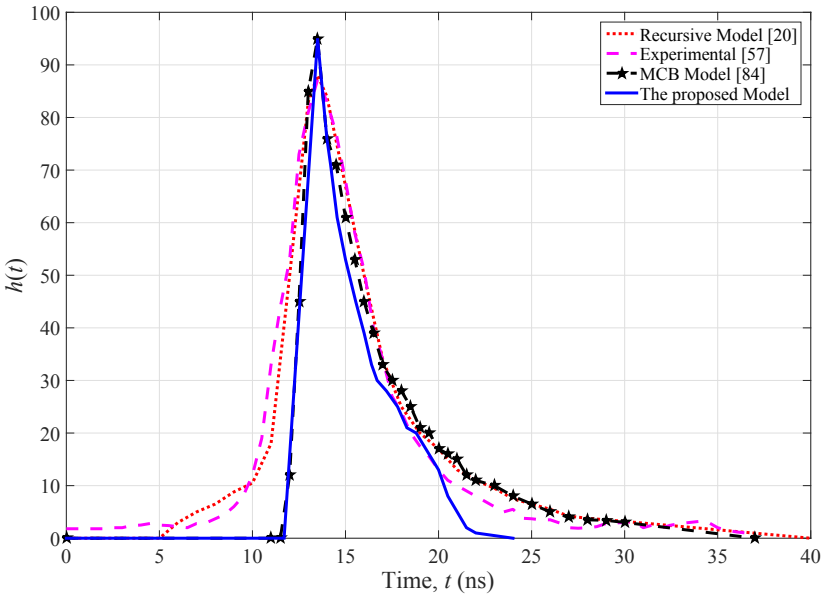

FIGURE 3.17: Comparison of one-ring model with MCB model and recursive model with the experimental results by Barry *et al.*

3.8 Summary

In this chapter, a new 2D stationary FoV one-ring RS-GBSM for VLC SISO channels is proposed. IM/DD scheme is assumed for a specific indoor environment, considering LoS and SB components. VLC channel characteristics are analysed under the constraint of PD's FoV. It has been shown that VLC channel gain, delay spread, and Rician factor (under specific reflection coefficient ρ assumption) of the proposed model depend on the optical path length, AoD, AoA and the position of the PD. Our results have further pointed out that VLC channels are highly correlated at the centre of the environment and the correlation is decreasing gradually when moving away towards the environment edges.

Chapter 4

A 2D Stationary Multiple-Bounce RS-GBSM for VLC SISO Channels

4.1 Introduction

In Chapter 3, a new 2D stationary FoV one-ring RS-GBSM, which is considered the LoS and SB components was proposed for VLC SISO channels. However, for a more realistic channel model, higher-order reflections need be to be addressed and hence the previous model should be developed. In this chapter, we expand the RS-GBSM which employs a combined two-ring model and confocal ellipse model to model VLC channels considering up to the third reflection. Two-ring and ellipse model was first proposed in [110] for modelling MIMO channels in Mobile-to-Mobile (M2M) cellular radio systems. However, it considers only first two primary reflections. Here we developed the previous model to make it more generic and able to consider the third reflection. In a similar way to that discussed in FoV one-ring model, in this model, the effective scatterers are located on regular 2D shapes, namely, two rings and a confocal ellipse. Consequently, the received signal is constructed as a sum of the following components

1. The LoS component

2. SB rays reflected off the effective scatterers located on either of the two rings or the confocal ellipse.

3. DB rays reflected off the effective scatterers located on both two rings and/or the confocal ellipse.

4. TB rays reflected off the effective scatterers located on both two rings and the confocal ellipse.

Considering primary reflections in the extended version of the prototype model makes the model sufficiently accurate, generic and adaptable to a variety of indoor scenarios. RS-GBMB is mathematically tractable and to the best of the authors' knowledge, this is the first time that the combined two-ring and confocal ellipse model is proposed to model VLC channels. Based on the proposed RS-GBSM, statistical properties of VLC channels are then investigated, such as DC channel gain, delay spread, angular spread, and Rician factor.

The rest of this chapter is organised as follows. Section 4.2 gives a general description of the proposed indoor environment including the optical source and the optical receiver. Section 4.3 introduces the combined two-ring and confocal ellipse model for VLC channels. In section 4.4, VLC channel coefficient is derived. In Section 4.5, simulation results and analysis are presented. Conclusions are finally drawn in Section 4.7.

4.2 Indoor VLC System Model

The system model is assumed to be a meeting room equipped with an incoherent WLED lamp. In order to generate a visual presentation, the system model is designed with the help of DIALux® [125]; a 3D commercially available professional light planning software. The proposed VLC link scenario is illustrated in Fig. 4.1. Here, we assumed NDLoS VLC link configuration, which considers LoS and NLoS propagation scenarios. DIALux® is a 3D software tool that has been designed for

FIGURE 4.1: Indoor VLC system model for a meeting room.

lighting planning, calculation, and visualisation. It is also supported with electronic catalogues which enable the user to select and use a wide range of luminaires from different manufacturers. For example, the latest version of the Philips lamps database is plugged-in DIALux® electronic library. The philosophy behind using DIALux® tool is that to guarantee the lighting functionality in the proposed environment.

In terms of optical source, the radiation pattern is following the generalised Lambertian radiation pattern which is expressed previously by (3.3). On the other hand, at the receiving end, a PD is modelled as an active area A_{r} collecting the radiation incident at angle ϕ_{R} smaller than Ψ_{FoV}. Here, AoD ϕ_{T}, AoA ϕ_{R}, mode number m, and $A_{\mathrm{R_{eff}}}$ have the same concepts being used in Chapter 3.

4.3 A Multiple-Bounce RS-GBSM

Since the characterisation of VLC channel is performed by its CIR, a well-defined methodology to identify all the parameters that affect CIR and hence system performance need to be clarified first. This methodology can be generalised by the following steps.

1. Introduce the type of application: indoor, outdoor, underwater, etc.

2. Specify the environment such as being offices, factories, hospitals and so on. Here task lighting should be considered accordingly.

3. Stationary/non-stationary status of the optical source and optical receiver. Such as being Fixed-to-Fixed (F2F), Fixed-to-Mobile (F2M), or M2M.

4. Specify link scenario: LoS, DLoS, NDLoS, or NDNLoS.

5. Identify the optical source /receiver positions, orientations, and specifications such as radiation pattern and FoV Ψ_{FoV}.

6. Determine link's parameters, such as the distance between the optical source and the receiver, AoD, AoA, and the attenuation due to scattering and absorption.

7. Based on the information above, CIR can be generated.

8. Finally, once CIR is generated, VLC channel characteristics can be investigated based on obtained CIR.

The generalised principle of generating CIR can be illustrated in Fig. 4.2.

In this section, we describe the proposed combined two-ring and confocal ellipse model for VLC SISO channels. Let us now consider a general VLC system where the transmitter is WLED lamp which acts as fixed BS while the receiver is a PD acts as end user device. Fig. 4.3 illustrates the geometry of the proposed 2D multiple-bounce RS-GBSM, which employs combined two-ring and confocal ellipse models. This model guarantees SB, DB, and TB within combined two-ring and confocal ellipse model, in addition to the LoS component. The definitions of key geometry parameters are presented in Table 4.1.

Referencing to Fig. 4.3, the two-ring model is proposed to mimic the scatterers around the Tx (denoted by p) and Rx (denoted by q) while the confocal ellipse model is proposed to consider the walls within the indoor environment. Suppose there are N_1 local scatterers around the Tx lying on a ring of radius R_{T} and the n_1th ($n_1 = 1, ..., N_1$) local scatterer is denoted by S^{n_1}. Similarly, assume there are N_2 local scatterers around the Rx lying on a ring of radius R_{R} and the n_2th ($n_2 = 1, ..., N_2$)

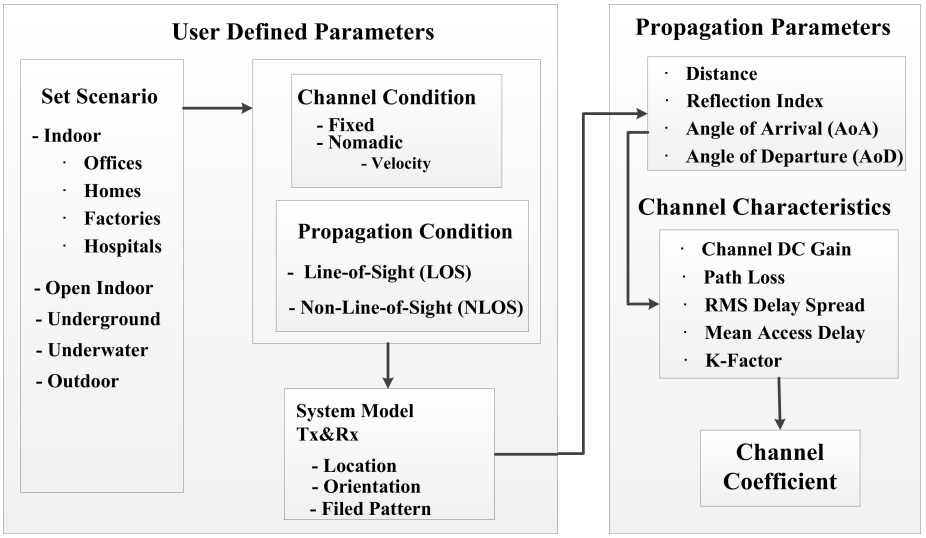

FIGURE 4.2: The generalised principle of generating CIR.

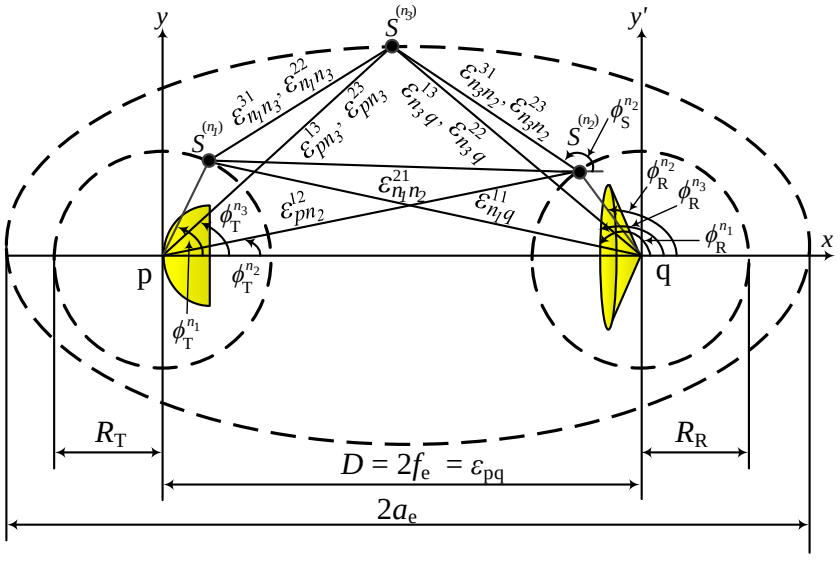

FIGURE 4.3: A generic 2D RS-GBSM for indoor VLC channels combining a two-ring model and a confocal ellipse model.

local scatterer is denoted by S^{n_2}. On the other hand, for the confocal ellipse model, N_3 local scatterers lying on an ellipse and the n_3th ($n_3 = 1, ..., N_3$) local scatterer is denoted by S^{n_3}. Ellipses are confocal, i.e., they have two common focal points (foci), which in our case coincide with the position of the Tx and Rx, respectively. The ellipse parameters a_e and b_e are denoting the semi-major axis and semi-minor axis, respectively (assuming $b_e < a_e$). The distance between the Tx and Rx is $D = 2f_e$ with f_e denoting the half length of the distance between the two focal points of ellipse

TABLE 4.1: Definitions of key geometry parameters.

Component	**Optical Path**	**Distance**
LoS	p→q	$\varepsilon_{\mathrm{pq}}$
1- SB_11	1- p→n_1→ q	1- R_{T}+ $\varepsilon^{11}_{n_1\mathrm{q}}$
2- SB_12	2- p→n_2→ q	2- $\varepsilon^{12}_{\mathrm{p}n_2}$ + R_{R}
3- SB_13	3- p→n_3→ q	3- $\varepsilon^{13}_{\mathrm{p}n_3}$ + $\varepsilon^{13}_{n_3\mathrm{q}}$
1- DB_21	1- p→n_1→n_2→ q	1- R_{T}+$\varepsilon^{21}_{n_1n_2}$+$R_{\mathrm{R}}$
2- DB_22	2- p→n_1→n_3→ q	2- R_{T}+$\varepsilon^{22}_{n_1n_3}$+$\varepsilon^{22}_{n_3\mathrm{q}}$
3- DB_23	3- p→n_3→n_2→ q	3- $\varepsilon^{23}_{\mathrm{p}n_3}$+$\varepsilon^{23}_{n_3n_2}$+$R_{\mathrm{R}}$
1- TB_31	p→n_1→n_3→n_2→ q	R_{T}+$\varepsilon^{31}_{n_1n_3}$+$\varepsilon^{31}_{n_3n_2}$+$R_{\mathrm{R}}$

and the equality $a_{\mathrm{e}}^2 = b_{\mathrm{e}}^2 + f_{\mathrm{e}}^2$ holds. According to combined two-ring and confocal ellipse model, the CIR $h(t)$, can be expressed as the superposition of the LoS and the higher-order components reflected off the local scatterers as [126]

$$h(t) = h^{\mathrm{LoS}}(t) + \sum_{i=1}^{I_{\mathrm{ls}}} \sum_{g=1}^{f_{I_{\mathrm{ls}}}(i)} h^{ig}(t). \tag{4.1}$$

Here, ($I_{\mathrm{ls}} \geq 1$) is the number of related local scattering areas, $f_{I_{\mathrm{ls}}}(i) = \frac{I_{\mathrm{ls}}!}{(I_{\mathrm{ls}}-i)!\times i!}$ denotes the total possible number of bonuses based on the number of local scattering areas, and $h^{ig}(t)$ represents the CIR of the gth scattered component consisting of i-bounced rays. For example, $h^{31}(t)$ denotes the first TB component. For indoor VLC system model shown in Fig. 4.1 with I_{ls}= 3, the proposed model framework consists of the LoS component, $f_3(1)$= 3 SB components, $f_3(2)$= 3 DB components, and $f_3(3)$= 1 TB component. The complexity in calculating the CIR grows as higher order reflections are considered. On the other hand, the contribution of the higher order reflections to the overall impulse response is significantly declining since $\left\|h^k(t)\right\| \to 0,\ k \to \infty$ [20]. It has been proved that the reflected power from the third bounce is very small, which is less than 5% in most link configurations [40]. That's why we consider the CIR for only primary reflections (up to 3) and hence (4.1) can be rewritten as

$$h(t) = h^{\mathrm{LoS}}(t) + h^{\mathrm{SB}}(t) + h^{\mathrm{DB}}(t) + h^{\mathrm{TB}}(t). \tag{4.2}$$

In order to make the proposed model more practical, we assumed the following two practical criteria: firstly, the $i-$th bounced rays are always bounced by S^{n_i} ($i \in \{1,2,3\}$) scatterers located in different local scattering areas from far to near relative to the receiver [110]. Secondly, excluding the scatterers behind optical source and out of Ψ_{FoV}. Based on these practical criteria, some i-bounced components are not necessarily to be considered.

4.4 VLC Channel Impulse Response

In this section, the CIR components of (4.2) will be rewritten in more details according to each link scenario within the proposed model.

4.4.1 The LoS Link

In the proposed model, the CIR of the LoS component is deterministic and given as [35]

$$h^{\text{LoS}}(t) = \frac{(m+1)\ A_{\text{r}}}{2\pi (D_{\text{TR}}^{\text{LoS}})^2} \cos^m(\phi_{\text{T}}^{\text{LoS}})\ \cos(\phi_{\text{R}}^{\text{LoS}})\ \delta(t - \frac{D_{\text{TR}}^{\text{LoS}}}{c}). \tag{4.3}$$

Here, $m = 1$, while the parameters in (4.3) are already defined in the previous chapter.

4.4.2 Single-Bounce Link

In general, for NDLoS link scenario, each scatterer $S^{(n_i)}$ introduces a gain $G^{(n_i)}$. This parameter is a function of the surface reflection coefficient ρ of the scatterer $S^{(n_i)}$. According to $f_{I_{\text{ls}}}(i)$ function, there are three SB subcomponents produced from Tx-ring SB_11, Rx-ring SB_12, and confocal ellipse SB_13 models. In SB links, nth transmitted plane wave from the optical source is interacting with the local scatterer $S^{(n_i)}$ once and then arrive the PD. SB subcomponents are detailed in the following subsections.

4.4.2.1 SB Components in Two-Ring Model

The first contribution of SB component of the CIR is produced from Tx-ring through the link $\mathrm{p}-n_1-\mathrm{q}$. The first SB component of the CIR for link SB_11 can be written as

$$h^{11}(t) = \sum_{n_1=1}^{N_1} \frac{G_{n_1} A_{\mathrm{r}}}{\pi(\varepsilon_{\mathrm{pq}})^2} \cos(\phi^{\mathrm{SB}}_{\mathrm{T},n_1}) \cos(\phi^{\mathrm{SB}}_{\mathrm{R},n_1}). \tag{4.4}$$

Here, $\varepsilon_{\mathrm{pq}}$ denotes the total distance through different paths between the optical source and the PD. According to Table 4.1, $\varepsilon_{\mathrm{pq}}$ can be given as

$$\varepsilon_{\mathrm{pq}} = R_{\mathrm{T}} + \varepsilon^{11}_{n_1\mathrm{q}}. \tag{4.5}$$

Accordingly, the distance $\varepsilon^{11}_{n_1\mathrm{q}}$ can be calculated by using the law of cosine in triangle $\mathrm{p}-n_1-\mathrm{q}$ as

$$\varepsilon^{11}_{n_1\mathrm{q}} = \sqrt{(R_{\mathrm{T}})^2 + (D)^2 - 2R_{\mathrm{T}}D\cos(\phi_{\mathrm{T}})}. \tag{4.6}$$

In this study, we assume an isotropic scattering along Tx-ring characterised by a uniform distribution of the AoD ϕ_{T} , i.e.,

$$\mathrm{P}(\phi_{\mathrm{T}}) = \frac{1}{\pi} \quad , \quad \phi_{\mathrm{T}} \in [-\pi/2, \pi/2]. \tag{4.7}$$

The relationship between the AoD ϕ_{T} and corresponding AoA ϕ_{R} can be found by using law of sines in the triangle $\mathrm{p}-n_1-\mathrm{q}$ as follows:

$$\phi_{\mathrm{R}} = \arcsin[\frac{R_{\mathrm{T}}\ \sin(\phi_{\mathrm{T}})}{\sqrt{(R_{\mathrm{T}})^2 + (D)^2 - 2R_{\mathrm{T}}D\ \cos(\phi_{\mathrm{T}}))}}]. \tag{4.8}$$

Since AoD ϕ_{T}, AoA ϕ_{R}, and the total distance of link SB_11 are determined, $h^{11}(t)$ can be computed using (4.4).

The second probable optical path within the two-ring model will be through the link $\mathrm{p}-n_2-\mathrm{q}$, i.e., SB_12. In this case, the scatterers S^{n_2} are lying on the Rx-ring under PD's FoV restriction. Here, we have followed the same procedure above to calculate $\varepsilon^{12}_{\mathrm{p}n_2}$, AoA ϕ_{R}, scatterers coordinates along the Rx-ring and then $h^{12}(t)$.

4.4.2.2 SB Components in Ellipse Model

The last probable optical path will be within the confocal ellipse model through the link $\mathrm{p} - n_3 - \mathrm{q}$. The same assumption above ($\phi_{\mathrm{R}} \backsim U(0, 1/\mathrm{FoV}),\ \phi_{\mathrm{R}} \in [0, \mathrm{FoV}]$) can be used in confocal ellipse model. The SB component of the CIR for link SB_13 can be written as

$$h^{13}(t) = \sum_{n_3=1}^{N_3} \frac{G_{n_3} A_{\mathrm{r}}}{\pi(\varepsilon_{\mathrm{pq}})^2} \cos(\phi^{\mathrm{SB}}_{\mathrm{T},n_3}) \cos(\phi^{\mathrm{SB}}_{\mathrm{R},n_3}). \tag{4.9}$$

Based on pure ellipse properties, the distance $\varepsilon_{\mathrm{pq}}$ can be expressed as

$$\varepsilon_{\mathrm{pq}} = 2a_{\mathrm{e}} = \varepsilon^{13}_{\mathrm{p}n_3} + \varepsilon^{13}_{n_3\mathrm{q}}. \tag{4.10}$$

According to law of cosines in triangle $\mathrm{p} - n_3 - \mathrm{q}$, the path length between the focal point and a specific scatterer is given as

$$\varepsilon^{13}_{\mathrm{p}n_3} = \sqrt{(\varepsilon^{13}_{n_3\mathrm{q}})^2 + (2f_{\mathrm{e}})^2 - 2(\varepsilon^{13}_{n_3\mathrm{q}})(2f_{\mathrm{e}})\cos(\phi_{\mathrm{R}})}. \tag{4.11}$$

Based on ellipse properties and after some manipulation, we can get the path length $\varepsilon^{13}_{\mathrm{p}n_3}$ as a function of AoA ϕ_{R}

$$\varepsilon^{13}_{\mathrm{p}n_3} = \frac{a_{\mathrm{e}}^2 + f_{\mathrm{e}}^2 - 2af_{\mathrm{e}}\cos(\phi_{\mathrm{R}})}{a_{\mathrm{e}} - f_{\mathrm{e}}\cos(\phi_{\mathrm{R}})}. \tag{4.12}$$

Substituting (5.17) to (5.16), we get

$$\varepsilon^{13}_{n_3\mathrm{q}} = \frac{b_{\mathrm{e}}^2}{a_{\mathrm{e}} - f_{\mathrm{e}}\cos(\phi_{\mathrm{R}})}. \tag{4.13}$$

Applying the laws of sines to the triangle $\mathrm{p} - n_3 - \mathrm{q}$ in order to find the relationship between the AoA ϕ_{R} and AoD ϕ_{T} for ellipse scattering region, we get

$$\phi_{\mathrm{T}} = \arcsin[\frac{b_{\mathrm{e}}^2 \cos(\phi_{\mathrm{R}})}{a_{\mathrm{e}}^2 + f_{\mathrm{e}}^2 + 2a_{\mathrm{e}}f_{\mathrm{e}}\cos(\phi_{\mathrm{R}})}]. \tag{4.14}$$

Now, $h^{13}(t)$ can be determined by substituting AoD ϕ_{T}, AoA ϕ_{R} and path length $2a_{\mathrm{e}}$ in (4.4). Once the path lengths $\varepsilon^{13}_{\mathrm{p}n_3}$ and $\varepsilon^{13}_{n_3\mathrm{q}}$ are calculated, the scatterers coordinates can be determined either through $x_{n_3} = \varepsilon^{13}_{n_3\mathrm{q}} \cos(\phi_{\mathrm{R}})$, $y_{n_3} = \varepsilon^{13}_{n_3\mathrm{q}} \sin(\phi_{\mathrm{R}})$, or by using intersection between the focal points and the ellipse.

4.4.3 Double-Bounce Link

According to $f_{I_{\mathrm{ls}}}(i)$ function, there are three DB subcomponents produced from the combined two-ring and confocal ellipse model, i.e., SB_21, SB_22, and SB_23. In terms of DB components of the CIR, nth transmitted plane wave from the optical source is interacting with the local scatterer $S^{(n_i)}$ first, then reflecting off a local scatterer $S^{(n_i)}$ and then arrive the PD, here, $i \in \{1, 2, 3\}$. However, the first criterion, which is referred in Section 4.3 must apply. DB subcomponents are detailed in the following subsections.

4.4.3.1 DB Components in Two-Ring Model

The first DB components within the two-ring model are generated through DB_21 link. Here, both AoA and AoD are generated using the same methodology that used in section 4.4.2. Each optical ray leaves the Tx with specific AoD will collide firstly one of the scatterers which are lying on the Tx-ring. Secondly, the scattered secondary rays will strike another scatterer located on the Rx-ring and then collide the PD with random AoA. The DB component of the CIR for link DB_21 can be written as

$$h^{21}(t) = \sum_{n_1,n_2=1}^{N_1,N_2} \frac{G_{n_i} A_{\mathrm{r}}}{\pi(\varepsilon_{\mathrm{pq}})^2} \cos(\phi^{\mathrm{DB}}_{\mathrm{T},n_{1,2}})^m \cos(\phi^{\mathrm{DB}}_{\mathrm{R},n_{1,2}}). \tag{4.15}$$

According to Table 4.1, $\varepsilon_{\mathrm{pq}}$ can be written as

$$\varepsilon_{\mathrm{pq}} = R_{\mathrm{T}} + \varepsilon^{21}_{n_1 n_2} + R_{\mathrm{R}} \tag{4.16}$$

Here, the distance, $\varepsilon^{21}_{n_1 n_2}$ can be expressed as

$$
\begin{aligned}
(\varepsilon_{n_1 n_2}^{21})^2 =& (\varepsilon_{n_1 \mathrm{q}}^{11})^2 + (R_{\mathrm{R}})^2 \\
& - 2(\varepsilon_{n_1 \mathrm{q}}^{11}) R_{\mathrm{R}} \cos(\phi_{\mathrm{R}}^{n_1} - \phi_{\mathrm{R}}^{n_2}).
\end{aligned} \tag{4.17}
$$

Furthermore, the optical path length that taken by each ray can be calculated geometrically based on the scatterers coordinates along both Tx-ring and Rx-ring. The scatterers coordinates along the Tx-ring are $x_{n_1} = R_{\mathrm{T}} \cos(\phi_{\mathrm{T}})$, $y_{n_1} = R_{\mathrm{T}} \sin(\phi_{\mathrm{T}})$. On the other hand, the scatterer coordinates along the Rx-ring can be written as $x_{n_2} = D - R_{\mathrm{R}} \cos(\phi_{\mathrm{R}})$, $y_{n_2} = R_{\mathrm{R}} \sin(\phi_{\mathrm{R}})$. Since the coordinates of each scatterer have been determined, the optical path length can be obtained by applying trigonometry and hence determine $h^{21}(t)$.

4.4.3.2 DB Components in Combined Model

Unlike the first DB component, the other two DB components are generated within the combined two-ring and confocal ellipse model. These components are $h^{22}(t)$ and $h^{23}(t)$, which are generated through links DB_22 and DB_23, respectively. The DB components of the CIR for links DB_22 and DB_22 can be written as

$$
h^{22}(t) = \sum_{n_1, n_3 = 1}^{N_1, N_3} \frac{G_{n_{2,3}} A_{\mathrm{r}}}{\pi(\varepsilon_{\mathrm{pq}})^2} \cos(\phi_{\mathrm{T},n_{1,3}}^{\mathrm{DB}})^m \cos(\phi_{\mathrm{R},n_{1,3}}^{\mathrm{DB}}) \tag{4.18}
$$

and

$$
h^{23}(t) = \sum_{n_2, n_3 = 1}^{N_2, N_3} \frac{G_{n_{2,3}} A_{\mathrm{r}}}{\pi(\varepsilon_{\mathrm{pq}})^2} \cos(\phi_{\mathrm{T},n_{2,3}}^{\mathrm{DB}})^m \cos(\phi_{\mathrm{R},n_{2,3}}^{\mathrm{DB}}). \tag{4.19}
$$

Here, the distance $\varepsilon_{\mathrm{pq}}$ in (4.18) and (4.19) can be found with the help of Table 4.1. Before going further in determining other path lengths, it is worth to mention that there are equal distances shared between SB and DB, i.e., $\varepsilon_{\mathrm{p}n_3}^{13} = \varepsilon_{\mathrm{p}n_3}^{23}$ and $\varepsilon_{n_3\mathrm{q}}^{13} = \varepsilon_{n_3\mathrm{q}}^{22}$. Likewise, there are equal distances shared between DB and TB, specifically, $\varepsilon_{n_1 n_3}^{22} = \varepsilon_{n_1 n_3}^{31}$ and $\varepsilon_{n_3 n_2}^{22} = \varepsilon_{n_3 n_2}^{31}$.

The optical path lengths $\varepsilon_{n_1 n_3}^{22}$ and $\varepsilon_{n_3 n_2}^{23}$ for DB component (or $\varepsilon_{n_1 n_3}^{31}$ and $\varepsilon_{n_3 n_2}^{31}$ for DB component) can be determined by using the method of intersection between an ellipse

and a line. By using this method, we can assume that the incident/reflected rays can be represented by lines intercepted at the scatterer S^{n_3} (or $x_{1_{n_3}}, y_{1_{n_3}}$). According to the ellipse formula, if the centre of ellipse is moved by $x = h_{\rm e}$ and $y = k_{\rm e}$, the ellipse equation can be written as [127]

$$\frac{(x-h_{\rm e})^2}{a_{\rm e}^2} + \frac{(y-k_{\rm e})^2}{b_{\rm e}^2} = 1 \quad , \quad a_{\rm e} > b_{\rm e}. \tag{4.20}$$

Slope-Intercept form of the line is given by

$$y = m_{\rm s} x + c_{\rm int}. \tag{4.21}$$

Here, $m_{\rm s}$ and $c_{\rm int}$ are the slope of the line and y-axis intercept, respectively. The intersection points are given by

$$x_{(1,2)_{n_3}} = \frac{h_{\rm e} b_{\rm e}^2 - m_{\rm s} a_{\rm e}^2 \varepsilon \pm a_{\rm e} b_{\rm e} \sqrt{a_{\rm e}^2 m_{\rm s}^2 + b_{\rm e}^2 - \delta^2 - k_{\rm e}^2 + 2\delta k_{\rm e}}}{a_{\rm e}^2 m_{\rm s}^2 + b_{\rm e}^2} \tag{4.22}$$

and

$$y_{(1,2)_{n_3}} = \frac{b_{\rm e}^2 \delta + k_{\rm e} a_{\rm e}^2 m_{\rm s}^2 \pm a_{\rm e} b_{\rm e} m \sqrt{a_{\rm e}^2 m_{\rm s}^2 + b_{\rm e}^2 - \delta^2 - k_{\rm e}^2 + 2\delta k_{\rm e}}}{a_{\rm e}^2 m_{\rm s}^2 + b_{\rm e}^2}. \tag{4.23}$$

Here, $\varepsilon = c_{\rm int} - k_{\rm e}$ and $\delta = c_{\rm int} + m_{\rm s} h_{\rm e}$. The key assumption is that the scatterer point (x_{n_2}, y_{n_2}) at the Rx-ring should satisfy the equation of any line pass through that point and hence

$$y_{n_2} = x_{n_2} m_{\rm s} + c_{\rm int}. \tag{4.24}$$

Here, $x_{n_2} = R_{\rm R}\cos(\phi_{\rm R})$, $y_{n_2} = R_{\rm R}\sin(\phi_{\rm R})$. In order to create a relation between the two-ring and the ellipse scattering regions for double and triple bounces, we introduced one more parameter, i.e., the Angle of Scattering (AoS) off the Rx-ring and it is denoted by $\phi_{\rm S}$. Note that the AoD $\phi_{\rm T}$, AoS $\phi_{\rm S}$ and AoA $\phi_{\rm R}$ are independent for DB and TB rays, while AoD $\phi_{\rm T}$ and AoA $\phi_{\rm R}$ are interdependent for SB rays. The angle $\phi_{\rm S}$ can be generated randomly and the slop in (4.24) is computed by

$$m = -\tan(\phi_{\rm S}). \tag{4.25}$$

While the y-axis intercept coordinate is

$$c_{\text{int}} = y_{n_2} - x_{n_2} m_{\text{s}}. \tag{4.26}$$

The coordinates of the above line can be obtained by substituting above coordinates and equations (4.25) and (4.26), in (4.21) to get

$$y = x\ \tan(\phi_{\text{S}}) + [R_{\text{R}}\ \sin(\phi_{\text{R}}) - (R_{\text{R}}\ \tan(\phi_{\text{S}})\ \cos(\phi_{\text{R}}) + f_{\text{e}})]. \tag{4.27}$$

Based on above assumption, the path length $\varepsilon^{23}_{n_3 n_2}$ (or $\varepsilon^{31}_{n_3 n_2}$) can be written as

$$\varepsilon^{31}_{n_3 n_2} = \sqrt{(x_{1_{n3}} - x_{n_2})^2 + (y_{1_{n3}} - y_{n_2})^2}. \tag{4.28}$$

The path length $\varepsilon^{22}_{n_1 n_3}$ (or $\varepsilon^{31}_{n_1 n_3}$) can be obtained as

$$\varepsilon^{31}_{n_1 n_3} = \sqrt{(x_{1_{n3}} - x_{n_1})^2 + (y_{1_{n3}} - y_{n_1})^2}. \tag{4.29}$$

It can be noticed from (4.28) and (4.29) that only $(x_{1_{n_3}}, y_{1_{n_3}})$ is considered, while $(x_{2_{n_3}}, y_{2_{n_3}})$ have been ignored. This is due to the fact that these optical paths do match the second criterion that imposed in Section 4.3.

4.4.4 Triple-Bounce Link

Applying the criterion of (4.1) produces only one TB component, namely, $h^{31}(t)$, and thus it can be expressed as

$$h^{31}(t) = \sum_{n_1,n_2,n_3=1}^{N_1,N_2,N_3} \frac{G_{n_{1,2,3}} A_{\text{r}}}{\pi(\varepsilon_{\text{pq}})^2}\ \cos(\phi^{\text{TB}}_{\text{T},n_{1,2,3}})^m\ \cos(\phi^{\text{TB}}_{\text{R},n_{1,2,3}}). \tag{4.30}$$

Here, $f_I(i) = 1$ and ε_{pq} denotes the total distance considering triple reflections between the optical source and the PD through link TB_31, as detailed in Table 4.1. Although the TB $h^{31}(t)$ scattered components are less probable to be captured by the PD, they are still contributing to the total scattered power. Furthermore, the effect of above

second criterion can be significant. In this case, each optical ray leaves the optical source with specific AoD ϕ_{T}, will collide firstly one of the scatterers which are laying on the Tx-ring. Secondly, the scattered secondary ray will strike another scatterer that located on surrounded ellipse and thirdly, will collide with a scatterer which is laying on the Rx-ring and then captured by the PD with random AoA ϕ_{R} within Ψ_{FoV}. Consequently, based on the first criterion of Section 4.3, the only possible optical path for TB component is $\mathrm{p} - n_1 - n_3 - n_2 - \mathrm{q}$. The main parameters such as AoD ϕ_{T} and AoA ϕ_{R} can be determined by following the same methodology that used in subsections 4.4.2 and 4.4.3. Here, the optical path lengths $\varepsilon^{31}_{n_1 n_3}$ and $\varepsilon^{31}_{n_3 n_2}$ can be determined by using the method of intersection between an ellipse and a line twice. Firstly between the Tx-ring and the ellipse and then between the ellipse and the Rx-ring. Finally applying (4.30) in order to obtain $h^{31}(t)$.

4.5 Results and Analysis

In performing simulations, the entries of the environmental parameters are summarised in Table 4.2. Based on the proposed combined tow-ring and an ellipse model, VLC channel caracteristics will be investigated in this section. This is due to the fact that the design, implement and operate an efficient VLC system requires that the characteristics of the optical wireless channel are well investigated.

4.5.1 Channel Impulse Response

VLC channel gain is related to the average received power P_{r} as $P_{\mathrm{r}} = P_{\mathrm{t}}\ H(0)$, P_{t} denotes to the average transmitted power. It will be convenient to compare results under the assumption that the transmitted power is 1 W. According to (4.2), the CIR of VLC channel consisting of $h^{\mathrm{SB}}(t)$, $h^{\mathrm{DB}}(t)$, and $h^{\mathrm{TB}}(t)$ in addition to the LoS component, namely, $h^{\mathrm{LoS}}(t)$. Firstly, the LoS $h^{\mathrm{LoS}}(t)$ component and SB $h^{\mathrm{SB}}(t)$ components are illustrated in Fig. 4.4. In Fig. 4.4(a), all the components including the LoS one are presented. While only SB $h^{\mathrm{SB}}(t)$ components are shown in Fig. 4.4(b). The total

TABLE 4.2: Model Parameters used in computer simulations.

Model Parameters	
semi-major a & semi-minor b axes	3 m, 1.5 m
ρ_{wall} (Brick painted white)	0.8 [57]
$\rho_{\text{scatterers}}$	0.6
Optical Source Parameters	
Type	LG F3630TC1N5B [125]
Mode number (m)	1 [125]
Photodiode Parameters	
Area (A_{r})	1 cm^2 [20]
Field of view (Ψ_{FoV})	80° [20]
Other Parameters	
Number of scatterers (N)	40 [52]
Ring radius ($R_{\text{T}}, R_{\text{R}}$)	1 m

power carried by SB components is presented in Fig. 4.4(c). Secondly, the DB $h^{\text{DB}}(t)$ components are illustrated in Fig. 4.5. Fig. 4.5(a), illustrates all DB individually. On the other hand, the total power carried by DB components is given in Fig. 4.5(b). Thirdly, since there is only one probable TB component within the proposed VLC channel model, Fig. 4.6 illustrates TB component $h^{\text{TB}}(t)$. Finally, since the CIR of VLC channel based on the proposed model is the sum of all above components, the total power which arrives the PD is presented in Fig. 4.7.

4.5.2 RMS Delay Spread

Due to the difference in propagation length of the various optical paths, the received signal is dispersed over time. This will induce multipath temporal dispersion at receiving side. The temporal dispersion can be quantified by the channel RMS delay spread D_{rms} as (2.3) states. RMS delay spread is critical in high-speed applications, where the maximum bit rate $R_{\text{b}} \leq 1/10D_{\text{rms}}$ [54]. RMS delay spread results are detailed in Table 4.3.

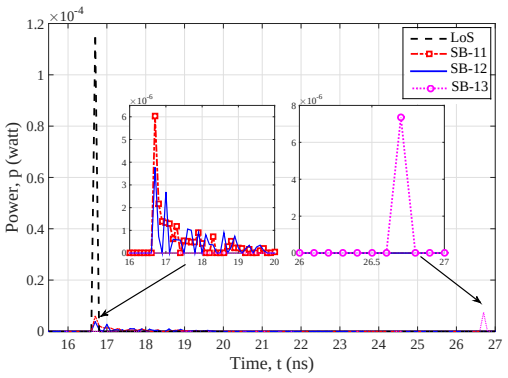

(a) LoS $h^{\mathrm{LoS}}(t)$ and SB $h^{\mathrm{SB}}(t)$ components

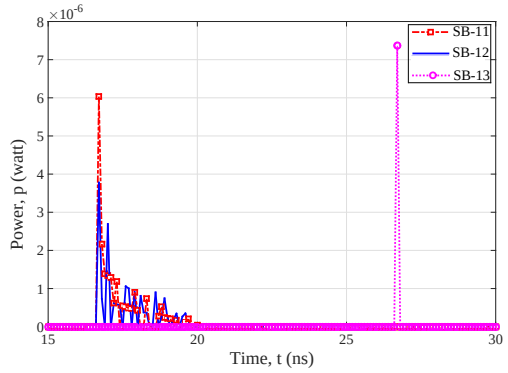

(b) SB $h^{\mathrm{SB}}(t)$ components

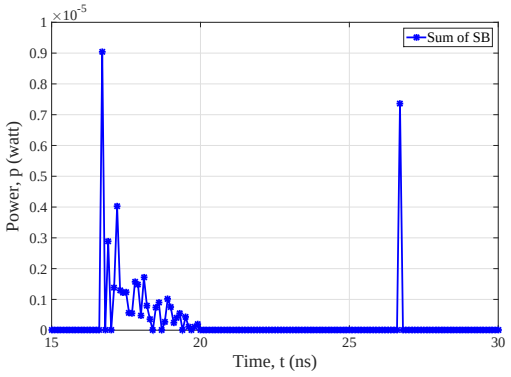

(c) Total power of SB $h^{\mathrm{SB}}(t)$ components

FIGURE 4.4: VLC CIR (a) LoS and SB, (b) SB, and (c) Sum of SB.

4.5.3 Rician Factor

If we keep the assumption of the transmitted power as 1 W valid, the power ratio between the LoS and the NLoS links can be quantified by the Rician factor, which is given as [20]

$$K_{\mathrm{rf}} = \frac{P_{\mathrm{LoS}}}{P_{\mathrm{NLoS}}}. \tag{4.31}$$

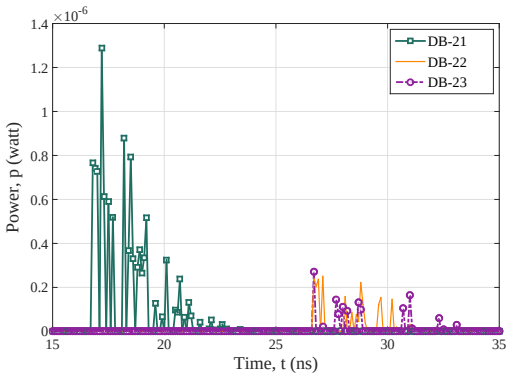

(a) DB $h^{\mathrm{SB}}(t)$ components

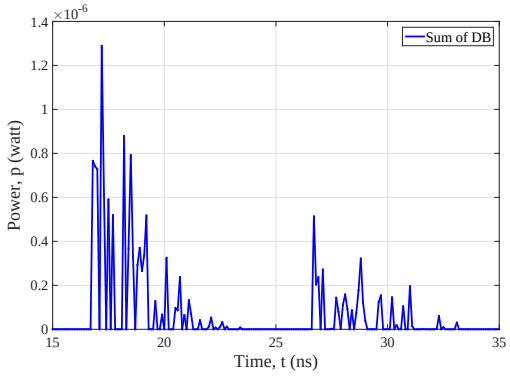

(b) Total power of DB $h^{\mathrm{SB}}(t)$ components

FIGURE 4.5: VLC CIR (a) DB and (b) Sum of DB.

TABLE 4.3: VLC Channel Characteristics.

	LoS	**SB_11**	**SB_12**	**SB_13**	**DB_21**	**DB_22**	**DB_23**	**TB_31**
Received Power (W)	0.1146e-03	12.778e-06	11.239e-06	7.3638e-06	8.7387-06	1.4423e-06	1.643e-06	4.3894e-07
Mean Access Delay (ns)	16.7	17.129	17.158	26.7	17.743	27.966	29.161	29.722
RMS Delay Spread (ns)	0	0.47092	0.62552	0	0.90587	1.3227	1.8323	1.7832
K_Factor	1	3.6517			9.6914			261.07

All above fundamental channel characteristics are presented in Table 4.3. In term of channel DC gain, the theoretical total received power is 0.1582 mW. The LoS components carry 0.1146 mW (72.42% of the total received power). While the powers carried by SB_11 and SB_12 components are 12.778 μW and 11.239 μW, respectively, and it is further decrease for SB_13 components to be 7.3638 μW because of the longer path length and larger AoD and/or AoA that ellipse made with the Tx and/or Rx, with respect to the normal on the Tx or Rx planes. Therefore SB components carry 31.38 μW (19.83%). On the other hand, for DB model, the power carried by DB_21 components is 8.7387 μW. It can be noted that the powers carried by DB_21 and SB_13 components are close to some extent although DB_21 components have shorter

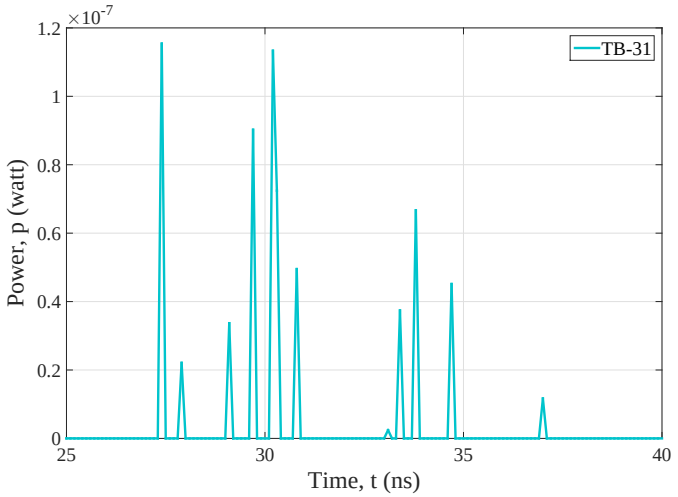

FIGURE 4.6: VLC CIR of TB $h^{\mathrm{TB}}(t)$

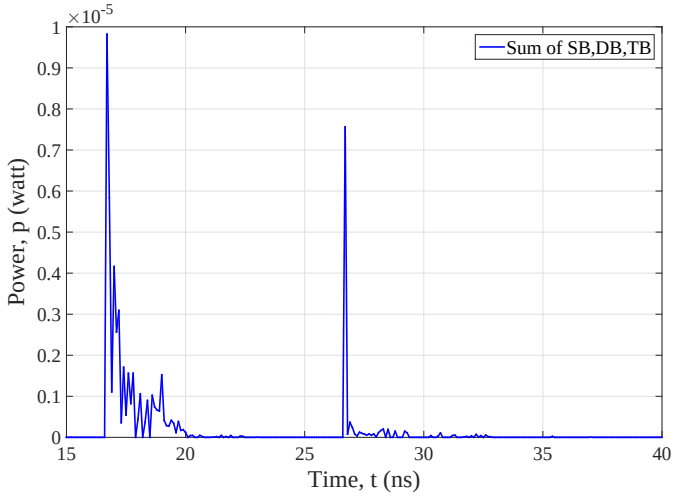

FIGURE 4.7: VLC CIR of Combined model.

path length and this is due to the higher losses resulting from ρ_{scaterer} compared with ρ_{wall}. DB_22 and DB_23 components carry 1.4423 μW and 1.643 μW, respectively because of the long path length compared with DB_21. Hence DB components carry 1.1824 μW (7.47%). Finally, the power carried by TB_31 components is no more 0.43894 μW (0.28%) since it is pass longer path length and scattered triple.

In term of the RMS delay spread, it is obvious that the delay is related to the path length. Furthermore it is worth to notice that DB_21 components arrive much earlier than DB_22 and DB_23 components and hence overlapping with SB_11 and SB_12 components. Although, DB_21 carries less power compared with SB_11 and SB_12 as shown in Fig. 4.8, because they are scattered twice, some component have high

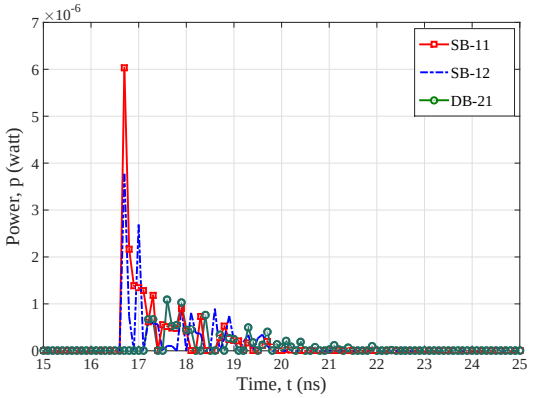

FIGURE 4.8: Overlapping of SB_11, SB_12 and DB_21.

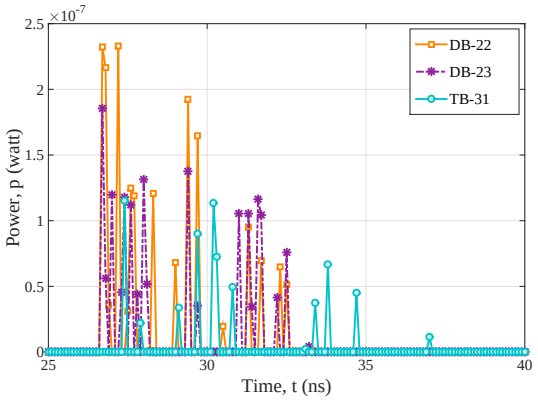

FIGURE 4.9: Overlapping of DB_22, DB_23 and TB_31.

power since they have small AoD and/or AoA with respect to the normal on the Tx or Rx planes. Accordingly, this will add a significant amount of power for total power as shown in the sum of CIR in Fig. 4.7. Also, it is observed that DB_21 components arrive even much earlier than that SB_13 as a result of shorter path length. Finally, TB_31 components arrive later than all previous ones as illustrated in Fig. 4.6. We can see that TB_31 components are overlapping with DB_22 and DB_23 components as shown in Fig. 4.9, but have less power since they are scattered triple and have less number of components and this latter can be interpreted as a result of the two practical criteria mentioned above.

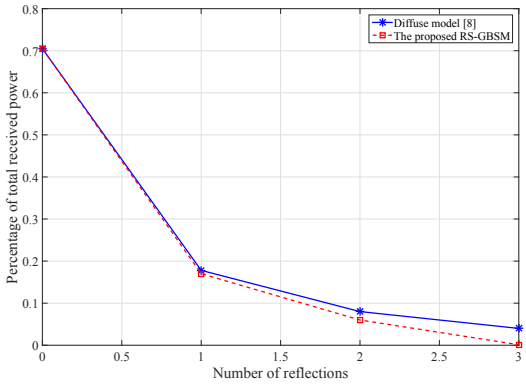

FIGURE 4.10: Percentage of received power vs. number of reflections.

4.6 Comparison of the proposed RS-GBSM with the Diffuse Model

The proposed RS-GBSM have been validated in terms of received power percentage per reflection as illustrated in Fig. 4.10. Simulation results showed a good agreement with the results of the diffuse model in [40] for up to three bounces. Here, the same transmitted power has been assumed for the purpose of validation. The slight difference is due to that the reflectivity values in IR spectrum are larger than those in visible light spectrum [120]. Furthermore, it can be seen that after the first bounce, the contribution of lower reflectivity of visible light band affects received power. This behaviour is also reported in [1] as the authors have shown that most materials have a higher reflectance in IR spectrum rather than in visible light spectrum. Highly reflective geometry encounters low path loss and hence high power will be received from different propagation paths, resulting in high delay spread and low channel bandwidth. Consequently, VLCs provide a larger transmission bandwidth compared with WIRCs.

4.7 Summary

In this chapter, a new 2D stationary multiple-bounce RS-GBSM for VLC SISO channels has been proposed. The proposed model employs a combined two-ring and confocal ellipse model. This model is sufficiently generic and adaptable to a variety of indoor scenarios since the received signal is constructed as the summation of the LoS, SB, DB, and TB rays with different powers. Based on the proposed model, geometrical properties have been derived and VLC channel characteristics have thoroughly been investigated. Simulation results have validated the utility of the proposed model compared with the existing models. Our results have demonstrated that the LoS component can carry a significant amount of power compared with the primary reflections (up to 3). However, the primary reflections tend to add to a significant amount as they sum together. VLC channel characteristics of the proposed model such as channel DC gain, RMS delay spread, and Rician factor have been investigated and analysed with respect to optical path length, AoD/AoA, and scatterers and their reflection coefficients.

Chapter 5

A 2D Mobile RS-GBSM for Vehicular VLC SISO Channels

5.1 Introduction

The annual global road crash statistics revealed that nearly 1.3 million people die in road crashes each year. Consequently, road traffic crashes account for 2.2% of all deaths globally with an average of 3,287 deaths per day [128]. It considers as the major cause of death among young people ages 15-29. Furthermore, between 20 and 50 million more people suffer non-fatal injuries, with many incurring a disability as a result of their injury [129]. In terms of material losses, road crashes cost USD 518 billion globally every year [128]. Therefore, researchers have been focusing on vehicular communication networks which enable the cars to talk to each other and to the surrounding environment in order to exchange information to enhance road safety and traffic efficiency towards accident-free driving. Over the last few years, we have witnessed many research efforts towards the adaptation of R2V, V2R, and V2V communications to the ITS. The first two scenarios of communication enable the driver to access the Internet to get directions, road maps, congestions, and accidents in real time. On the other hand, V2V communication enables cars to talk to each other in order to exchange information that may be useful in facilitating road safety

such as collision warning, lane departure, loss of stability, braking, speed, the direction of travel and location. Furthermore, nowadays, the research efforts have been directed towards what so-called Vehicle-to-Everything (V2X) technology. This includes V2V, R2V, V2R, Vehicle-to-Device (V2D),Vehicle-to-Pedestrian (V2P), Vehicle-to-Home (V2H), and Vehicle-to-Grid (V2G) communications.

Recently, Vehicular ad-hoc Network (VANET) technology provides tremendous potential to improve road safety, traffic efficiency, and ensure the safety and convenience of drivers, passengers, and pedestrians. [130]. VANET uses Dedicated Short Range Communications (DSRC)/Wireless Access in Vehicular Environments (WAVE) protocols for fast data communication. In order to implement DSRC/WAVE standards, new hardware need to be added. However, adding more hardware to the infrastructures and cars is always an issue in terms of cost and power consumption. Therefore, the idea is to take advantage of VLC technology in vehicular communications to introduce what so-called VVLCs. Table 5.1 presents a comparison between the conventional RF (DSRC) and vehicular VLCs systems.

Modern cars already have LEDs such as front headlights, tail lights, and wing mirror flashers that can be used for data transmission. They also have PDs that used for rain detection and the automatic activation of wipers as well as automatically switch-on headlamps when the luminosity level drops. Cars are being equipped with both inside and outside cameras. Inside the car, driver attention monitoring and surveillance cameras are used. Whereas outside car cameras are used for a number of applications such as road signs reading, blind spot, backup (rear view) cameras, etc. [131]. Most recently, the combination of VLC technology with a camera is termed as OCC system [131]. However, there are two main concerns about the use of OCC: firstly, light flickering due to the typical frame rate of a commercial camera, which is low (25–50 fps). Thus If the signal is transmitted at a low frequency using WLED, the human eye will detect light flickering, which is not acceptable due to eye safety regulations [1]. Therefore such cameras are only suitable for video recording. Secondly, lower data rate compared to PD-based systems which are widely used in VLCs [131].

TABLE 5.1: Comparison of VVLCs and RF (DSRC) technologies.

	VVLC	**RF (DSRC)**
Communication Scenario	Mainly (LoS)	LoS & NLoS
Distance	SSS	SSS, MSS, LSS
Cost	Low	High
New Hardware Required	No	Yes
Complexity	Low	High
Positioning Precision	High (cm-level)	Low
Interference	Optical (High) Electrical (Low)	Electrical (High)
Environment-friendly	Yes	No
Data Rate	hundreds of Mbps	27 Mbps
Carrier frequency	380–780 THz	5.85–5.925 GHz
License	Free	Required
Mobility	Low-Medium	High
Security	High	Low
SSS: Small Spatial Scale (Tx-Rx distance $<$ 300 m); MSS: Moderate spatial scale (1 km$>$Tx-Rx distance $>$ 300 m); LSS: large spatial scale (Tx-Rx distance $>$ 1 km)		

The fact that new cars are equipped with cameras will pave the way for VVLCs. For instance, the United States will require backup cameras to be installed in new cars beginning in 2018. Furthermore, the transportation lighting infrastructure such as street lamps, traffic lights, variable message boards, etc., are changing to LEDs, which results in further cost reduction since no new infrastructure expense is required. As a result, ubiquitous transmitters will be in the immediate vicinity of vehicles providing ultra-reliable and low latency due to the short transmission distances [12].

On the other hand, this new technology is not a night technology as it would seem, since it can be used in daytime, especially after the road safety legislative requirements have been made. For instance, in 2008, European commission adopted a legislation that all new cars will have to be equipped with Daytime Running Lights (DRLs) [132]. DRLs are designed to come on automatically when the engine is started [133].

The rest of this chapter is structured as follows. Section 5.2 presents the various

existing VVLC channel models. Section 5.3 describes the proposed 2D RS-GBSM for VVLC channels. Simulation results of the main VVLC channel characteristics and their analysis are unveiled in Section 5.4. Conclusions are finally drawn in Section 5.5.

5.2 VVLCs Channel Models

In order to adopt VLCs in the ITS, detailed knowledge about the underlying propagation channel is indispensable to get optimum link design and performance evaluation. A considerable amount of work has been done based on VVLCs in terms of R2V scenario, such as traffic light control at intersections [134]–[136]. However, the previous work considered only the LoS channel between the Tx and Rx. Such a channel model is deterministically derived based on a specific scenario of application. In reality, however, the received signal contains other NLoS components arriving from different paths due to multipath propagation. The latter components result from reflections off surrounding obstacles. Furthermore, a deterministic VVLC V2V and R2V channel models based on the ray-tracing method was proposed in [81], [137]. This model requires a detailed and time-consuming description of the propagation environment and consequently cannot be easily generalised to a wider class of scenarios. The authors in [138], [139] have used geometry-based road-surface reflection model, which considers LoS and NLoS components. The latter model ignored all other reflections except that reflected off the road-surface, i.e., asphalt.

Another purpose of this thesis is to fill the above research gaps within vehicular VLCs landscape. Therefore, in this work, we propose a new RS-GBSM that addresses all the aforementioned shortcomings of the existing VVLC channel models. The proposed model has already considered the light that reflected off moving vehicles around the Tx and Rx and the stationary roadside environments. Due to their reasonable complexity and mathematical traceability, RS-GBSM approach has widely been used in conventional RF based vehicular cellular systems to mimic V2V channels such as [110]–[112]. However, channel knowledge obtained from conventional V2V based cellular radio systems cannot be directly used for V2V based VLC systems. Therefore, characterising

of VVLC channels is one of the most important challenges that have to be addressed before VVLC technology deployment. RS-GBSM approach has been employed to model indoor VLC channels. The authors in [95] used the one-ring model for investigating indoor VLC channel characteristics. While in [80], a combined tow-ring and confocal ellipse model was proposed to model indoor VLC channels considering up to three reflections. Most importantly, it is worth to note that the shortage of measurement-based channel models of VVLC, particularly for V2V scenarios, hinders the progress of IEEE 802.15.7 standardization since it does not discuss any channel parameter details that describe the reference channel model. Motivated by the above research gaps, in this paper we propose a new mobile RS-GBSM that addresses all the aforementioned shortcomings of the existing VVLC channel models.

5.3 A Mobile RS-GBSM for VVLC Channels

For Vehicular VLC Channels, there are three major elements should be modeled: the road traffic, the environment adjacent to the road, and the wave propagation between the vehicles. In terms of first and second elements, this paper considers a SSS VVLC system model deployed in a typical urban canyon as illustrated in Fig. 5.1. Here, the road environment includes dynamic road traffic such as moving cars, vans, and trucks, as well as includes roadside environment, e.g., buildings, parked cars, road signs, and trees. In terms of wave propagation between the Tx and the target vehicles, there are further two key elements should be modeled, namely, the Tx pattern and the Rx aperture size. In VVLCs, the Tx is usually an automotive LED headlamp. Unfortunately, since VVLC technology is still in very early stages of research, a standard headlamp with measured beam pattern model does not exist yet. Furthermore, the existing Halogen and gas discharge (Xenon) lamps are not suitable for intensity modulation purposes. Therefore, an ideal Lambertian model is employed in this work. The intensity angular distribution of generalised Lambertian pattern can be expressed as (3.3). In this work, the optical receiver is assumed to be a non-imaging PIN PD, which is equipped at the rear end of the vehicle. Preferring the PD is due to the fact that the OCC experiences light flickering and provides low data rate compared

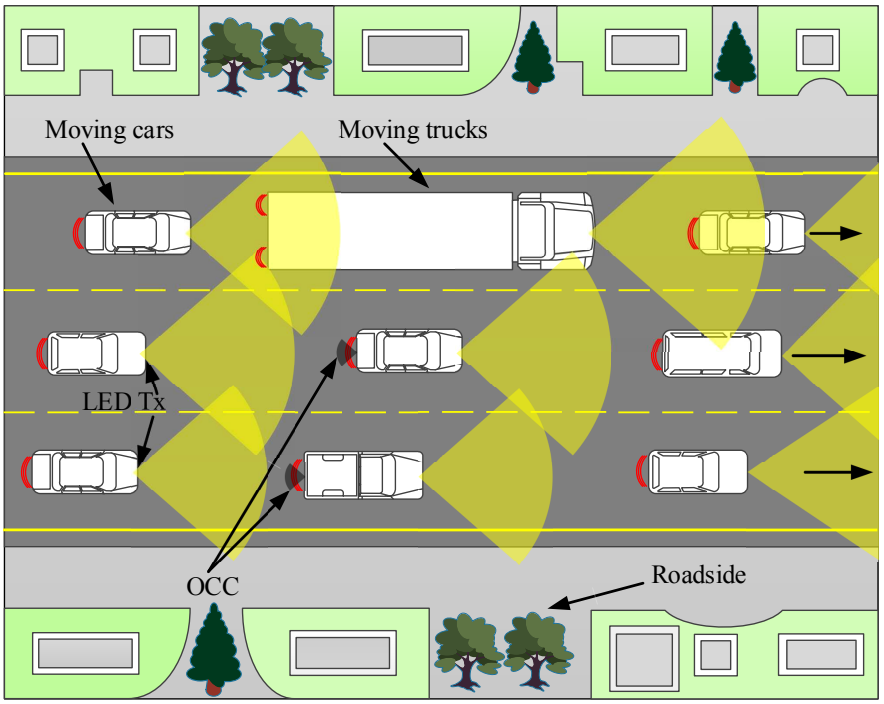

FIGURE 5.1: A typical VVLC environment.

to PD-based systems widely used in VLCs [131]. The PD can be modelled using its effective collection area as given in (3.5).

In terms of the optical wireless channel, Fig. 5.2 illustrates the geometry of the proposed RS-GBSM for VVLC channels. The geometry of the proposed model is a combination of a two-ring model and a confocal ellipse model considering SB and DB two-ring model, SB ellipse model, in addition to the LoS component. The probable optical paths and the definitions of key geometry parameters are presented in Table 5.2 and Table 5.3, respectively. It worth mentioning that this model considers as a special case of the combined two-ring and confocal ellipse model, which is proposed in Chapter 4. Here, only SB and DB in addition to the LoS components have been considered.

The two-ring scenario is proposed to model the scatterers around the Tx and Rx, while the ellipse scenario is proposed to model the stationary roadside environments. Suppose there are N_1 local scatterers around the Tx lying on a ring of radius R_{T} and the n_1th $(n_1 = 1, ..., N_1)$ local scatterer is denoted by S^{n_1}. Similarly, assume

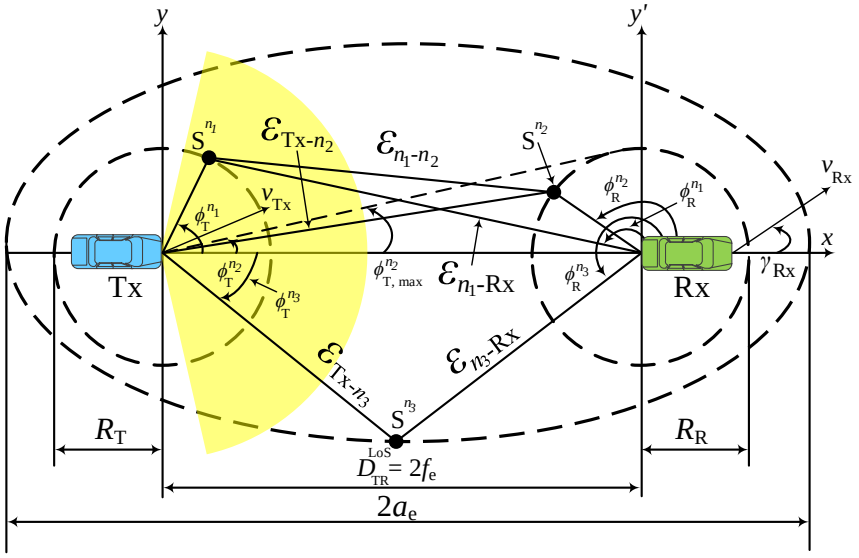

FIGURE 5.2: A generic 2D RS-GBSM for vehicular VLC channels.

TABLE 5.2: Probable optical paths.

Component	**Optical Path**	**Distance**
LoS	Tx→Rx	D
1- SB − 11	1- Tx→S^{n_1}→ Rx	1- R_T +$\varepsilon_{S^{n_1}-Rx}$
2- SB − 12	2- Tx→S^{n_2}→ Rx	2- $\varepsilon_{Tx-S^{n_2}}$+R_R
3- SB − 13	3- Tx→S^{n_3}→ Rx	3- $\varepsilon_{Tx-S^{n_3}}$+ $\varepsilon_{S^{n_3}-Rx}$
DB − 11	Tx→S^{n_1}→S^{n_2}→ Rx	R_T+$\varepsilon_{S^{n_1}-S^{n_2}}$+$R_R$

there are N_2 local scatterers around the Rx lying on a ring of radius R_R and the n_2th ($n_2 = 1, ..., N_2$) local scatterer is denoted by S^{n_2}. For the ellipse model, N_3 local scatterers lying on an ellipse and the n_3th ($n_3 = 1, ..., N_3$) local scatterer is denoted by S^{n_3}. Ellipses parameters are already explained in chapter 4. The Tx and Rx are moving with speeds v_{Tx} and v_{Rx} in directions determined by the angles of motion γ_{Tx} and γ_{Rx}, respectively. At the Tx, the AoDs are denoted by $\phi_T^{n_1}$, $\phi_T^{n_2}$, and $\phi_T^{n_3}$. While at the effective scatterers side S^{n_1}, S^{n_2}, and S^{n_3} the corresponding AoAs and AoDs are denoted by $\theta_S^{n_1}$, $\theta_S^{n_2}$, $\theta_S^{n_3}$, and $\phi_S^{n_1}$, $\phi_S^{n_2}$, $\phi_S^{n_3}$, respectively. On the other hand, the corresponding AoAs of the waves that impinge on the Rx, are designated by $\phi_R^{n_1}$, $\phi_R^{n_2}$, and $\phi_R^{n_3}$. In the literature, many different distributions have been proposed to characterize AoD $\phi_T^{n_i}$ and AoA $\phi_R^{n_i}$, such as Gaussian and the von

TABLE 5.3: Definitions of key geometry parameters.

$D_{\mathrm{TR}}^{\mathrm{LoS}}$	distance between the centre of the Tx-ring and the centre of the Rx-ring
T_{R}, R_{R}	radius of the Tx-ring and Rx-ring, respectively
a, b	semi-major axis and semi-minor axis of the ellipse, , respectively
$\phi_{\mathrm{T}}^{(n_i)}$ $(i=1,2,3)$	angle of departure (AoD) of the waves that emitted from the optical source
$\phi_{\mathrm{R}}^{(n_i)}$ $(i=1,2,3)$	angle of arrival (AoA) of the waves that impinge the optical receiver
$\theta_{\mathrm{S}}^{(n_i)}$ $(i=1,2,3)$	angle of arrival (AoA) of the waves that impinge the effective scatterers
$\phi_{\mathrm{S}}^{(n_i)}$ $(i=1,2,3)$	angle of departure (AoD) of the waves that reflecting off walls the effective scatterers
γ_{Tx}, γ_{Rx}	moving directions of the Tx and Rx in the x-y plane, respectively
υ_{Tx}, υ_{Rx}	velocities of the Tx and Rx, respectively
$\varepsilon_{\mathrm{Tx}-n_i}$	distances from the Tx to scatterers $n_i, (i=1,2,3)$
$\varepsilon_{n_i-\mathrm{Rx}}$	distances from scatterers n_i to the Rx, $(i=1,2,3)$
$\varepsilon_{n_1-n_2}$	distances from scatterer n_1 to scatterer n_2

Mises distributions [110]. In this study, an isotropic scattering around the rings and ellipse is characterized by a uniform distribution of the AoDs $\phi_{\mathrm{T}}^{n_i}$ and AoAs $\phi_{\mathrm{R}}^{n_i}$.

Based on the proposed channel model, the CIR can be expressed as a superposition of the LoS and NLoS components, as

$$h(t) = h^{\mathrm{LoS}}(t) + h^{\mathrm{NLoS}}(t). \tag{5.1}$$

As mentioned in chapter 4, the complexity of calculating the CIR grows exponentially with the number of reflections k, therefore, this work considers the CIR for only primary reflections, i.e., SB and DB as well as the LoS component. Consequently, (5.1) can be rewritten in more detail as

$$h(t) = h^{\mathrm{LoS}}(t) + \sum_{i_{\mathrm{SB}}=1}^{I_{\mathrm{SB}}} h^{\mathrm{SB}_i}(t) + h^{\mathrm{DB}}(t). \tag{5.2}$$

Here, $I_{\mathrm{SB}} = 3$ which means there are three subcomponents for SB rays, i.e., SB_11 from the Tx-ring, SB_12 from the Rx ring, and SB_13 from the confocal ellipse. For the sake of a more practical VVLC channel model, the following two criteria have been assumed. Firstly, we introduced the visibility function $V(\phi_{\mathrm{R}})$ at the Rx side, which indicates that only the scatterers that located within PDs FoV will be considered.

Visibility function $V(\phi_{\mathrm{R}})$ can be expressed as a function of PDs FoV Ψ_{FoV} as

$$V(\phi_{\mathrm{R}}) = \begin{cases} 1 & \text{if } \ 0 \leq \text{AoA } \phi_{\mathrm{R}} \leq \Psi_{\mathrm{FoV}} \\ 0 & \text{if } \ \text{AoA } \phi_{\mathrm{R}} > \Psi_{\mathrm{FoV}}. \end{cases} \tag{5.3}$$

Secondly, the $i-$th ray, in the double-bounce model, is always reflected off from a far scatterer to a near scatterer, relative to the optical receiver. Therefore, some i-bounced components are not necessarily to be considered making the proposed model more realistic and practical. The LoS, SB and DB channels within the proposed model will be more detailed in next subsections.

5.3.1 The LoS Link

In the proposed model, if the Tx and Rx are stationary, the LoS component of the CIR is deterministic and given as a function of signal propagation delay between the Tx and Rx as [35]

$$\begin{aligned} h^{\mathrm{LoS}}(t) =& \frac{(m+1)A_{\mathrm{r}}\ V(\phi_{\mathrm{R}})}{2\pi (D_{\mathrm{TR}}^{\mathrm{LoS}})^2}\ \cos^m(\phi_{\mathrm{T}}^{\mathrm{LoS}}) \\ & \times \cos(\phi_{\mathrm{R}}^{\mathrm{LoS}})\ \delta(t - \frac{D_{\mathrm{TR}}^{\mathrm{LoS}}}{c}). \end{aligned} \tag{5.4}$$

However, if the Tx and Rx are moving, (5.4) can be rewritten as

$$\begin{aligned} h^{\mathrm{LoS}}(t) =& \frac{(m+1)A_{\mathrm{r}}\ V(\phi_{\mathrm{R}})}{\pi (D(t)_{\mathrm{TR}})^2}\ \cos^m(\phi_{\mathrm{T}}^{\mathrm{LoS}}) \\ & \times \cos(\phi_{\mathrm{R}}^{\mathrm{LoS}})\ \delta(t - \frac{D(t)_{\mathrm{TR}}}{c}) \end{aligned} \tag{5.5}$$

where

$$D(t)_{\mathrm{TR}}(t) = \varepsilon(t)_{\mathrm{TR}} - [\varepsilon(t)_{\mathrm{Tx}} - \varepsilon(t)_{\mathrm{Rx}}], \quad \upsilon_{\mathrm{Tx}} > \upsilon_{\mathrm{Rx}}. \tag{5.6}$$

Here, $D(t)_{\mathrm{TR}}(t)$ determines the time-varying distance between the Tx and the target Rx. While, $\varepsilon(t)_{\mathrm{TR}}$, $\varepsilon(t)_{\mathrm{Tx}}$, and $\varepsilon(t)_{\mathrm{Rx}}$ are the initial Tx-Rx distance, Tx distance, and Rx distance, respectively. If the Tx and Rx are moving with speeds υ_{Tx} and υ_{Rx} in directions determined by the angles of motion γ_{Tx} and γ_{Rx}, then the distances $\varepsilon(t)_{\mathrm{Tx}}$

and $\varepsilon(t)_{\mathrm{Rx}}$, can be given as $\varepsilon(t)_{\mathrm{Tx}} = \upsilon_{\mathrm{Tx}} \times t \times \cos(\gamma_{\mathrm{Tx}})$ and $\varepsilon(t)_{\mathrm{Rx}} = \upsilon_{\mathrm{Rx}} \times t \times \cos(\gamma_{\mathrm{Rx}})$, respectively.

5.3.2 Single-Bounce Link

5.3.2.1 SB Components in Two-Ring Model

The first probable optical path within the two-ring model is SB_11. The AoD of the nth transmitted wave is denoted by $\phi_{\mathrm{T}}^{n_1}$, and the corresponding AoA is described by $\phi_{\mathrm{R}}^{n_1}$ $(n_1 = 1, 2, ..., N_1)$. The first SB component of the CIR for link SB_11 can be written as

$$\begin{aligned} h^{11}(t) = \sum_{n_1=1}^{N_1} & \frac{(m+1)\ V(\phi_{\mathrm{R}})}{2\pi(R_{\mathrm{T}})^2} \cos^m(\phi_{\mathrm{T}}^{n_1})\ \cos(\theta_{\mathrm{S}}^{n_1}) \\ & \times \frac{(m+1)\ A_{\mathrm{r}}\ \rho_{\mathrm{Vehicles}}}{2\pi(\varepsilon_{n_1-\mathrm{Rx}})^2} \cos^m(\phi_{\mathrm{S}}^{n_1})\ \cos(\phi_{\mathrm{R}}^{n_1}) \\ & \times \delta(t - \frac{\varepsilon_{n_1-\mathrm{Rx}} + \mathrm{R_T}}{c}). \end{aligned} \tag{5.7}$$

Similarly, the second SB component of the CIR for link SB_12 can be written as

$$\begin{aligned} h^{12}(t) = \sum_{n_2=1}^{N_2} & \frac{(m+1)\ V(\phi_{\mathrm{R}})}{2\pi(\varepsilon_{\mathrm{Tx}-n_2})^2} \cos^m(\phi_{\mathrm{T}}^{n_2})\ \cos(\theta_{\mathrm{S}}^{n_2}) \\ & \times \frac{(m+1)\ A_{\mathrm{r}}\ \rho_{\mathrm{Vehicles}}}{2\pi(R_{\mathrm{R}})^2} \cos^m(\phi_{\mathrm{S}}^{n_2})\ \cos(\phi_{\mathrm{R}}^{n_2}) \\ & \times \delta(t - \frac{\varepsilon_{\mathrm{Tx}-n_2} + R_{\mathrm{R}}}{c}). \end{aligned} \tag{5.8}$$

Here, ρ_{Vehicles} denotes the reflection coefficient of the vehicles body. The angle $\phi_{\mathrm{T,max}}^{n_2}$ in Fig. 5.2 designates the maximum AoD $\phi_{\mathrm{T}}^{n_2}$ that can be seen by the Rx. This quantity is related to R_{R} and D by $\phi_{\mathrm{T,max}}^{n_2} = \arctan(R_{\mathrm{R}}/D_{\mathrm{TR}}^{\mathrm{LoS}})$. From Fig. 5.2 and based on the application of the law of cosines in appropriate triangles, we get

$$\varepsilon_{n_1-\mathrm{Rx}} = \sqrt{(R_{\mathrm{T}})^2 + (D_{\mathrm{TR}}^{\mathrm{LoS}})^2 - 2R_{\mathrm{T}}D_{\mathrm{TR}}^{\mathrm{LoS}}\ \cos(\phi_{\mathrm{T}})} \tag{5.9}$$

and

$$\varepsilon_{\mathrm{Tx}-n_2} = \sqrt{(R_{\mathrm{R}})^2 + (D_{\mathrm{TR}}^{\mathrm{LoS}})^2 - 2R_{\mathrm{T}}D_{\mathrm{TR}}^{\mathrm{LoS}}\ \cos(\theta_{\mathrm{R}})}. \tag{5.10}$$

Note that the AoD and AoA are correlated for SB rays in the proposed model. Therefore, using the law of sines in appropriate triangles, we get

$$\phi_{\mathrm{R}} = \arcsin[\frac{R_{\mathrm{T}}\ \sin(\phi_{\mathrm{T}})}{\varepsilon_{n_1-\mathrm{Rx}}}] \tag{5.11}$$

and

$$\phi_{\mathrm{T}} = \arcsin[\frac{R_{\mathrm{R}}\ \sin(\phi_{\mathrm{R}})}{\varepsilon_{\mathrm{Tx}-n_2}}]. \tag{5.12}$$

Equations (5.11) and (5.12) are valid for links SB-11 and SB-12, respectively. Hence, (5.9) can be rewritten as

$$\varepsilon_{n_1-\mathrm{Rx}} = \sqrt{(R_{\mathrm{T}})^2 + (D_{\mathrm{TR}}^{\mathrm{LoS}})^2 - 2R_{\mathrm{T}}D_{\mathrm{TR}}^{\mathrm{LoS}}\sqrt{1-(\frac{R_{\mathrm{T}}\sin(\phi_{\mathrm{R}})}{\varepsilon_{\mathrm{Tx}-n_1}})^2}}. \tag{5.13}$$

5.3.2.2 SB Components in Ellipse Model

According to the proposed model, there is one more probable optical path through the ellipse model, i.e., link SB − 13. The SB component of the CIR for link SB − 13 can be written as

$$\begin{aligned} h^{13}(t) = \sum_{n_3=1}^{N_3} & \frac{(m+1)\ V(\phi_{\mathrm{R}})}{2\pi(\varepsilon_{\mathrm{Tx}-n_3})^2}\cos^m(\phi_{\mathrm{T}}^{n_3})\ \cos(\theta_{\mathrm{S}}^{n_3}) \\ & \times \frac{(m+1)\ A_{\mathrm{R}}\ \rho_{\mathrm{Roadside}}}{2\pi(\varepsilon_{n_3-\mathrm{Rx}})^2}\cos^m(\phi_{\mathrm{S}}^{n_3})\ \cos(\phi_{\mathrm{R}}^{n_3}) \\ & \times \delta(t - \frac{\varepsilon_{\mathrm{Tx}-n_3} + \varepsilon_{n_3-\mathrm{Rx}}}{c}). \end{aligned} \tag{5.14}$$

Here, ρ_{Roadside} denotes the reflection coefficient of the roadside substances.

The optical path lengths within the ellipse model can be derived based on pure ellipse properties mentioned in Chapter 4. The total optical path through the confocal ellipse model is

$$\varepsilon_{\mathrm{Tx}-n_3} + \varepsilon_{n_3-\mathrm{Rx}} = 2a_{\mathrm{e}}. \tag{5.15}$$

According to the law of cosines in triangle $\mathrm{Tx} - n_3 - \mathrm{Rx}$, the optical path length between the focal point Tx and a specific scatterer is given as

$$\varepsilon_{\mathrm{Tx}-n_3} = \sqrt{(\varepsilon_{n_3-\mathrm{Rx}})^2 + (2f_\mathrm{e})^2 - 2(\varepsilon_{n_3-\mathrm{Rx}})(2f_\mathrm{e})\cos(\phi_\mathrm{R}^{n_3})}. \tag{5.16}$$

Based on ellipse properties and after some manipulation, we can get the path length as a function of AoA ϕ_R^{n3}

$$\varepsilon_{\mathrm{Tx}-n_3} = \frac{a_\mathrm{e}^2 + f_\mathrm{e}^2 + 2a_\mathrm{e}f_\mathrm{e}\cos(\phi_\mathrm{R}^{n_3})}{a_\mathrm{e} + f_\mathrm{e}\cos(\phi_\mathrm{R}^{n_3})}. \tag{5.17}$$

Substituting (5.17) to (5.15), we get

$$\varepsilon_{n_3-\mathrm{Rx}} = \frac{b_\mathrm{e}^2}{a_\mathrm{e} + f_\mathrm{e}\cos(\phi_\mathrm{R}^{n_3})}. \tag{5.18}$$

Applying the law of sines to the triangle $\mathrm{Tx} - n_3 - \mathrm{Rx}$ in order to find the relationship between the AoA ϕ_R^{n3} and AoD ϕ_R^{n3} for ellipse scattering region, we get

$$\phi_\mathrm{T}^{n_3} = \arcsin[\frac{b_\mathrm{e}^2\sin(\phi_\mathrm{R}^{n_3})}{a_\mathrm{e}^2 + f_\mathrm{e}^2 + 2a_\mathrm{e}f_\mathrm{e}\cos(\phi_\mathrm{R}^{n_3})}] \tag{5.19}$$

and

$$\phi_\mathrm{T}^{n_3} = \arccos[\frac{2a_\mathrm{e}f_\mathrm{e} + (a_\mathrm{e}^2 + f_\mathrm{e}^2)\cos(\phi_\mathrm{R}^{n_3})}{a_\mathrm{e}^2 + f_\mathrm{e}^2 + 2a_\mathrm{e}f_\mathrm{e}\cos(\phi_\mathrm{R}^{n_3})}]. \tag{5.20}$$

For single-bounce in the two-ring model and the ellipse model, due to the microscopic irregularities of the scatterers surfaces, the reflection pattern is assumed to be diffuse and hence the reflected components can correctly be approximated using the Lambertian reflection pattern. This model states that the total radiant power observed from a Lambertian surface is directly proportional to the cosine of the angle between the observer's line-of-sight and the surface normal. Since there is no unique reference surface normal that we can refer to, we assumed that the surface normal angles are uniformly distributed over $[\phi_\mathrm{T}^{n_i}, \phi_\mathrm{R}^{n_i}]$. Hence, the scattering angles can be characterized as the following criterion

$$\phi_{\mathrm{T}}^{n_i} > \theta_{\mathrm{S}}^{n_i}, \phi_{\mathrm{S}}^{n_i} > \phi_{\mathrm{R}}^{n_i},\ i = 1, 2, 3. \tag{5.21}$$

Accordingly, the angles pairs $\theta_{\mathrm{S}}^{n_1}$, $\phi_{\mathrm{S}}^{n_1}$, $\theta_{\mathrm{S}}^{n_2}$, $\phi_{\mathrm{S}}^{n_2}$, $\theta_{\mathrm{S}}^{n_3}$, and $\phi_{\mathrm{S}}^{n_3}$ can be obtained by using trigonometry in triangles $\mathrm{Tx} - \mathrm{S}^{n_1} - \mathrm{Rx}$, $\mathrm{Tx} - \mathrm{S}^{n_2} - \mathrm{Rx}$, and $\mathrm{Tx} - \mathrm{S}^{n_3} - \mathrm{Rx}$, respectively. For instance, according to trigonometry in Tx-ring model, if $\phi_{\mathrm{T}}^{n_1}$ and $\phi_{\mathrm{R}}^{n_1}$ have been determined as detailed previously, the apex angle in triangle $\mathrm{Tx} - \mathrm{S}^{n_1} - \mathrm{Rx}$ can be determined accordingly. Hence, if $\theta_{\mathrm{S}}^{n_1}$ is assumed as uniformly distributed, $\phi_{\mathrm{S}}^{n_1}$ represents the residual the of the apex angle. The same procedure is applied to determine $\theta_{\mathrm{S}}^{n_2}$, $\phi_{\mathrm{S}}^{n_2}$, $\theta_{\mathrm{S}}^{n_3}$, and $\phi_{\mathrm{S}}^{n_3}$. It is worth to notice that unlike in LoS scenario, in SB scenario, the shortest optical paths are not necessarily carry more power than other paths as will be noticed in Section 5.4. This is due to the effect of AoA and AoD at the scatterers.

5.3.3 Double-Bounce link

In the DB scenario, the received power mainly comes from the DB rays which are reflected twice, firstly at Tx-ring and then at the Rx-ring. The DB components within combined two-ring and confocal ellipse model, i.e., the optical paths Tx-n_1-n_3-Rx and Tx-n_3-n_2-Rx are ignored since they reflect less power compared to the two-ring model as reported in [80]. This is due to the longer path length and lower reflectivity ρ_{Roadside} of the roadside scatterers. The DB component of the CIR in the two-ring model can be expressed as

$$\begin{aligned} h^{21}(t) = \sum_{n_1,n_2=1}^{N_1,N_2} & \frac{(m+1)\ V(\phi_{\mathrm{R}})\ \cos^m(\phi_{\mathrm{T}}^{n_1})\ \cos(\theta_{\mathrm{S}}^{n_1})}{2\pi(R_{\mathrm{T}})^2} \\ & \times \frac{(m+1)\ \cos^m(\phi_{\mathrm{S}}^{n_1})\ \cos(\theta_{\mathrm{S}}^{n_2})\ \rho_{\mathrm{Vehicles}}}{2\pi(\varepsilon_{n_1-\mathrm{S}^{n_2}})^2} \\ & \times \frac{(m+1)\ \cos^m(\phi_{\mathrm{S}}^{n_2})\ \cos(\phi_{\mathrm{R}}^{n_2})\ A_{\mathrm{R}}\ \rho_{\mathrm{Vehicles}}}{2\pi(R_{\mathrm{R}})^2} \times \delta(t - \frac{D_{\mathrm{DB}}}{c}). \end{aligned} \tag{5.22}$$

From the quadrilateral Tx-n_1-n_2-Rx, the distances D_{DB} and $\varepsilon_{n_1-n_2}$ can be expressed as

$$D_{\mathrm{DB}} = R_{\mathrm{T}} + \varepsilon_{n_1-n_2} + R_{\mathrm{R}} \tag{5.23}$$

and

$$\begin{aligned}(\varepsilon_{n_1-n_2})^2 =&(\varepsilon_{n_1-\mathrm{Rx}})^2 + (R_{\mathrm{R}})^2 \\ &- 2(\varepsilon_{n_1-\mathrm{Rx}})R_{\mathrm{R}}\cos(\theta_{\mathrm{R}}^{n_1} - \theta_{\mathrm{R}}^{n_2}).\end{aligned} \tag{5.24}$$

In the DB model, the AoA $\theta_{\mathrm{S}}^{n_i}$ and the AoD $\phi_{\mathrm{S}}^{n_i}$ $(i = 1, 2)$ at an effective scatterer, have been determined by using the distances $\varepsilon_{n_1-\mathrm{Rx}}$ and $\varepsilon_{\mathrm{Tx}-n_2}$, in (5.9) and (5.10), respectively. For example, to compute $\theta_{\mathrm{S}}^{n_1}$ and $\phi_{\mathrm{S}}^{n_1}$ angles in Tx-ring, we use the law of cosines to determine the apex angle in triangle $\mathrm{Tx} - \mathrm{S}^{n_1} - \mathrm{S}^{n_2}$ with help of (5.10). Hence, if $\theta_{\mathrm{S}}^{n_1}$ is assumed as uniformly distributed, $\phi_{\mathrm{S}}^{n_1}$ represents the residual the of the apex angle. The same procedure is applied to determine $\theta_{\mathrm{S}}^{n_2}$ and $\phi_{\mathrm{S}}^{n_2}$ in Rx-ring by using law of cosines in triangle $\mathrm{S}^{n_1} - \mathrm{S}^{n_2} - \mathrm{Rx}$ with help of (5.9).

5.4 Results and Analysis

In performing simulations, the entries of the environmental parameters are summarized in Table 5.4. The body of the vast majority of vehicles is made from steel. Therefore, average painted steel reflectance ρ_{Vehicles} will be considered. Likewise, for roadside environment, average concrete reflectance ρ_{Roadside} has been selected. According to [52], the reasonable value of N parameter is in the range from 40 to 50. The most important VVLC channel characteristics have been studied in below subsections.

5.4.1 Received Optical Power

According to the proposed model, the total received optical power can be generally expressed as

$$P_{\mathrm{r}} = P_{\mathrm{t}}\,[H(0)^{\mathrm{LoS}} + H(0)^{\mathrm{SB}} + H(0)^{\mathrm{DB}}]. \tag{5.25}$$

TABLE 5.4: Model Parameters used in computer simulations.

Model Parameters	
The initial Tx-Rx distance	70 m
Semi-major a & semi-minor b axes	36.5 m, 10 m
Ring radius $(R_{\mathrm{T}}, R_{\mathrm{R}})$	3 m
Tx speed v_{Tx}	21.6 km/h
Rx speed v_{Rx}	14.4 km/h
Lane width	3.5 m [140]
Roadside width	2.2 m [141]
Vehicles reflectivity $(\rho_{\mathrm{Vehicles}})$	0.8 [142]
Roadside reflectivity $(\rho_{\mathrm{Roadside}})$	0.4 [143]
I	7000 cd [144]
Mode number (m)	1
PD area	1 cm^2 [20]
PD's (FoV)	80° [20]
Number of scatterers	40 [52]

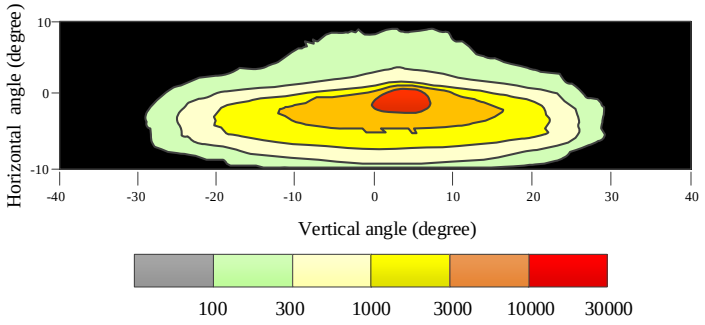

FIGURE 5.3: Isocandela diagram of the median luminous intensities for a pair of low-beam tungsten-halogen headlamps [144].

In terms of transmitted power P_{t}, since a standard LEDs headlamp with measured beam pattern model is not available, we considered the luminous intensity I (cd) at 50% (median) of the low-beam tungsten-halogen headlamp in [144]. The isocandela diagram of a pair of low-beam tungsten-halogen headlamps is plotted in Fig. 5.3 [144]. Also, we consider the luminous efficacy of radiation (LER) of a high power phosphor-coated WLED to be 250.3 lm/W [138]. Thus the received optical power can be expressed as

$$P_{\mathrm{Rx}} = \frac{I}{LER}\,[H(0)^{\mathrm{LoS}} + H(0)^{\mathrm{SB}} + H(0)^{\mathrm{DB}}]. \tag{5.26}$$

Let's assume that both of the Tx and Rx are moving in the same direction, i.e.,

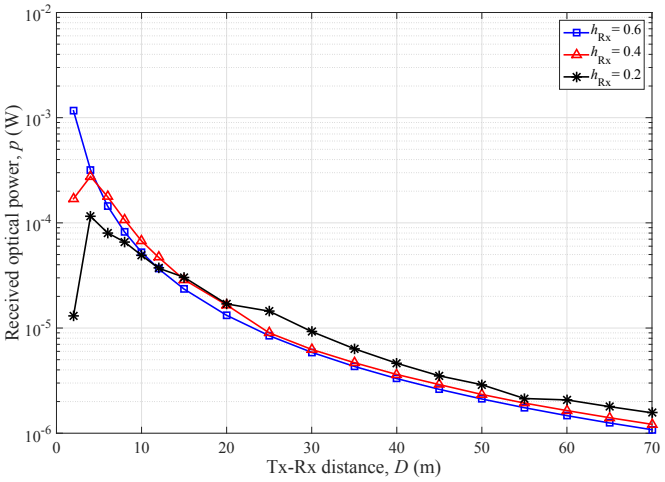

FIGURE 5.4: Received optical power, h_{Rx}= 0.2 m, 0.4 m, and 0.6 m.

$\gamma_{\text{Tx}} = \gamma_{\text{Rx}} = 0$, but in different speeds, specifically, $v_{\text{Tx}} = 6$ m/s and $v_{\text{Rx}} = 4$ m/s which are correspond to 21.6 km/h and 14.4 km/h, respectively. Note that, the speeds are chosen to be within urban speed limits. In terms of LoS component, the received optical power for different distances between the Tx and Rx is presented in Fig. 5.4. Here we considered three different cases in which the PD is mounted at different heights h_{Rx}, i.e., 0.6 m, 0.4 m and 0.2 m. The Tx is mounted at a 0.6 m height, which is considered as the reference height. Note that in the first case the Tx and the Rx are on the same plane, while there are 0.2 m and 0.4 m differences in the second and third cases, respectively. Referring to Fig. 5.4, we can highlight the following. The results show in general the received power decrease as the distance increase, which is intuitively behaviour. But in terms of PD position effect, it can be noticed that the received power is higher as Tx-Rx height difference increases. This is valid for Tx-Rx distances longer than 20 m. However, before this, since the Tx-Rx distances become shorter and shorter, the effects of both PD height and the observation angle with respect to the PD surface normal are the direct result of changes in the received power. We can also clearly observe that the received power displays peaks at very short distance, specifically at 2 m, when there is Tx-Rx height difference. This can be explained with the help of Fig. 5.3, where lower luminous intensities (cd) is obtained due to the effect of the higher vertical angles.

For validation purpose, the simulation results based on Lambertian pattern showed

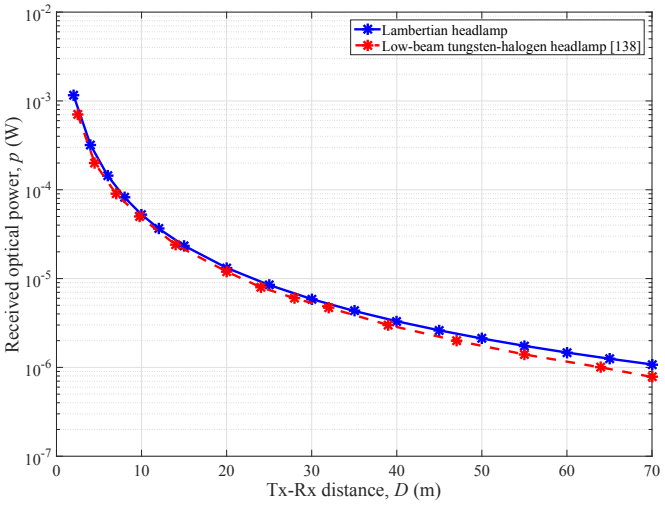

FIGURE 5.5: Received optical power considering Lambertian headlamp and low-beam tungsten-halogen headlamp h_{Rx}= 0.6 m.

good agreement with those obtained by measurements based on using a low-beam tungsten-halogen headlamp in [138], as illustrated in Fig. 5.5. Here we assumed that both the Tx and Rx are mounted at a 0.6 m height.

On the other hand, in terms of SB components, the received power from $\mathrm{SB}-11$ and $\mathrm{SB}-12$ components for the two-ring model are shown in Fig. 5.6. Here, we deliberately use the time-domain to indicate SB components of the CIR for the proposed channel model. It can be noticed, firstly, that $\mathrm{SB}-11$ components carry much power than $\mathrm{SB}-12$ components. This is due to the PD's FoV constraint, which states that all the scatterers are within PD's FoV. Secondly $\mathrm{SB}-12$ components have a longer tail compared with $\mathrm{SB}-11$ because of the wider aperture of the optical source at the Tx side. The last SB component results from the surrounding roadside environments which are represented here by the ellipse model. The received power of $\mathrm{SB}-13$ component is illustrated in Fig. 5.7, alongside $\mathrm{SB}-11$ and $\mathrm{SB}-12$ components. It can be shown that the received power from $\mathrm{SB}-13$ is significantly lower as compared to $\mathrm{SB}-11$ and $\mathrm{SB}-12$. This is due to two main factors: first, in the ellipse model the optical rays travel longer distance than their equivalents in the two-ring model and hence higher path loss. This also explains why $\mathrm{SB}-13$ comes later than the other first two components. Second, since we assumed that ρ_{Roadside} represents the average of concrete reflectance, a high portion of the incident power will be absorbed due to

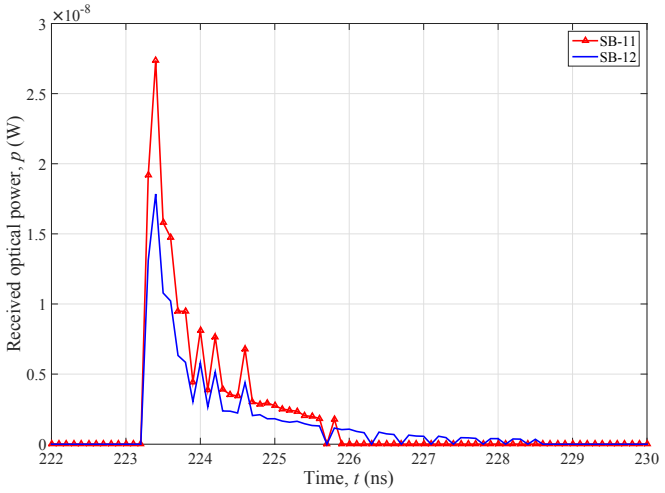

FIGURE 5.6: Received power from $SB-11$ and $SB-12$ components within the two-ring model ($t = 0$, $D = 70$ m).

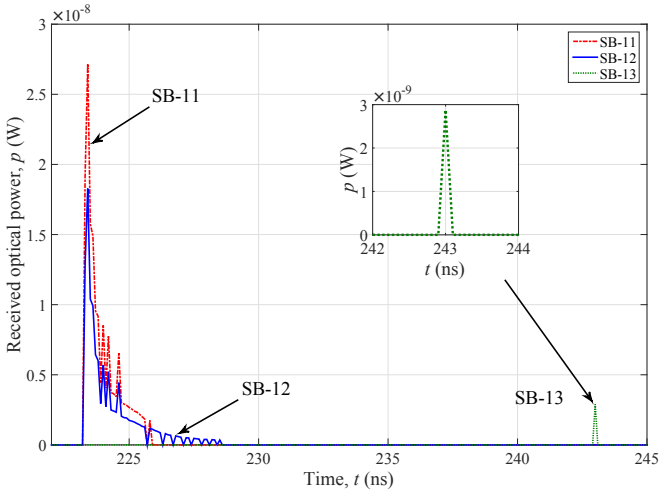

FIGURE 5.7: Received power from $SB-11$, $SB-12$, and $SB-13$ components within the combined two-ring and confocal ellipse model ($t = 0$, $D = 70$ m).

the low concrete reflectivity. Consequently, the total power carried by SB component within the combined two-ring and confocal ellipse model is illustrated in Fig. 5.8. It is the sum of the power curried by $SB-11$ and $SB-12$, and $SB-13$.

In terms of the DB component of the CIR, the received power is presented in Fig. 5.9. Here, the results have been obtained at the initial distance only, i.e., $t = 0$ and $D = 70$ m. Compared with SB components, it can be seen that the DB component carry a significantly smaller amount of power. It is worthwhile to mention that there are another probable optical paths for DB component within the proposed model as

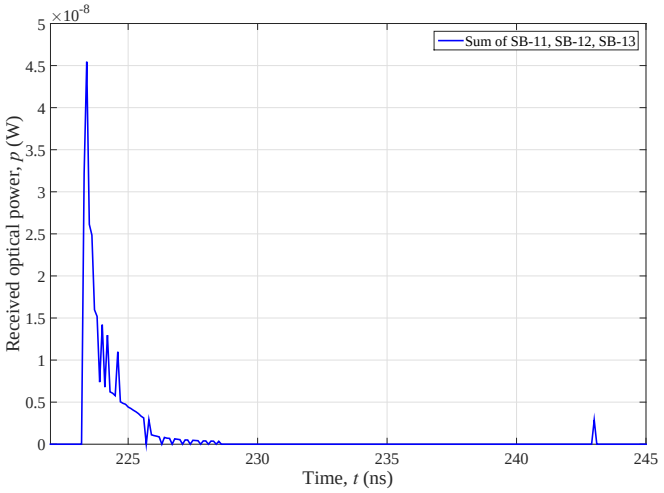

FIGURE 5.8: Total received power from the combined two-ring and confocal ellipse models ($t = 0$, $D = 70$ m).

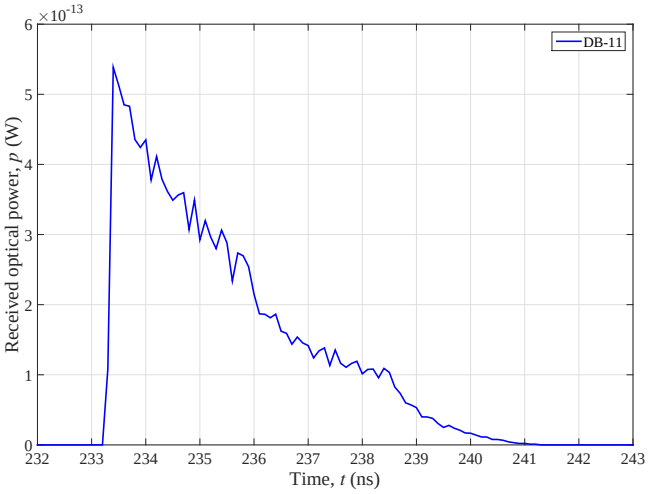

FIGURE 5.9: Received power from DB_11 component within the two-ring model ($t = 0$, $D = 70$ m).

detailed in [80] for indoor VLCs. For instance, one probable path can be scattered by the scatterers of Tx-ring model then reflected off by the scatterers of the ellipse model. In this study, such paths are not considered because they will be highly attenuated and have insignificant contribution to the total power that arrives at the PD. Although DB_11 component carries insufficient power, it comes earlier than SB_13 as it is clearly shown in Fig. 5.10. This is due to the shorter path length in the two-ring model. The SB and DB components of the CIR are shown in Fig. 5.10.

The previous discussion was based on the static condition assumption, i.e., $t = 0$

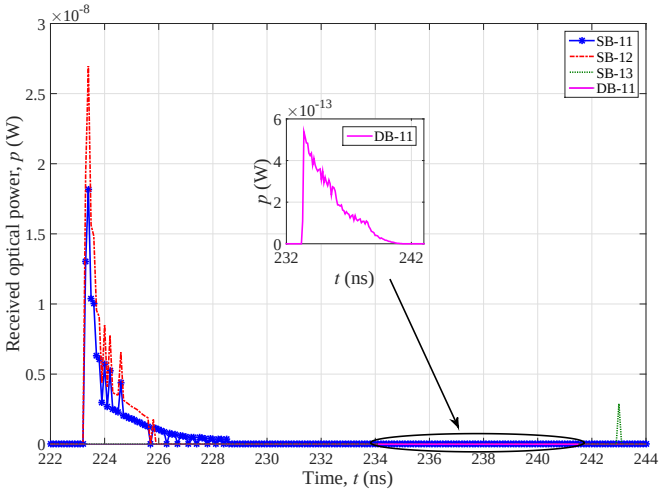

FIGURE 5.10: Received power from SB_11, SB_12, SB_13, and DB_11 components for the combined two-ring model and ellipse model ($t = 0$, $D = 70$ m).

and $D = 70$ m. Let's consider the dynamic condition in which both of the Tx and Rx moving in the same direction with different speeds as detailed in Table 5.4. In terms of SB components in the two-ring model, Fig. 5.11 shows the contribution of the two-ring model when both the Tx and Rx are moving. Here the total power of both SB_11 and SB_12 is considered at specific times. Since the Tx vehicle is moving relatively faster than target Rx vehicle, the received power increases gradually. In this case, the optical path lengths and both AoD and AoA are the main parameters which are effects signal strength.

On the other hand, in terms of the DB component of the CIR in the dynamic mode, simulation results have demonstrated that the received power between 2.7×10^{-10} W and 1.4 $\times 10^{-11}$ W, which are corresponding to Tx-Rx distance 20 m and 70 m, respectively. The former distance represents the minimum distance to maintain DB reflection between two cars. In order to summarise above discussions regarding received power, Fig. 5.12 illustrates the relationships between the received optical powers from LoS, SB, and DB components with Tx-Rx distances. The results are calculated based on the given parameters when the PD is mounted at 0.6 m height.

Since it has been demonstrated that DB components are insufficient enough to be used for further analysis, the rest of this work will focus on SB components.

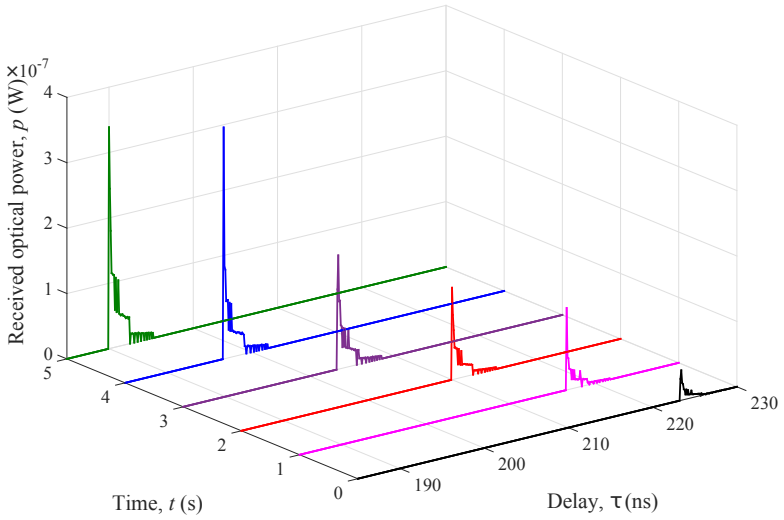

FIGURE 5.11: Received power form SB_11 and SB_12 component (the Tx and Rx are moving, $v_{\mathrm{Tx}} = 21.6$ km/h, $v_{\mathrm{Rx}} = 14.4$ km/h, $t = 0 - 5$ s).

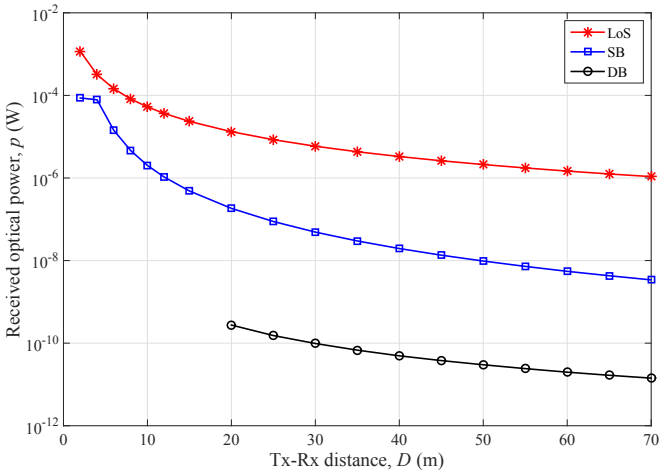

FIGURE 5.12: The received optical power from LoS, SB, and DB components.

5.4.2 VVLC Channel Gain

In terms of channel gain in dB, let's now evaluate the mean channel gain and the distribution of channel gains at a particular distance, specifically 70 m. Following channel gain definition in [94] and based on simulation data we will investigate propagation characteristics for a large ensemble of scatterers locations with different angular distributions. Consequently, the resultant channel gain distribution for the SB components in the two-ring model is illustrated in Fig. 5.13. It can be noticed that the

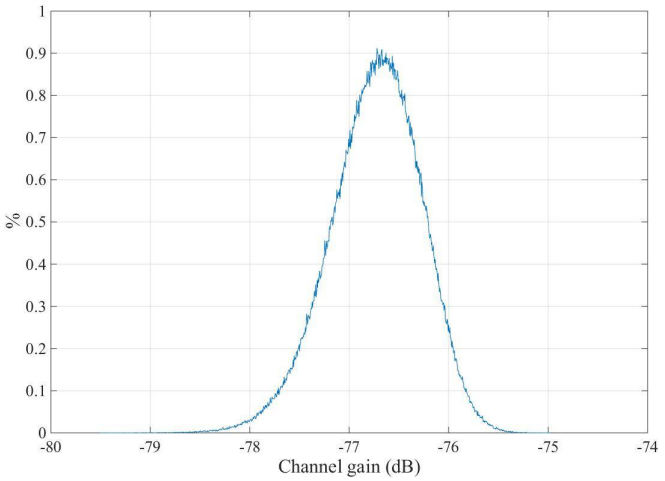

FIGURE 5.13: Channel gain (dB) for SB components in two-ring model.

mean channel gain is -76.73 dB.

In terms of analysing the resultant channel gain distribution in Fig. 5.13, we can notice that the most potential distribution that fit the results is the Gaussian distribution. To evaluate the channel model at the given distance, two methods have been used. First, we performed a Cumulative Distribution Function (CDF) fitting method for the resultant distribution. A Monte Carlo simulation of 10^6 iterations (realisations) is carried out. In each realisation, the value of the AoD/AoA is randomly generated following a uniform distribution. The resultant distribution is then verified by applying empirical CDF technique, which is a built-in function in MATLAB. The CDF fitting result is illustrated in Fig. 5.14. Here, we can notice that the CDF fitting method produces a good fit across all the channel gain samples. Secondly, we use the χ^2- goodness-of-fit test [145]. The χ^2-test is generally used to test the hypothesis that a function $F(x)$ is the distribution of the sample population $x_1, x_2, ..., x_n$. If the sample population deviates too much from $F(x)$ then that hypothesis will be rejected. Here, we will perform the test on all groups of data for the distribution that obtained from SB components in the two-ring model. The result of the simulation is analyzed using χ^2- goodness-of-fit test built-in function in MATLAB. According to that function, the test result is denoted by $\chi^2_{.05}$, which means that the null hypothesis has been estimated at the 5% significance level. Consequently, if $\chi^2_{.05}$ is 1, the test rejects the null hypothesis, while if the returned value $\chi^2_{.05} = 0$, that means the test does not

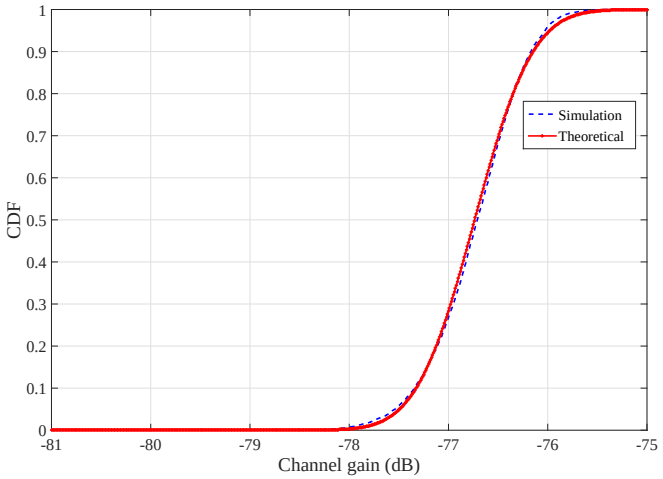

FIGURE 5.14: CDF fitting for simulation results of VVLC channel gain.

reject the null hypothesis at the default 5% significance level. Based on our simulation results, examining the normal distribution has passed the χ^2-test. In terms of results validation, it is worth mentioning that comparable results have been obtained in [94].

5.4.3 RMS Delay Spread

By following the same methodology which is used in Section 5.4.2, in this subsection, the RMS delay spread model for the SB channels has been characterised based on (2.3). Here, Gaussian distribution has been examined again to model VVLC channel RMS delay spread D_{rms}. In this context, Gaussian distribution has passed the χ^2-test firstly. Secondly, we used the Probability Density Function (PDF) fitting method to characterize the results with the theoretical PDF of Gaussian distribution as illustrated in Fig. 5.15. The last figure shows that the Gaussian is a good estimate for RMS delay spread of SB components.

5.5 Summary

VLC technology considers as an alternative and complementary to the RF wireless communications, not only for indoor applications but could also be used for outdoor

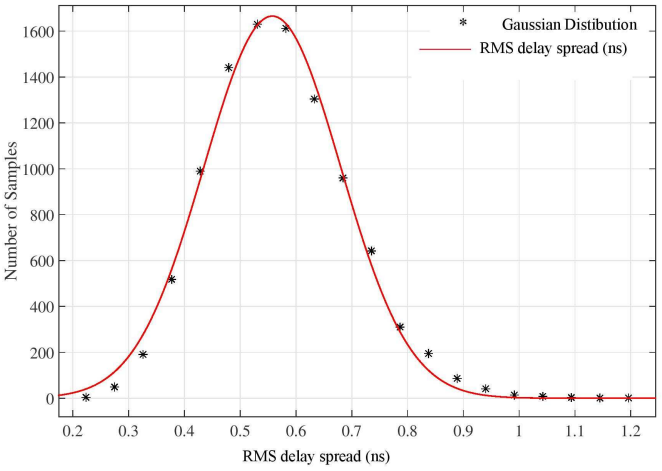

FIGURE 5.15: Curve fitting of channel RMS delay spread histogram for SB components in the two-ring model.

applications. Therefore, in this chapter, the potential of using VLC technology for vehicular communication networks has been investigated. A new 2D mobile RS-GBSM for vehicular VLC SISO channels has been proposed. In order to consider a more practical scenario, a combined two-ring and confocal ellipse model is adopted. VVLC channel characteristics are investigated through a large set of channel impulse responses generated from the proposed RS-GBSM. The received optical powers for LoS, SB, and DB components have been computed along different distances range between 0–70 m. Furthermore, the LoS received power is obtained when the PD is mounted at three different heights. While, in terms of SB components, the traditional fitting methods have confirmed that the Gaussian distributions are the best fit for channel gain in dB for SB components and RMS delay spread. Finally, the results have indicated that the DB components carry inconsiderable optical power.

Chapter 6

A 3D Mobile RS-GBSM for Vehicular VLC Multiple-Input Single-Output (MISO) Channels

6.1 Introduction

In Chapter 5 we have proposed a 2D mobile RS-GBSM for vehicular VLC SISO channels. However, in reality, optical waves are propagating in three dimensions and hence the variations in both vertical and horizontal planes should be considered. Therefore, 3D channel model is more accurate to characterise VVLC channels, particularly for Small Spatial Scale (SSS) communications. Consequently, in this chapter, we propose a new 3D mobile RS-GBSM for non-isotropic VVLC MISO channels. Unlike 2D models, in 3D models, the effective scatterers assumed that they are lying on a 3D regular shape such as a sphere or a cylinder. The proposed 3D RS-GBSM combines a two-sphere model and a confocal elliptic-cylinder model and considers both LoS and SB components. According to the proposed model, we assume that both Left-Side Headlight (LSH) and Right-Side Headlight (RSH) have identical output light distribution. Thus, the received power is composed of LoS and NLoS components. It is worth to mention that the NLoS components are resultant due to the reflection of

LSH and RSH lights across both two-sphere and elliptic-cylinder models. Therefore, the proposed model can be introduced as a new 3D VVLC MISO channel model. Due to their reasonable complexity and mathematical traceability, RS-GBSM have widely been used in conventional vehicular cellular systems to mimic V2V channels in 3D such as [112], [111], [146]. It is worth mentioning that in order to significantly reduce the complexity of the 3D RS-GBSM, only the SB rays via scatterers on the two-sphere model and the elliptic-cylinder model are considered. To conclude, in this chapter, the development of optical wireless channel modelling and simulations are becoming more and more comprehensive and effective through the development from 2D to 3D, from isotropic to non-isotropic, and from SISO to MISO towards more generic, realistic and adaptable channel model for VVLCs.

The rest of this chapter is structured as follows. Section 6.2 describes the proposed VVLC MISO system model including the headlamp and optical receiver models. In Section 6.3, the description of the proposed 3D RS-GBSM and the related geometric derivations are presented. Section 6.4 presents the investigated VVLC channel characteristics based on using von Mises-Fisher (VMF) distribution. Simulation results and analysis are unveiled in Section 6.5. Conclusions are finally drawn in Section 6.6.

6.2 MISO VVLC Model

6.2.1 VVLC System Model

A typical VVLC environment and the corresponding geometrical description of the proposed VVLC MISO system model with the LoS and SB rays is illustrated in Fig. 6.1. In terms of the road traffic, here we consider a SSS VVLC system model deployed in a typical urban canyon environment. In this study, only the SB is considered since the power which is carried by the DB rays is significantly low as it has been demonstrated in the previous work [114], and hence can be ignored especially for outdoor VLCs applications. While in terms of optical wireless channel propagation between the Tx and Rx, we assume that all the effective scatterers are located on 3D

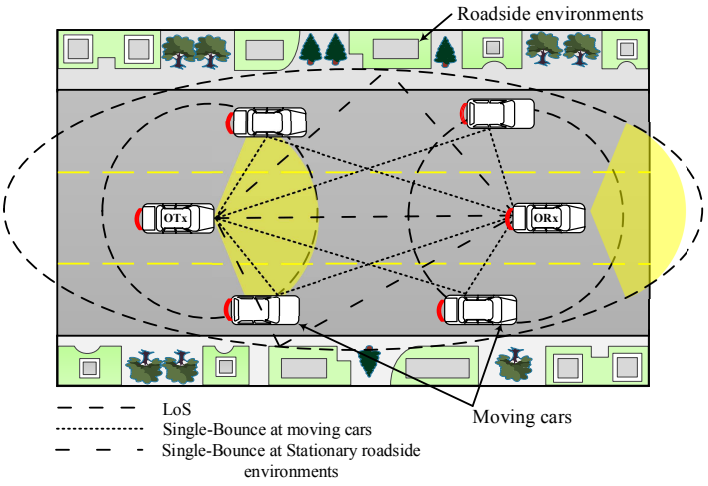

FIGURE 6.1: A typical VVLC environment and the corresponding geometrical description

regular shapes, i.e., two spheres and a confocal elliptic-cylinder. Different from physical scatterers, an effective scatterer may include several physical scatterers which are unresolvable in delay domain [111]. The two-sphere model proposes first and second spheres that model the scatterers around the Tx and Rx, respectively. These scatterers include adjacent moving cars, vans, and trucks. While the elliptic-cylinder model is proposed to model the stationary roadside environments such as buildings, packed cars, road signs, and trees.

In order to introduce the problem of MISO channel modelling, we assumed that VVLC MISO system consists of LSH and RSH headlights with transmitted power of $P_{\text{Tx-LSH}}$ and $P_{\text{Tx-RSH}}$, respectively. While at the receiving side, a non-imaging PIN PD is considered. For OWCs, channel effect is completely characterized by its CIR $h(t)$ [57]. Since each Tx will be connected with the Rx through transmission links (subchannels), therefore, the detailed CIR of the LSH and RSH can be expressed as

$$h(t)_{\text{L}} = h_{\text{L}}^{\text{LoS}}(t) + \sum_{n=1}^{N} h_{\text{L}}^{i,j}(t) + \sum_{n=1}^{N} h_{\text{L}}^{i,j}(t) + \sum_{n=1}^{N} h_{\text{L}}^{i,j}(t) \tag{6.1}$$

and

$$h(t)_{\text{R}} = h_{\text{R}}^{\text{LoS}}(t) + \sum_{n=1}^{N} h_{\text{R}}^{i,j}(t) + \sum_{n=1}^{N} h_{\text{R}}^{i,j}(t) + \sum_{n=1}^{N} h_{\text{R}}^{i,j}(t). \tag{6.2}$$

Note that L/R denotes LSH/RSH throughout this chapter. Here, $i = 1, 2$, which means we consider the contributions from both left side and right side surroundings for each headlight. Here, $i = 1$, for the left side surroundings, while $i = 2$ for the right side surroundings. On the other hand, $j = 1, 2, 3$ denotes there are three components for SB rays, which arrive from the Tx-sphere, the Rx-sphere, and the elliptic-cylinder models, respectively. Consequently, the total received power for the proposed MISO VVLC system is generally defined as

$$P_{\mathrm{r}} = H(0)_{\mathrm{L}}\ P_{\mathrm{t,L}} + H(0)_{\mathrm{R}}\ P_{\mathrm{t,R}}. \tag{6.3}$$

Here, $H(0)_{\mathrm{L}}$ and $H(0)_{\mathrm{R}}$ represent the DC channel gains (as expressed in (3.16)) of left headlight and right headlight, respectively. If we assume that both headlights are transmitting the same power, (6.3) can be rewritten as

$$P_{\mathrm{r}} = P_{\mathrm{t}}\ [H(0)_{\mathrm{L}} + H(0)_{\mathrm{R}}]. \tag{6.4}$$

Equation (6.4) represents the most general equation for describing the received optical power of the proposed system model.

6.2.2 Headlamp Model

According to the final report from European Commission in [147], the advanced headlights must be designed to maximize clarity of the roadway whilst minimizing the glare toward oncoming vehicles. Therefore, the pattern of light produced by headlamp is of vital importance in VVLCs. Headlamps can produce high-beam pattern for long-distance visibility on roads with no oncoming car, and low-beam pattern which provides maximum forward and lateral illumination. In this work, we consider low-beam headlight since our system model has been proposed in a typical urban canyon environment. The illuminance E that can be captured at a specific Rx located at a specific distance of interest, can be expressed as [148]

$$E = \frac{I(\alpha_{\mathrm{T}}, \beta_{\mathrm{T}})\ \cos(\phi_{\mathrm{R}})}{(D_{\mathrm{TR}}^{\mathrm{LoS}})^2}. \tag{6.5}$$

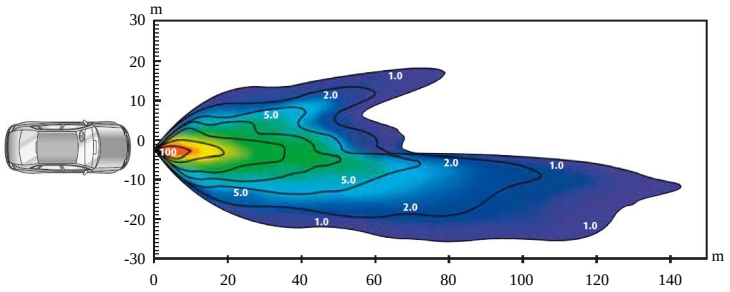

FIGURE 6.2: Isolux diagram of a Xenon lamp

Here, E is the illuminance (lx), $I(\alpha_{\mathrm{T}}, \beta_{\mathrm{T}})$ is the luminous intensity in unit of candela (cd), α_{T} and β_{T} are the azimuth and elevation angles of Tx radiation pattern, respectively, $D_{\mathrm{TR}}^{\mathrm{LoS}}$ is the Tx-Rx distance, and ϕ_{R} is the angle between the light-receiving surface normal and the light incident direction. For instance, the illuminance pattern of a headlamp equipped with a Xenon lamp is presented in Fig. 6.2. This diagram is called an Isolux diagram where lines indicate illuminance E levels in steps. In this example, the illuminance reaches a maximum as 100 lx at the front of the car and minimum of 1 lx at the outer line. However, such illuminance patterns are asymmetrical, therefore usually, the value of $I(\alpha_{\mathrm{T}}, \beta_{\mathrm{T}})$ for a specific luminaire and specific range of α_{T} and β_{T} can be provided based on measurements campaign to produce what so called I-table. For instance, I-table for standard tungsten-halogen headlamp is presented in [144]. Since the existing Halogen and Xenon lamps are not suitable for intensity modulation purposes, whereas no I-table available for advanced LED headlights, we assume that the radiation patterns of both LSH and RSH are following the generalised Lambertian radiation pattern.

6.2.3 Optical Receiver Model

On the other hand, in terms of optical receiver, a non-imaging PIN PD is considered. The PD is modelled as an active area A_{r} collecting the radiation incident at angle ϕ_{R} smaller than Ψ_{FoV}, as expressed in (3.5). In order to increase overall effective collection area for outdoor VLC applications, truncated spherical non-imaging concentrator, i.e., lens is attached to the PD. The optical gain $G(\beta_{\mathrm{R}})$ that can be obtained by the

concentrator is given as [20]

$$G(\beta_{\mathrm{R}}) = \begin{cases} \frac{n_{\mathrm{ind}}^2}{\sin^2(\beta_{\mathrm{R}})} , & 0 \leq \beta_{\mathrm{R}} \leq \Psi_{\mathrm{FoV}} \\ 0 , & \beta_{\mathrm{R}} > \Psi_{\mathrm{FoV}}. \end{cases} \tag{6.6}$$

Here, n_{ind} denotes the refractive index of the concentrator. Furthermore, an optical filter with $T(\beta_{\mathrm{R}})$ transmission coefficient can be deposited onto the concentrator surface or inserted between the concentrator and the PD. The optical filter is normally used to reduce all out-of-band natural and artificial light signals. Using of optical concentrator and filter can highly increase the detected power and decrease ambient noise, respectively, and thus improve system's SNR.

6.3 A Mobile RS-GBSM for VVLC MISO Channels

In this study, the propagation environment is characterized by 3D effective scattering with LoS and NLoS components between the Tx and Rx. Fig. 6.3 and Fig. 6.4 illustrate the proposed 3D mobile RS-GBSM for vehicular VLC MISO channels. This model is the combination of LoS component, SB two-sphere model, and SB elliptic-cylinder model. For readability purposes, Fig. 6.3 only shows the geometry of LoS component and the SB elliptic-cylinder model. The detailed geometry of the SB two-sphere model is shown in Fig. 6.4. In order to describe the proposed model, suppose there are N_1 effective scatterers around the Tx are lying on a sphere of radius R_{T} and the n_1th ($n_1 = 1, ..., N_1$) effective scatterer is denoted by S^{n_1}. Likewise, assume there are N_2 effective scatterers around the Rx are lying on a sphere of radius R_{R} and the n_1th ($n_1 = 1, ..., N_2$) effective scatterer is denoted by S^{n_2}. For the elliptic-cylinder model, N_3 effective scatterers are lying on an elliptic-cylinder with the Tx and Rx located at the foci and the n_3th ($n_3 = 1, ..., N_3$) local scatterer is denoted by S^{n_2}. Ellipse parameters and related relationships are already defined in Chapter 4. Here, the focal points (foci) coincide with firstly, the mid-distance between the headlights, i.e., p and secondly, the position of the Rx, which is denoted by q. The definitions of

TABLE 6.1: Definitions of key geometry parameters.

$D_{\mathrm{TR}}^{\mathrm{LoS}}$	LoS distance between the centre of Tx-sphere and the centre of the Rx-sphere
$R_{\mathrm{T}}, R_{\mathrm{R}}$	radius of the Tx and Rx spheres, respectively
2δ	spacing between the LSH and the RSH
a, b	semi-principal axes of the ellipse
$\theta_{\mathrm{T}}, \theta_{\mathrm{R}}$	orientation of the Tx and Rx the x-y plane, respectively
$\phi_{\mathrm{T}}, \phi_{\mathrm{R}}$	elevation of the Tx and Rx relative to the x-y plane, respectively
$v_{\mathrm{T}}, v_{\mathrm{R}}$	the speeds of the Tx and Rx, respectively
$\gamma_{\mathrm{T}}, \gamma_{\mathrm{R}}$	moving directions of the Tx and Rx in the x-y plane, respectively
$\alpha_T^{(n_i)} (i = 1, 2)$	azimuth angle of departure (AAoD) of the waves that impinge on the effective scatterers $s^{(n_i)}$
$\alpha_R^{(n_i)} (i = 1, 2)$	azimuth angle of arrival (AAoA) of the waves traveling from the effective scatterers $s^{(n_i)}$
$\beta_T^{(n_i)} (i = 1, 2)$	elevation angle of departure (EAoD) of the waves that impinge on the effective scatterers $s^{(n_i)}$
$\beta_R^{(n_i)} (i = 1, 2)$	elevation angle of arrival (EAoA) of the waves traveling from the effective scatterers $s^{(n_i)}$
$\varepsilon_{\mathrm{Tx}-n_i}$	distances from the Tx to scatterers n_i, $(i = 1, 2, 3)$
$\varepsilon_{n_1-\mathrm{Rx}}$	distances from scatterers n_1 to the Rx
$\xi_{\mathrm{p}-n_3}$	distances from the centre of Tx-sphere to scatterer n_3
$\xi_{n_3-\mathrm{q}}$	distances from scatterer n_3 to the Rx

TABLE 6.2: Probable optical paths

Component	**Optical Path**	**Distance**
LoS	$\mathrm{Tx_{L/R}} \rightarrow \mathrm{Rx}$	$D_{\mathrm{TR}}^{\mathrm{LoS}}$
1- SB1	$\mathrm{Tx_{L/R}} \rightarrow n_1 \rightarrow$ Rx	$\varepsilon_{\mathrm{Tx}-n_1} + \varepsilon_{n_1-\mathrm{Rx}}$
2- SB2	$\mathrm{Tx_{L/R}} \rightarrow n_2 \rightarrow$ Rx	$\varepsilon_{\mathrm{Tx}-n_2} + R_{\mathrm{R}}$
3- SB3	$\mathrm{Tx_{L/R}} \rightarrow n_3 \rightarrow$ Rx	$\varepsilon_{\mathrm{Tx}-n_3} + \xi_{n_3-\mathrm{q}}$

key geometry parameters of Fig. 6.3 and Fig. 6.4, as well as optical paths are presented in Table 6.1 and Table 6.2, respectively.

Consequently, the total channel gain can be represented as a superposition of the optical waves coming from direct direction, i.e., LoS and different directions determined by the distribution of the local scatterers, as detailed in next subsections.

6.3.1 The LoS Link

Since we assumed that both LSH and RSH have an identical output light pattern, i.e., Lambertian pattern, the detailed derivations for their contribution in the LoS link will be presented here. In the proposed model, if the Tx and Rx are stationary, the LoS component of the CIR is deterministic and it is proportional to the square of the distance between the Tx and Rx (the inverse square law), the active area of the PD

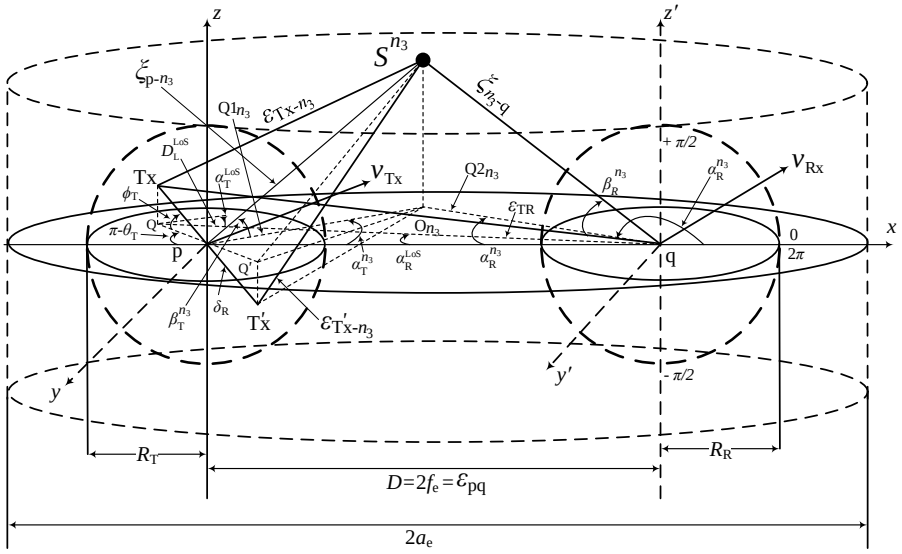

FIGURE 6.3: The proposed 3D RS-GBSM for VVLC MISO channels (only showing the detailed geometry of LoS component and SB rays in the elliptic-cylinder model).

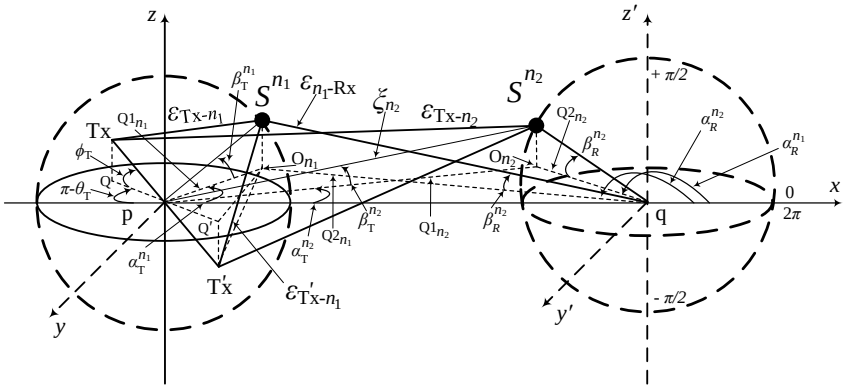

FIGURE 6.4: The detailed geometry of the SB rays in the two-sphere model of the proposed 3D RS-GBSM for VVLC MISO channels.

A_r, the LoS Azimuth Angle of Departure (AAoD) α_T^{LoS}, and the LoS Azimuth Angle of Arrival (AAoA) α_R^{LoS}. Therefore, equation (4.6) in [35] can be expressed as

$$h_{L/R}^{LoS}(t) = \frac{(m+1)\ G(\beta_R)T(\beta_R)A_r}{2\pi(D_{L/R}^{LoS})^2}\ \cos(\beta_{T,L/R}^{LoS})^m \times \cos(\beta_{R,L/R}^{LoS})\ \delta(t - \frac{D_{L/R}^{LoS}}{c}) \tag{6.7}$$

where, $D_{\mathrm{L/R}}^{\mathrm{LoS}} = \sqrt{(\delta_{\mathrm{L/R}})^2 + \varepsilon_{\mathrm{pq}}^2}$, $\delta(.)$ refers to the Dirac delta function, $T(\phi_{\mathrm{R}})$ is the transmittance of an optical band-pass filter, $G(\phi_{\mathrm{R}})$ is the gain of a non-imaging concentrator, and c is speed of light. It should be mentioned that we further assumed that both headlights and the PD are equipped at the same height, namely, 0.6 m. Therefore, eq. (6.7) was written in terms of the LoS EAoD $\beta_{\mathrm{T}}^{\mathrm{LoS}}$, and EAoA $\beta_{\mathrm{R}}^{\mathrm{LoS}}$. On the other hand, if the Tx and Rx are moving in the same direction, (6.7) can be rewritten as

$$h_{\mathrm{L/R}}^{\mathrm{LoS}}(t) = \frac{(m+1)\ G(\beta_{\mathrm{R}})T(\beta_{\mathrm{R}})A_{\mathrm{r}}}{2\pi(D_{\mathrm{TR,L/R}}^{\mathrm{LoS}})^2}\ \cos(\beta_{\mathrm{T,L/R}}^{\mathrm{LoS}})^m \times \cos(\beta_{\mathrm{R,L/R}}^{\mathrm{LoS}})\ \delta(t - \frac{D_{\mathrm{TR,L/R}}^{\mathrm{LoS}}}{\mathrm{c}}). \tag{6.8}$$

Here, $D_{\mathrm{TR,L/R}}^{\mathrm{LoS}}$ determines the time-varying distance between the Txs and the target Rx. Since the LSH and RSH are located at the same distance from the Rx, $D_{\mathrm{TR,L/R}}^{\mathrm{LoS}}$ can be referred as D_{TR} and given as

$$D_{\mathrm{TR}}^{\mathrm{LoS}}(t) = \varepsilon_{\mathrm{TR}}(t_0) - [\varepsilon_{\mathrm{Tx}}(t) - \varepsilon_{\mathrm{Rx}}(t)], \quad \upsilon_{\mathrm{Tx}} > \upsilon_{\mathrm{Rx}}. \tag{6.9}$$

Here, $\varepsilon_{\mathrm{TR}}(t_0)$, $\varepsilon_{\mathrm{Tx}}(t)$, and $\varepsilon_{\mathrm{Rx}}(t)$ are the initial Tx-Rx distance, the Tx distance at the given speed after a specific time, and the target Rx distance at the given speed after a specific time, respectively. If the Tx and Rx are moving with speeds υ_{Tx} and υ_{Rx} in directions determined by the angles of motion γ_{Tx} and γ_{Rx}, respectively, the distances $\varepsilon_{\mathrm{Tx}}(t)$ and $\varepsilon_{\mathrm{Rx}}(t)$, can be written as $\varepsilon_{\mathrm{Tx}}(t) = \upsilon_{\mathrm{Tx}} \times t \times \cos(\gamma_{\mathrm{Tx}})$ and $\varepsilon_{\mathrm{Rx}}(t) = \upsilon_{\mathrm{Rx}} \times t \times \cos(\gamma_{\mathrm{Rx}})$, respectively.

6.3.2 Single-Bounce Link

The complexity of calculating the CIR grows exponentially with the number of reflections k [44]. Therefore, this work considers the CIR for only primary reflection. Furthermore, unlike indoor VLCs, outdoor environment is a very complex and dynamic environment that can affect the optical wireless channel characteristics and makes the power of the second reflection insignificant as demonstrated in chapter 5. Hence, only the first reflection has been considered in this work. Furthermore, to

reduce the complexity in terms of NLoS scenario, the mode number is assumed to be 1.

6.3.2.1 SB Components in Tx-Sphere Model

In terms of the SB components of the CIR within the Tx-sphere model, $h(t)^{(1)}_{\mathrm{L/R}}$ resulting from the LSH and RSH can be written as

$$\begin{aligned} h^{(1)}_{\mathrm{L/R}}(t) = \lim_{N_1\to\infty} \sum_{n_1=1}^{N_1} & \frac{G(\beta_{\mathrm{R}})T(\beta_{\mathrm{R}})A_{\mathrm{r}}\ \rho_{\mathrm{Vehicles}}}{\pi(\varepsilon^{(1)}_{\mathrm{L/R}})}\ \cos(\alpha^{(1)}_{\mathrm{T,L/R}}) \\ & \times \cos(\beta^{(1)}_{\mathrm{T,L/R}})\ \cos(\alpha^{(1)}_{\mathrm{R,L/R}}) \\ & \times \cos(\beta^{(1)}_{\mathrm{R,L/R}})\ \delta(t - \frac{\varepsilon^{(1)}_{\mathrm{L/R}}}{\mathrm{c}}). \end{aligned} \tag{6.10}$$

Referring to Fig. 6.4, for the LSH, the distance $\varepsilon^{(1)}_{\mathrm{L}}$ in (6.10) can be written as

$$\varepsilon^{(1)}_{\mathrm{L}} = \varepsilon_{\mathrm{T_x}-n_1} + \varepsilon_{n_1-\mathrm{R_x}}. \tag{6.11}$$

The distance $\mathrm{p} - \mathrm{O}_{\mathrm{n_1}}$ $(= Q1_{n_1})$ can be written as $Q1_{n_1} = R_{\mathrm{T}}\ \cos(\beta_{\mathrm{T,L}})$. While the distance $\mathrm{O}_{n_1} - \mathrm{q}$ $(= Q2_{n_1})$ is given as

$$Q2_{n_1} = \sqrt{(Q1_{n_1})^2 + 4f_{\mathrm{e}}^2 - 4f_{\mathrm{e}}(Q1_{n_1})\ \cos(\alpha_{\mathrm{T,L}})}. \tag{6.12}$$

Accordingly, and after mathematical manipulation, the distance between the LSH and a scatterer, which is lying on the Tx-sphere can be written as

$$\begin{aligned} \varepsilon_{\mathrm{T_x}-n_1} = & (R_{\mathrm{T}}^2 + \delta_{\mathrm{L}}^2 - 2\delta_{\mathrm{L}}R_{\mathrm{T}}\ \cos(\phi_{\mathrm{T,L}}) \\ & \times \cos(\beta_{\mathrm{T,L}})\ \cos(\theta_{\mathrm{T,L}} - \alpha_{\mathrm{T,L}}) \\ & - 2\delta_{\mathrm{L}}R_{\mathrm{T}}\ \sin(\phi_{\mathrm{T,L}})\ \sin(\beta_{\mathrm{T,L}}))^{0.5}. \end{aligned} \tag{6.13}$$

While the distance between the above scatterer and the Rx, i.e., q is $\varepsilon_{n_1-\mathrm{R_x}} = Q2_{n_1}/\cos(\beta_{\mathrm{R,L}})$.

On the other hand, in terms of the RSH, the distance between the right headlight and a scatterer, which is lying on the Tx-sphere, can be obtained by application of trigonometry in triangles $\mathrm{p}-\mathrm{Q}'-\mathrm{O}_{n_1}$, $\mathrm{Q}'-\mathrm{Tx}'-S_{n_1}$, and $\mathrm{Q}'-\mathrm{Tx}'-\mathrm{O}_{n_1}$ to get

$$\varepsilon_{\mathrm{T_x}'-n_1} = \sqrt{R_{\mathrm{T}}^2 + \delta_{\mathrm{R}}^2 + A1 - B1} \tag{6.14}$$

where,

$$A1 = 2\ R_{\mathrm{T}}\delta_{\mathrm{T}}\ \sin(\phi_{\mathrm{T,R}})\ \sin(\beta_{\mathrm{T,R}}) \tag{6.15}$$

and

$$B1 = 2\ R_{\mathrm{T}}\delta_{\mathrm{T}}\ \cos(\phi_{\mathrm{T,R}})\ \cos(\beta_{\mathrm{T,R}})\ \cos(\theta_{\mathrm{T,R}} - \alpha_{\mathrm{T,R}}). \tag{6.16}$$

Note that the azimuth/elevation angle of departure (AAoD/EAoD), (i.e., $\alpha^{(1)}_{\mathrm{T,L/R}}$, $\beta^{(1)}_{\mathrm{T,L/R}}$) and azimuth/elevation angle of arrival (AAoA/EAoA), (i.e., $\alpha^{(1)}_{\mathrm{R,L/R}}$, $\beta^{(1)}_{\mathrm{R,L/R}}$), are correlated for SB rays. Consequently, we can derive the relationship between the AoDs and AoAs as

$$\alpha^{(1)}_{\mathrm{R,L/R}} = \arcsin\left(\frac{R_{\mathrm{T}}\ \cos(\beta_{\mathrm{T,L/R}})\ \sin(\alpha_{\mathrm{T,L/R}})}{\sqrt{(Q1_{n_1})^2 + 4f_{\mathrm{e}}^2 + 4f_{\mathrm{e}}(Q1_{n_1})\cos(\alpha_{\mathrm{T,L/R}})}}\right) \tag{6.17}$$

and

$$\beta^{(1)}_{\mathrm{R,L/R}} = \arctan\left(\frac{R_{\mathrm{T}}\ \sin(\beta_{\mathrm{T,L/R}})}{\sqrt{(Q1_{n_1})^2 + 4f_{\mathrm{e}}^2 + 4f_{\mathrm{e}}(Q1_{n_1})\cos(\alpha_{\mathrm{T,L/R}})}}\right). \tag{6.18}$$

6.3.2.2 SB Components in Rx-Sphere Model

Regarding the SB components of the CIR within the Rx-sphere model, $h(t)^{(2)}_{\mathrm{L/R}}$ resulting from the LSH and RSH can be written as

$$\begin{aligned} h(t)^{(2)}_{\mathrm{L/R}} = \lim_{N_2\to\infty} \sum_{n_2=1}^{N_2} & \frac{G(\beta_{\mathrm{R}})T(\beta_{\mathrm{R}})A_{\mathrm{r}}\ \rho_{\mathrm{Vehicles}}}{\pi(\varepsilon^{(2)}_{\mathrm{L/R}})^2}\ \cos(\alpha^{n_2}_{\mathrm{T,L/R}}) \\ & \times \cos(\beta^{n_2}_{\mathrm{T,L/R}})\ \cos(\alpha^{n_2}_{\mathrm{R,L/R}})\ \cos(\beta^{n_2}_{\mathrm{R,L/R}}) \\ & \times \delta(t - \frac{\varepsilon^{(2)}_{\mathrm{L/R}}}{\mathrm{c}}). \end{aligned} \tag{6.19}$$

For the LSH, the distance $\varepsilon_{\mathrm{L}}^{(2)}$ in (6.19) is given as

$$\varepsilon_{\mathrm{L}}^{(2)} = \varepsilon_{\mathrm{T_x}-n_2} + \mathrm{R_R}. \tag{6.20}$$

In terms of optical path lengths within the Rx-sphere model, the distance $\mathrm{p} - \mathrm{O}_{n_2}$ $(= Q1_{n_2})$ can be written as

$$Q1_{n_2} = \sqrt{4f_{\mathrm{e}}^2 + (Q2_{n_2})^2 - 4f_{\mathrm{e}}(Q2_{n_2})\,\cos(\alpha_R)}. \tag{6.21}$$

Here, $Q2_{n_2} = R_{\mathrm{R}}\,\cos(\beta_{\mathrm{R}})$. Hence,

$$\xi_{n_2} = \sqrt{Q1_{n_2}^2 + R_{\mathrm{R}}^2\,\sin^2(\beta_{\mathrm{R}})}. \tag{6.22}$$

The distance between the LSH and a scatterer, which is lying on the Rx-sphere $\varepsilon_{\mathrm{Tx}-n_2}$, can be found by applying Pythagoras's theorem and the law of sines in appropriate triangles to get

$$\varepsilon_{\mathrm{Tx}-n_2} = \sqrt{A2^2 + B2^2}. \tag{6.23}$$

Here,

$$\begin{aligned} A2 = (&\delta^2\,\cos^2(\phi_{\mathrm{T}}) + (Q1_{n_2})^2 \\ &- 2\delta\,(Q1_{n_2})\,\cos(\phi_{\mathrm{T}})\,\cos(\theta_{\mathrm{T}} - \alpha_{\mathrm{T}}))^{0.5} \end{aligned} \tag{6.24}$$

and

$$\begin{aligned} B2 = &R_{\mathrm{R}}^2\,\sin^2(\beta_{\mathrm{R}}) - 2\delta R_{\mathrm{R}}\,\sin(\beta_{\mathrm{R}})\,\sin(\theta_{\mathrm{T}}) \\ &+ \delta^2\,\sin^2(\phi_{\mathrm{T}}). \end{aligned} \tag{6.25}$$

On the other hand, in terms of the RSH, the distance between the RSH and a scatterer that lying on the Rx-sphere $\varepsilon_{\mathrm{T_x}'-n_2}$, can be written as

$$\varepsilon_{\mathrm{T_x}'-n_2} = \sqrt{R_{\mathrm{R}}^2\,\sin^2(\beta_{\mathrm{R}}) + \delta^2\,\sin^2(\phi_{\mathrm{T}}) + A3 + B3}. \tag{6.26}$$

Here,

$$\begin{aligned} A3 = &\delta^2\,\cos^2(\phi_{\mathrm{T}}) + Q1_{n_2}^2 \\ &+ 2\delta\,Q1_{n_2}\,\cos(\phi_{\mathrm{T}})\,\cos(\theta_{\mathrm{T}} - \alpha_{\mathrm{T}}) \end{aligned} \tag{6.27}$$

and

$$B3 = 2\delta R_{\mathrm{R}} \sin(\phi_{\mathrm{T}})\cos(\beta_{\mathrm{R}}). \tag{6.28}$$

Since AAoD/EAoD and AAoA/EAoA are correlated for SB rays in Rx-sphere model, the relationship between the AoDs and AoAs can be expressed as

$$\beta^{(2)}_{\mathrm{T,L/R}} = \arcsin\left(\frac{R_{\mathrm{R}} \sin(\beta_{\mathrm{R,L/R}})}{\sqrt{(R^2_{\mathrm{R}} + 4f^2_{\mathrm{e}} + 4f_{\mathrm{e}}R_{\mathrm{R}}C3}}\right) \tag{6.29}$$

Here, $C3 = \cos(\beta_{\mathrm{R,L/R}})\ \cos(\alpha_{\mathrm{R,L/R}})$. While

$$\alpha^{(2)}_{\mathrm{T,L/R}} = \arcsin\left(\frac{R_{\mathrm{R}}\ \cos(\beta_{\mathrm{R,L/R}})\ \sin(\alpha_{\mathrm{R,L/R}})}{Q1_{n_2}}\right). \tag{6.30}$$

6.3.2.3 SB Components in Elliptic-Cylinder Model

In terms of the SB components of the CIR within the elliptic-cylinder model, $h(t)^{(3)}_{\mathrm{L/R}}$ resulting from the LSH and RSH can be expressed as

$$\begin{aligned} h^{(3)}_{\mathrm{L/R}}(t) = \lim_{N_3\to\infty} \sum_{n_3=1}^{N_3} & \frac{G(\beta_{\mathrm{R}})T(\beta_{\mathrm{R}})A_{\mathrm{r}}\ \rho_{\mathrm{Roadside}}}{\pi(\varepsilon^{(3)}_{\mathrm{L/R}})^2}\ \cos(\alpha^{n_3}_{\mathrm{T,L/R}}) \\ & \times \cos(\beta^{n_3}_{\mathrm{T,L/R}})\ \cos(\alpha^{n_3}_{\mathrm{R,L/R}})\ \cos(\beta^{n_3}_{\mathrm{R,L/R}}) \\ & \times \delta(t - \frac{\varepsilon^{(3)}_{\mathrm{L/R}}}{\mathrm{c}}). \end{aligned} \tag{6.31}$$

Referring to Fig. 6.3, for the LSH, the distance $\varepsilon^{(3)}_{\mathrm{L}}$ in (6.31) can be written as

$$\varepsilon^{(3)}_{\mathrm{L}} = \varepsilon_{\mathrm{T_x}-n_3} + \varepsilon_{n_3-\mathrm{q}}. \tag{6.32}$$

The optical path lengths within the elliptic-cylinder model can be derived based on pure elliptic-cylinder properties mentioned above. The distance $\mathrm{p} - \mathrm{O}_{n_3}$ $(= Q1_{n_3})$ can be written as

$$Q1_{n_3} = \sqrt{(Q2_{n_3})^2 + (D)^2 - 2(Q2_{n_3})(D)\ \cos(\alpha_{\mathrm{R,L}}^{n_3})}. \tag{6.33}$$

While the distance $\mathrm{O}_{n_3} - \mathrm{q}$ $(= Q2_{n_3})$ is given as

$$Q2_{n_3} = \xi_{n_3-\mathrm{q}}\ \cos(\beta_{\mathrm{R,L}}^{n_3}). \tag{6.34}$$

Based on elliptic-cylinder properties and after some manipulation we can get

$$\xi_{n_3-\mathrm{q}} = \frac{2a_{\mathrm{e}} - Q_{n_3}}{\cos(\beta_{\mathrm{R,L}}^{n_3})} \tag{6.35}$$

and

$$\xi_{\mathrm{p}-n_3} = \sqrt{Q_{n_3}^2 + (\xi_{n_3-\mathrm{q}})^2\ \sin^2(\beta_{\mathrm{R,L}}^{n_3})} \tag{6.36}$$

where

$$Q_{n_3} = \frac{a_{\mathrm{e}}^2 + f_{\mathrm{e}}^2 + 2a_{\mathrm{e}}f_{\mathrm{e}}\ \cos(\alpha_{\mathrm{R,L}}^{n_3})}{a_{\mathrm{e}} + f_{\mathrm{e}}\ \cos(\alpha_{\mathrm{R,L}}^{n_3})} \tag{6.37}$$

The distance between the LSH and a scatterer that lying on the elliptic-cylinder model $\varepsilon_{\mathrm{T_x}-n_3}$, can be written as

$$\varepsilon_{\mathrm{Tx}-n_3} = \sqrt{A4^2 + B4^2}. \tag{6.38}$$

Here,

$$A4 = Q1_{n_3}^2 - 2\delta\ Q1_{n_1}\ \cos(\phi_{\mathrm{T}})\ \cos(\theta_{\mathrm{T}} - \alpha_{\mathrm{T}}) \tag{6.39}$$

and

$$\begin{aligned} B4 = \delta^2 + \xi_{n_3-\mathrm{q}}^2\ \sin^2(\beta_{\mathrm{R}}) - 2\delta\ \xi_{n_3-\mathrm{q}} \\ \times \sin(\beta_{\mathrm{R}})\ \sin(\phi_{\mathrm{T}}). \end{aligned} \tag{6.40}$$

On the other hand, regarding the RSH, the distance between the RSH and a scatterer that lying on the elliptic-cylinder model $\varepsilon_{\mathrm{T_x}'-n_3}$, can be written as

$$\varepsilon_{\mathrm{T_x}'-n_3} = \sqrt{\delta^2\ \sin^2(\phi_{\mathrm{T}}) + A5 - B5}. \tag{6.41}$$

Here,

$$A5 = D^2 + \xi_{n_3-\mathrm{q}}^2 - 2D\ \xi_{n_3-\mathrm{q}}\cos(\beta_{\mathrm{R}})\cos(\alpha_{\mathrm{R}}) \tag{6.42}$$

and

$$B5 = 2D\delta\xi_{n_3-\mathrm{q}}\sin(\phi_{\mathrm{T}})\cos(\alpha_{\mathrm{R}}). \tag{6.43}$$

Since the correlation between AAoD/EAoD and AAoA/EAoA is still valid in elliptic-cylinder model, the relationship between the AAoAs and AAoDs can be expressed as

$$\alpha_{\mathrm{T,L/R}}^{(3)} = \arcsin\left(\frac{\xi_{n_3-\mathrm{q}}\sin(\beta_{\mathrm{R,L/R}})}{\xi_{\mathrm{q}-n_3}}\right) \tag{6.44}$$

While, the relationship between the EAoAs and EAoDs can be written as

$$\beta_{\mathrm{T,L/R}}^{(3)} = \arcsin\left(\frac{\xi_{n_3-\mathrm{q}}\cos(\beta_{\mathrm{R,L/R}})\sin(\alpha_{\mathrm{R,L/R}})}{Q1_{n_3}}\right). \tag{6.45}$$

6.4 VVLC Channel Characteristics

6.4.1 VMF distribution

For the theoretical RS-GBSM, the number of scatterers tends to infinity. However, in this study, only the discrete AAoD $\alpha_{\mathrm{T}}^{(n_i)}$, EAoD $\beta_{\mathrm{T}}^{(n_i)}$, AAoA $\alpha_{\mathrm{R}}^{(n_i)}$, and EAoA $\beta_{\mathrm{R}}^{(n_i)}$ will be considered. In order to jointly consider the impact of the azimuth and elevation angles on channel statistics, VMF PDF has been used to characterise the distribution of effective scatterers. The VMF distribution is commonly used to describe directional data. It is parameterized by a mean direction and a concentration factor k_{c}. VMF PDF is defined as [149]

$$f(\alpha,\beta) = \frac{k_{\mathrm{c}}\cos(\beta)}{4\pi\sinh(k_{\mathrm{c}})}\mathrm{e}^{k_{\mathrm{c}}[\cos(\beta_0)\cos(\beta)\cos(\alpha-\alpha_0)+\sin(\beta_0)\ \sin(\beta)]}. \tag{6.46}$$

Here, $\alpha \in (-\pi,\pi)$ and $\beta \in (-\pi/2,\pi/2)$, while $\alpha_0 \in (-\pi,\pi)$ and $\beta_0 \in (-\pi/2,\pi/2)$ refer to the mean values of the azimuth angle α and elevation angle β, respectively,

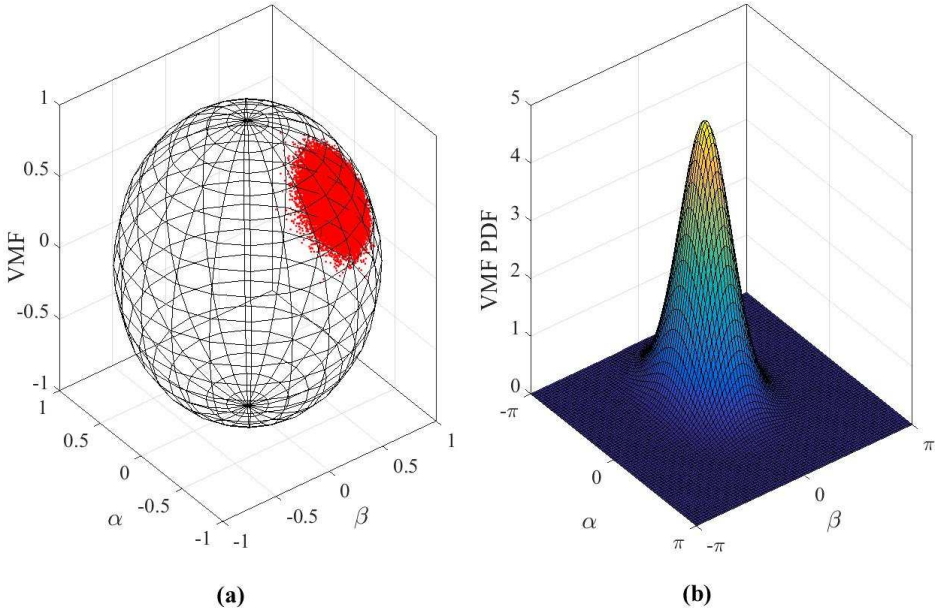

FIGURE 6.5: (a) The VMF distribution on the unit sphere in 3D and (b) VMF PDF ($\alpha_0 = 10°$, $\beta_0 = 30°$, $k = 30$).

and k_c ($k_c \geqslant 0$) is a real-valued parameter that controls the concentration of the distribution relative to the mean direction that identified by α_0 and β_0. To demonstrate the VMF on the unit sphere in 3D space, we set $\alpha_0 = 10°$, $\beta_0 = 2°$, and $k_c = 70$ as an example and plot the scatterers (10000 points) that embedded in the 3D Euclidean space to obtain the distribution that shown in Fig. 6.5(a). While Fig. 6.5(b) illustrates the corresponding VMF PDF when $\alpha_0 = 0°$, $\beta_0 = 31.6°$, and $k_c = 3.6$. According to the VMD, the larger the value of k_c, the VMF PDF is more concentrated towards the mean direction. Thus for $k_c \to 0$ the distribution is isotropic, while for $k_c \to \infty$ the distribution becomes extremely nonisotropic.

6.4.2 Channel DC Gain

Let us now consider that LSH and RSH are VVLC links with Lambertian sources, a receiver with an optical band-pass filter of transmission $T(\beta_R)$ and a nonimaging

concentrator of gain $G(\beta_{\mathrm{R}})$, the channel DC gain for the LoS links can be expressed as

$$H(0)_{\mathrm{L/R}}^{\mathrm{LoS}} = \begin{cases} \frac{T(\beta_{\mathrm{R}})G(\beta_{\mathrm{R}})A_{\mathrm{r}}\cos(\beta_{\mathrm{T,L/R}}^{\mathrm{LoS}})\cos(\beta_{\mathrm{R,L/R}}^{\mathrm{LoS}})}{\pi(D_{\mathrm{TR,L/R}}^{\mathrm{LoS}})^2} & 0 < \beta_{\mathrm{R,L/R}} \leqslant \Psi_{\mathrm{FoV}} \\ 0 & \beta_{\mathrm{R,L/R}} > \Psi_{\mathrm{FoV}}. \end{cases} \tag{6.47}$$

Here, (m=1). On the other hand, in order to consider the joint effect of azimuth and elevation angles on the optical wireless channel, we need to consider the gain of all reflected paths by performing the double integral of VMF PDF, i.e., the volume of 6.5(a). Therefore, channel DC gain of LSH and RSH in NLoS scenario can be written as

$$H(0)_{\mathrm{L/R}}^{\mathrm{SB}} = \begin{cases} \int_{-\pi/2}^{\pi/2}\int_{-\pi/2}^{\pi/2} I_{L,R}(\alpha,\beta)\ h_{L,R}(t)\ f_{L,R}(\alpha,\beta)\ d\alpha\ d\beta & ,0 < \beta_{\mathrm{R,L/R}} \leqslant \Psi_{\mathrm{FoV}} \\ 0 & ,\beta_{\mathrm{R,L/R}} > \Psi_{\mathrm{FoV}}. \end{cases} \tag{6.48}$$

It worth mentioning that we applied the same criteria that used in Section 4.3.

6.4.3 Noise Modelling

For outdoor VLC applications, the optical noise produces by background solar radiation during the daytime and artificial light (i.e., streetlights, vehicles lights, and advertising screens) at nighttime [138]. Optical noise is a decisive factor in determining link performance. The total noise at the Rx side is comprised of 1) the shot noise σ_{sh}^2, which is induced by the received photocurrent, 2) background noise σ_{b}^2 resulting from the ambient light sources, 3) dark current noise σ_{d}^2, that caused by the reverse leakage current which flows through the PD in the absence of light, and 4) thermal noise σ_{th}^2, which is induced by the receiver's electronics such as the resistive element. Consequently, the total noise variance defined as [20]

$$\sigma_{\mathrm{total}}^2 = \sigma_{\mathrm{sh}}^2 + \sigma_{\mathrm{b}}^2 + \sigma_{\mathrm{d}}^2 + \sigma_{\mathrm{th}}^2. \tag{6.49}$$

According to [20], the shot and thermal noise variances are given by

$$\sigma_{\mathrm{sh}}^2 = 2qR_\lambda P_{\mathrm{r}} B_{\mathrm{VLC}} + 2qI_B I_2 B_{\mathrm{VLC}} \tag{6.50}$$

and

$$\sigma_{\mathrm{th}}^2 = \frac{8\pi k_{\mathrm{B}} T_{\mathrm{k}}}{G_{\mathrm{ol}}} C_{\mathrm{PD}} A_{\mathrm{r}} I_2 B_{\mathrm{VLC}}^2 + \frac{16\pi^2 k_{\mathrm{B}} T_{\mathrm{k}} \Gamma_{\mathrm{FET}}}{g_{\mathrm{m}}} C_{\mathrm{PD}} A_{\mathrm{r}}^2 I_3 B_{\mathrm{VLC}}^3 \tag{6.51}$$

The other noise contributions in (6.49) can be obtained according to [20] (Equation 4.7). In this study, we have adopted IM/DD that employing on-off keying (OOK) scheme. Therefore, the SNR at the receiver side is given as [20]

$$\mathrm{SNR} = \frac{(R_\lambda \ P_{\mathrm{r}})^2}{\sigma_{\mathrm{total}}^2}. \tag{6.52}$$

6.5 Results and Analysis

In performing simulations, the key parameters for the proposed system model are summarised in Table 6.3. The body of the vast majority of vehicles is made from steel. Therefore, average painted steel reflectance ρ_{Vehicles} will be considered. Likewise, for the roadside environment, average concrete reflectance ρ_{Roadside} has been selected. The most important VVLC channel characteristics have been studied in below subsections.

6.5.1 Received Optical Power

In this section, the received wireless optical power is analysed based the proposed VLC MISO channel model parameters.

6.5.1.1 LoS components

In the proposed model we assume that the Tx and Rx are moving in the same direction. Since the drivers try to keep the car centered in the current lane, we assume that the

TABLE 6.3: Key parameters used in simulations.

Model Parameters	
The initial Tx-Rx distance	70 m
Semi-major a & semi-minor b axes	40 m, 19 m
Tx speed υ_{Tx}	21.6 km/h
Rx speed υ_{Rx}	14.4 km/h
Sphere radius $(R_{\mathrm{T}}, R_{\mathrm{R}})$	4 m
Lane width	3.5 m [140]
Roadside width	2.2 m [141]
Stopping distance (d_{SD})	6 m [150]
Vehicles reflectivity $(\rho_{\mathrm{Vehicles}})$	0.8 [142]
Roadside reflectivity $(\rho_{\mathrm{Roadside}})$	0.4 [143]
Mode number (m)	1
PD Area	1 cm^2
Luminous intensity (I)	8830 cd [144]
PD field of view Ψ_{FoV}	80°
Number of scatterers	100
Capacitance of PD per unit area (C_{PD})	112 pF/cm^2 [12]
Load resistance (R_{s})	50 Ω [20]
Noise bandwidth factors I_2 and I_3	0.562 and 0.0868 [138]
FET channel noise factor (Γ_{FET})	1.5 [20]
Boltzmann's constant (k_{B})	1.38×10^{-23} J/K
Absolute temperature (T_{k})	298 K
Electric charge (q)	1.6×10^{-19} C
Open-loop voltage gain (G_{ol})	10 [138]
FET transconductance (g_{m})	30 mS [139]
VLC system bandwidth B_{VLC}	20 MHz
Background noise current (I_{B})	5100 μA [12]

reference projection of the Tx vehicle is the lane centre as shown in Fig. 6.1. The target vehicle Rx can be located either in the same lane or in an adjacent lane. The received power will be determined firstly based on the Tx-Rx distance. The following main parameters were chosen for our simulations. The initial distance (at $t = 0$) between the Tx vehicle and Rx vehicle is 70 m and they are moving with speed of 6 m/s (21.6 km/h) and 4 m/s (14.4 km/h), respectively, in the same direction, i.e., $\gamma_{\mathrm{Tx}} = \gamma_{\mathrm{Rx}} = 0$. Here, the headlight separation 2δ is 1.20 m [138]. Since the Tx vehicle is moving faster than the target vehicle, we assumed that the stopping distance d_{SD} is 6 m [150]. By considering above parameters and applying (6.8) and (6.9), the simulation results are shown in Fig. 6.6. This figure illustrates the contribution of each headlight in addition to the total received power, which is the sum of the LSH and RSH powers.

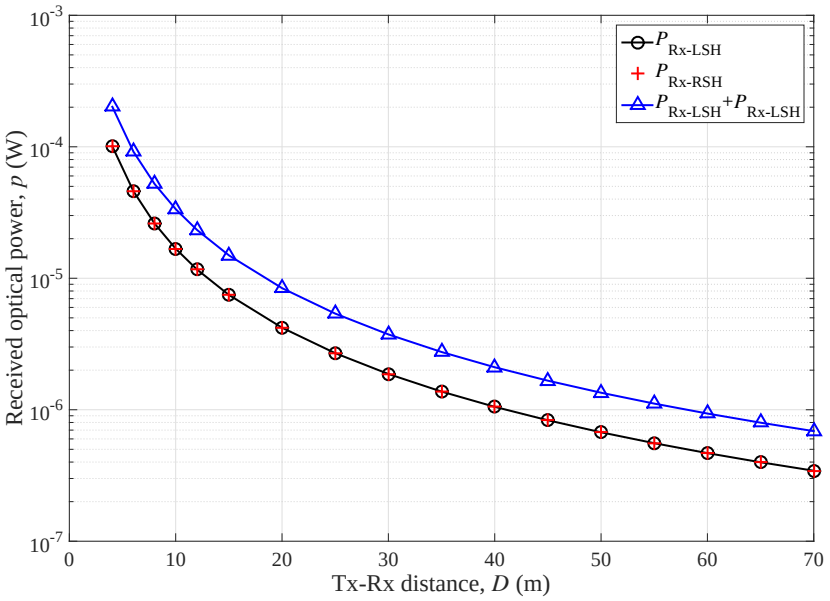

FIGURE 6.6: Received power of LoS components vs. Tx-Rx distance (v_{Tx} = 21.6 km/h, v_{Rx} = 14.4 km/h, $\gamma_{\text{T}} = \gamma_{\text{R}} = 0°$, 2δ = 1.2 m, $\phi_{\text{T}} = 0°$, d_{SD} = 6 m, m=1).

It can be noticed that the received power depends on the Tx-Rx distance and this behaviour becomes more pronounced when the Tx and Rx get closer to each other.

Secondly, since we considered the generalised Lambertian radiation pattern because there is no available standard LEDs headlamp with measured beam pattern, here we examine the effect of mode number m of Lambertian radiation pattern on the received optical power. By taking in to account the total received power from both LSH and RSH, it has been demonstrated that the received power increases as the mode number increase as illustrated in Fig. 6.7. This is due to the fact that higher mode number provides higher directionality of the optical source and hence more power will be delivered.

6.5.1.2 The SB components

As we mentioned before, the VMF distribution is adopted in order to jointly consider the impact of the azimuth and elevation angles on the channel characteristics. Since no measurements available, the main parameters including the mean values of the

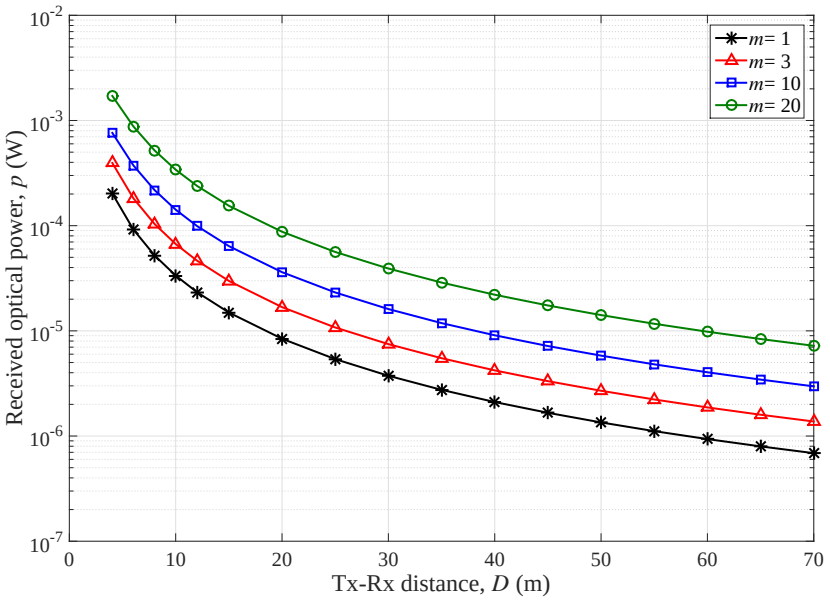

FIGURE 6.7: Received power of LoS components vs. Tx-Rx distance (v_{Tx} = 21.6 km/h, v_{Rx} = 14.4 km/h, $\gamma_{\mathrm{T}} = \gamma_{\mathrm{R}} = 0°$, 2δ = 1.2 m, $\phi_{\mathrm{T}} = 0°$, d_{SD} = 6 m, m=1, 3, 10, 20).

azimuth angles $\alpha_0^{(i)}$ and elevation angles $\beta_0^{(i)}$ $(i = 1, 2, 3)$, as well as the concentration factor k_{c} will be assumed for simulation purposes. Accordingly, the related propagation distances can be determined by using the derived equations that presented in Section 6.3. Here, we tried to make the assumptions as much as close to the reality. Since the effective scatterers are distributed according to VMF distribution, we will investigate and analyse the effect of VMD parameters on the received power, namely, $N^{(i)}$, $k_{\mathrm{c}}^{(i)}$, $\alpha^{(n_i)}$, and $\beta^{(n_i)}$. For the simulation, the user must first choose adequate values for the numbers of discrete scatterers $N^{(i)}$ [52]. Based on our own simulation experiences, a reasonable value for $N^{(i)}$ can be 100. Furthermore, in order to select the set of $\left\{\alpha^{(n_i)}, \beta^{(n_i)}\right\}_{n_i=1}^{N_i}$ we used Method of Equal Volume (MEV), which is proposed in [111] to determine discrete values for the azimuth and elevation angles around the mean direction. In the following subsections, the effect of each parameter on the received power is studied separately for each model.

6.5.1.2.1 Tx-Sphere Model

The received power is related to the concentration factor $k_{\mathrm{c}}^{(i)}$, which is managing the distribution of the scatterers according to VMF distribution. In this work, we

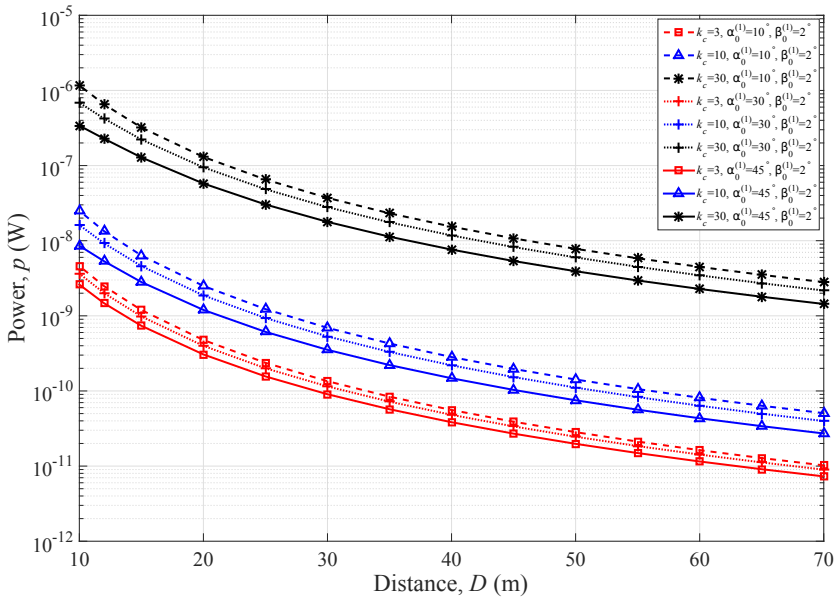

FIGURE 6.8: Received power from LSH within Tx-sphere model ($\gamma_T = \gamma_R = 0°$, $\delta = 0.6$ m, $\phi_{\mathrm{T}} = 0$, $\alpha_0^{(1)} = 10°, 30°, 45°$ $\beta_0^{(1)}, = 2°$, $k_{\mathrm{c}} = 3, 10, 30$).

investigate the effect of $k_{\mathrm{c}}^{(i)}$ and the mean direction of the scatterers on the power amount that can be received from LSH and RSH. Here, the mean direction of the scatterers means, in other words, the position of a car on the adjacent lane. In reality, vehicles are not aligned precisely with other surrounding vehicles that located in the adjacent lanes. Hence, cars which are on the right side make different angles compared with cars on the left side. In order to consider the cars on the left side and right sides, two sets of mean angles have been defined, $\left\{\alpha_0^{(n_i,\mathrm{L})}, \beta_0^{(n_i,\mathrm{L})}\right\}$ and $\left\{\alpha_0^{(n_i,\mathrm{R})}, \beta_0^{(n_i,\mathrm{R})}\right\}$, respectively. Since VVLC technology still at a very early stage of research, there are currently no available measurement data. Therefore, we tried to take in to account the most reliable parameters which are as close to reality as possible. We set the value of the elevation angle to 2° due to the fact that in urban environments, the majority of cars will be saloon cars and hence the reflection from the surrounding cars will be at almost the same plane. On the other hand, the azimuth angles have been set to reliable values as $\alpha_0^{(n_i,\mathrm{L})} = \alpha_0^{(n_i,\mathrm{R})} = 10°, 30°, 45°$. The azimuth angles were chosen to ensure that the most probable positions for the adjacent cars have been taken into account. Furthermore, regarding $k_{\mathrm{c}}^{(i)}$ values, we followed the procedure that applied in conventional RF V2V scenarios in [112], [111]. However, for VVLC, $k_{\mathrm{c}}^{(i)}$ have been

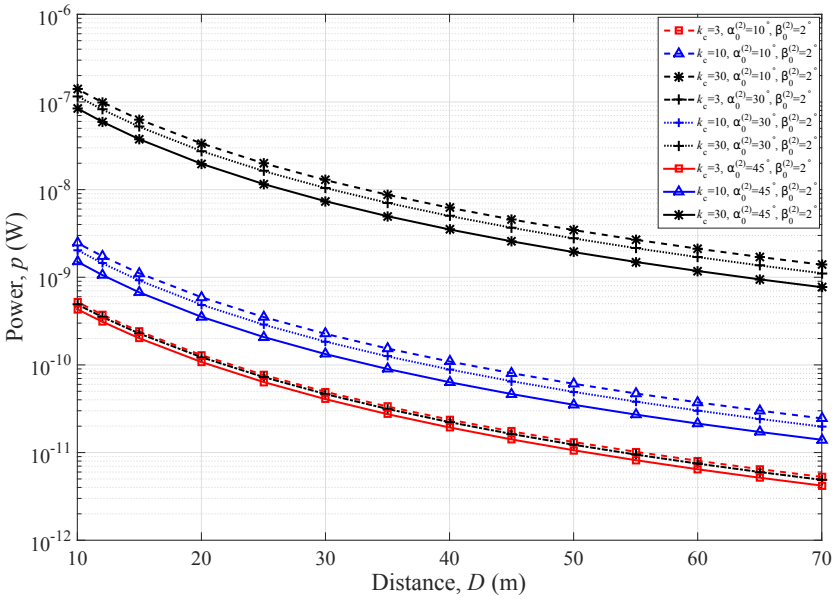

FIGURE 6.9: Received power from LSH within Rx-sphere model ($\gamma_T = \gamma_R = 0°$, $\delta = 0.6$ m, $\phi_{\mathrm{T}} = 0$, $\alpha_0^{(2)} = 10°, 30°, 45°$ $\beta_0^{(2)}, = 2°$, $k_{\mathrm{c}} = 3, 10, 30$).

set to 3, 10, 30. The other parameters which are related to the proposed model are listed in Table 6.3.

Since LSH and RSH present the same behaviour, here only powers which are generated at LSH and reflected off the surrounding vehicles at the left side will be analysed. From Fig. 6.8, it can be noticed that the higher k_{c} results in higher received power since all the scatterers are highly concentrated around the mean angles. On the other hand, when the mean angles increase, the received power decrease. For instance, for $k_{\mathrm{c}} = 30$ the received power from the LSH that reflected off an obstacle located at the left side at distance of 10 m is 1.16×10^{-6} W when the mean angle $\alpha_0^{(1)} = 10°$. While the received power is 3.4×10^{-7} W when $\alpha_0^{(1)} = 45°$ for the same k_{c} value. This is occurred due to the fact that the light intensity falls off as the cosine of the observation angle with respect to the surface normal of the LED and PD.

6.5.1.2.2 Rx-Sphere Model

In terms of Rx-sphere model, the FoV constraint of the PD is considered. Consequently, the assumed mean angles, i.e., $\alpha_0^{(2)}$, and $\beta_0^{(2)}$ must be within PD's FoV Ψ_{FoV}. Simulation results of the received optical power are shown in Fig. 6.9. It has been

found, firstly, that the received powers from the Rx-sphere model are less than their equivalents in Tx-sphere model for different values of k_c, α_0, and β_0. For example, at $k_c = 30$, $\alpha_0^{(2)} = 10°$, and $\beta_0^{(2)} = 2°$, the received power from the Rx-sphere model is 1.4×10^{-7} W compared to 1.16×10^{-6} W from the Tx-sphere model for the same input parameters. Secondly, it can be noticed that when $k_c = 10$, the values of received power are close to each other so that the difference is barely recognisable especially when $\alpha_0^{(2)} = 10°$, and $\alpha_0^{(2)} = 30°$. This is due to the fact that as much as k_c decreases, there will be no dominant mean direction and hence more deviation about the surface normal.

6.5.1.2.3 Elliptic-Cylinder Model

In terms of the elliptic-cylinder model, it is intuitive that less power will be received compared with the two-sphere model. This is due to two main reasons, firstly, the lower reflectivity ρ_{Roadside} of the roadside environments. Secondly, the longer optical path lengths within the elliptic-cylinder model. In this case, the same behaviour which is noticed in the Tx- and Rx-sphere appears here so that higher k_c produces much power at the PD. Fig. 6.10 illustrates the received optical power, which is transmitted from LSH then reflected off the roadside environments to be detected by the PD.

It is worth mentioning that based on simulation results in Figs. 6.8, 6.9, and 6.10, it has been noticed that increasing the number of k_c would not affect the results. This is due to the fact that at higher values of k_c, VMF PDF is more concentrated and hence the angular spread is insignificant.

6.5.2 SNR

Based on noise analysis in 6.4.3, the performance of each component can be analysed through the relationship between the SNR and Tx-Rx distance as illustrated in F.g. 6.11. Here, only the assumption in which $\alpha_0^{(i)} = 10°$, $\beta_0^{(i)} = 2°$, and $k_c = 30$ have been considered for all components. This is due to the fact that these components carrying higher power compared with the others. It can be noticed from Fig. 6.11, that

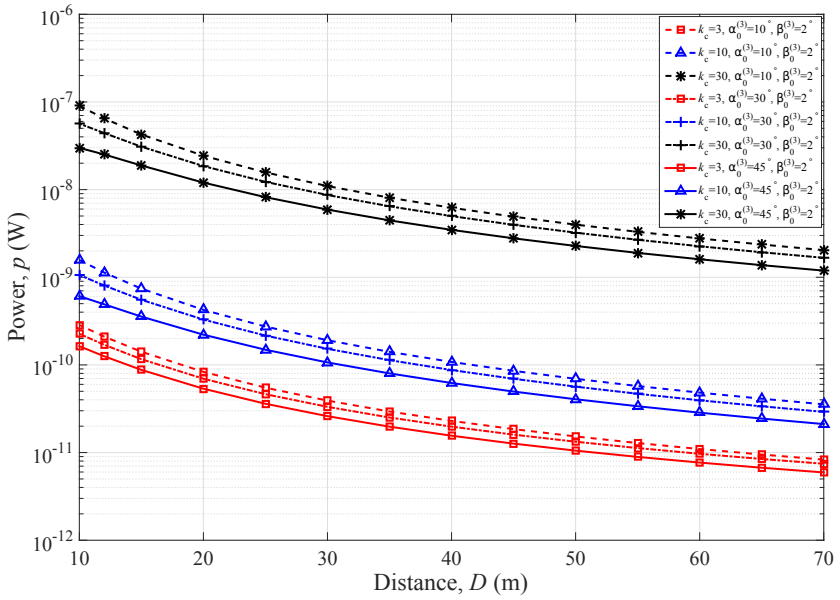

FIGURE 6.10: Received power from LSH within elliptic-cylinder model ($\gamma_T = \gamma_R = 0°$, $\delta = 0.6$ m, $\phi_{\mathrm{T}} = 0$, $\alpha_0^{(3)} = 10°, 30°, 45°$ $\beta_0^{(3)}, = 2°$, $k_{\mathrm{c}} = 3, 10, 30$).

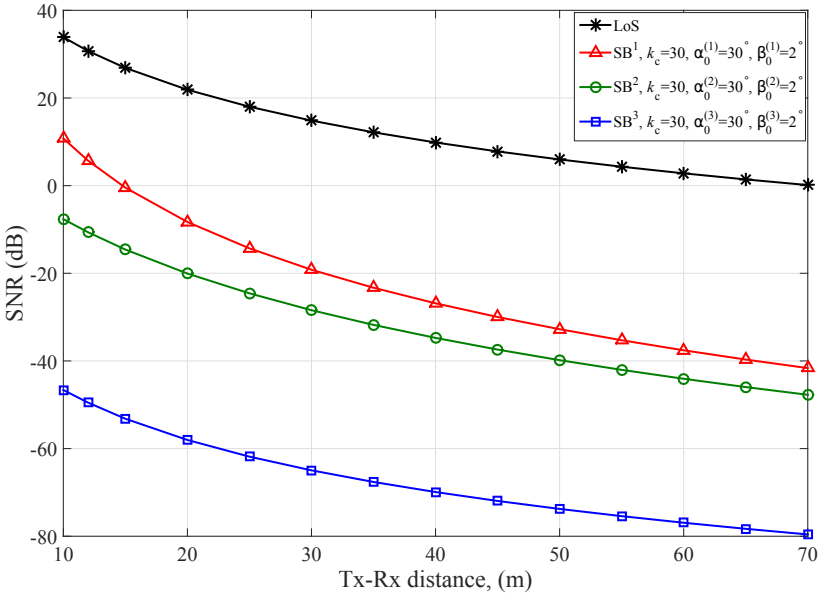

FIGURE 6.11: SNR vs. Tx-Rx distance ($\alpha_0^{(i)} = 10°$, $\beta_0^{(i)}, = 2°, k_{\mathrm{c}} = 30, i = 1, 2, 3$).

SNR values decrease as the Tx-Rx distances increases and the difference in received power according to each component is maintained.

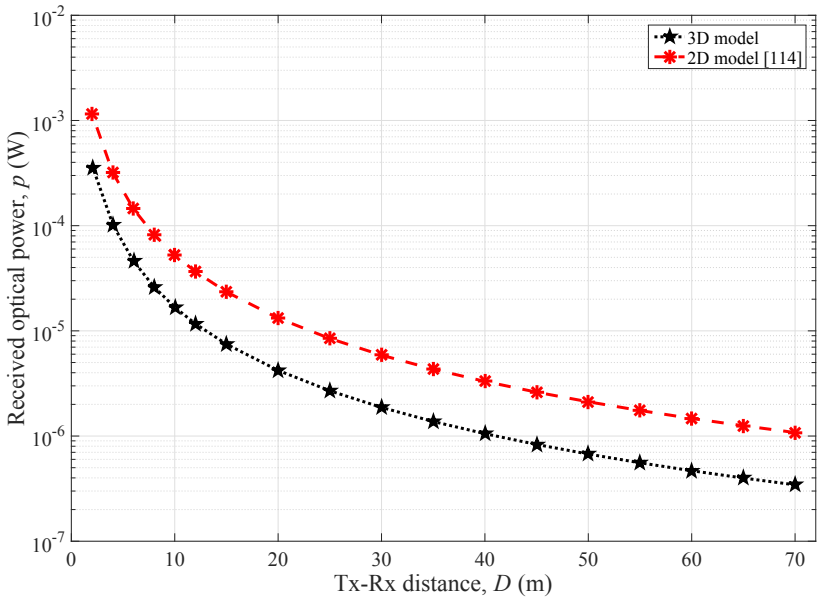

FIGURE 6.12: LoS received power comparison between the 3D and 2D models ($v_{\mathrm{Tx}} = 21.6$ km/h, $v_{\mathrm{Rx}} = 14.4$ km/h, $\gamma_{\mathrm{T}} = \gamma_{\mathrm{R}} = 0°$, $2\delta = 1.2$ m, $\phi_{\mathrm{T}} = 0°$, m=1).

6.5.3 Comparison Between 2D and 3D VVLC RS-GBSM

Regarding the proposed 3D RS-GBSM, it is worth to emphasize that when $\beta^{(n_i)} = 0$, $(i = 1, 2, 3)$, the proposed 3D model will be reduced to a 2D two-ring and elliptic model in [114]. In order to evaluate the impact of elevation angle on the received power, Fig. 6.12 illustrates a comparison between the 3D and 2D models in terms of the received power from LSH. Fig. 6.12 tells that compared with the 3D model, the 2D model overestimates the received power. The reason is that the 2D model assumes that $\beta^{(n_i)}$ has no contribution. Moreover, compared to the 2D model in [114], there is an extra optical path length caused by considering the headlight separation 2δ.

6.6 Summary

As the VVLC applications are at a very early stage, in this chapter, a new 3D mobile RS-GBSM for vehicular VLC MISO channels has been proposed. The proposed model jointly considers the azimuth and elevation angles by using the VMF distribution. VVLC channel characteristics have been examined through a large set of

channel impulse responses generated by the proposed RS-GBSM. Simulation results have shown that for the proposed model the azimuth angle has a significant impact on received power due to the fact that the light intensity falls off as the cosine of the observation angle with respect to the surface normal of the LED and PD. Moreover, the impact of the scatterers' concentrations has been studied. Finally, background noise sources have been modelled and accordingly, system's SNR has been evaluated.

Chapter 7

Conclusions and Future Work

Accurate channel models that are able to mimic key characteristics of optical wireless channels play an important role in designing and testing VLC systems. This thesis has presented a wealth of comprehensive research on optical wireless channel modelling and simulation for indoor and outdoor VLC applications. The novelty and importance of this research have been introduced in details. In this concluding chapter, the key findings of my Ph.D. research are summarised and several potential future research directions are outlined.

7.1 Summary of Results

7.1.1 Indoor VLCs Channel Modelling

In Chapter 2 a comprehensive survey of channel measurement campaigns and models for indoor OWCs, primarily in IR and visible light spectra, has been presented. It has been shown that NDLoS link configuration can be considered as the most suitable link configuration for VLC technology. On the other hand, NDNLoS is considered as the main link design for WUVC and WIRC technologies. Based on our survey, it has been identified that an appropriate channel model for VLC systems is currently missing in the literature. Furthermore, it has been noted that most existing VLC channel models

have extended from WIRC channel models, with the assumption that IR and visible light bands have similar optical properties due to their contiguous wavelengths.

In Chapter 3, we have proposed a new 2D stationary one-ring single-bounce RS-GBSM for VLC SISO Channels. In this model, both of the LoS and SB components have been considered. The impact of the optical path length, AoD/AoA, and the position of the PD on VLC channel characteristics has been studied considering IM/DD scheme. Furthermore, it has been noted that VLC channels are highly correlated at the centre of the environment and the correlation is decreasing gradually when moving away towards the environment edges.

In Chapter 4, a new 2D stationary multiple-bounce RS-GBSM for VLC SISO channels has been proposed. A two-ring and a confocal ellipse have been utilised in this model in order to make it sufficiently generic and adaptable to a variety of indoor scenarios. This is due to the fact that the proposed model has considered the three primary reflections, i.e., SB, DB, and TB in addition to the LoS components. VLC channel characteristics have been studied and analysed with respect to optical path length, AoD/AoA, and the reflection coefficients of the scatterers. Moreover, the utility of the proposed model compared with the existing models has been demonstrated.

7.1.2 Outdoor VLC Channel Modelling

VLC technology considers as an alternative and complementary to the RF wireless communications, not only for indoor applications but could also be used for outdoor applications. Therefore, the potential of using VLC technology in vehicular communications as part of ITS has been proposed lately. For the sake of a VVLC link design and performance evaluation, detailed knowledge about the underlying propagation channel and a corresponding realistic channel model are indispensable. Therefore, VVLC channel modelling and characterising have been considered in Chapter 5 and Chapter 6.

In Chapter 5, a new 2D mobile RS-GBSM for vehicular VLC SISO channels has been proposed. The proposed model has considered SB and DB in addition to the LoS

components. The results show that the received optical power highly depends on the Tx-Rx distance, Rx height, and optical source pattern. For the SB components, it has been demonstrated that the channel gain in dB and the RMS delay spread are following Gaussian distribution. Finally, the results have indicated that the detected optical power from the DB components is low enough to be overlooked.

In Chapter 6, we proposed a novel 3D mobile RS-GBSM for vehicular VLC MISO channels. The proposed RS-GBSM combining two-sphere model and an elliptic-cylinder model. Both LoS and SB components have been considered. The proposed model has the ability to study the impact of the vehicular traffic on the received optical power and jointly considers the azimuth and elevation angles by using VMF distribution. The relationship between the communication range and the received optical power has been investigated considering different scatterers' concentrations k_c. In terms of noise analysis, all background noise sources have been modelled and hence system's SNR has been evaluated.

7.2 Future Research Directions

This section is devoted to discussing important future research directions that can be considered as guidelines for conducting VLC channel measurement campaigns and developing more realistic channel models. Future work includes developing our current research and initiates new research directions as detailed below.

7.2.1 New Communication Scenarios

7.2.1.1 Underground Mining Communications (UMCs)

Most recently, VLCs have been introduced to UMCs landscape. Underground mine environment is one of the world's most hazardous environment since it is composed of tunnels exhibiting risky properties due to the presence of dangerous toxic gas and dust, as well as it is prone to collapse. It is worth mentioning that we have developed

the recursive method to investigate stationary and mobile VLC SISO channel characteristics in two different structures of underground mine environments, i.e., mining roadway and mine working face [151], [152]. However, channel models for more complex underground mining structures need to be developed taking into consideration the reflection coefficients associated with mine floors, walls, and ceilings.

7.2.1.2 Underwater Wireless Communications (UWCs)

UWCs and Underwater Sensor Networks (UWSNs) have been growing steadily towards utilising OWCs. For example, UOWCs enable the establishment of high-speed and reliable links for underwater missions employing robotics or Autonomous Underwater Vehicles (AUVs) [12]. Underwater wireless propagation channels can be seriously affected by marine environments and severe attenuation which turns the underwater wireless channel into one of the most complex and harsh wireless channels in nature [153]. Therefore, channel measurements and models suitable for such hostile environments are worthy being considered as a future research direction.

7.2.1.3 Aviation Environments

The aviation industry is another important area where OWCs can be applied. For WIRC systems, the PL exponent and the standard deviation of shadowing have been determined inside an aircraft cabin for specific scenarios [59]. However, channel measurements and modelling in the visible light spectrum are still of prime importance. This is due to the fact that VLC is a good candidate to connect the passengers to the Internet of Aircraft Things (IoAT) in the modern era of the aviation.

7.2.1.4 Smart Toys Communications

Smart toy networks can be used at homes or entertainment theme parks [154]. They utilize low-cost and energy-efficient LEDs operating in IR and visible light spectra to create interactive communications for toy-to-toy, toy-to-smartphone/computer, and

toy-to-environment. Such technology requires careful channel management in order to keep communication towards the desired end devices or toys.

7.2.1.5 Optical Body Area Network (OBAN)

Transdermal optical communications have become a hot research topic recently due to the rapidly growing usage of implantable medical devices (IMDs) [12], [155]. In order to establish a communication link through a human body, the optical signal need to penetrate the skin layers. However, human skin is a complex biological structure, therefore, characterization of skin optical properties is an extremely challenging task.

7.2.2 VLC MIMO Channel Measurements and Models

MIMO VLC is a promising technology for future OWC networks. This technology has been attracting researchers' attention due to its promising capability of greatly improving link reliability and high spectral efficiency (more bits/s/Hz) compared to IR LAN [20]. A 2×2 MIMO VLC configuration was demonstrated in [156], while a 4×4 configuration was presented in [157]. In this context, it is worth pointing out that for indoor VLC systems with NDLoS, the MIMO VLC channel matrix can be highly correlated because IM/DD has no phase information. Hence, strong correlation prevents reliable decoding of the parallel channels at the receiver [158]. Therefore, reducing the correlation of MIMO VLC channels and obtaining high spatial multiplexing gains are still important topics that need to be addressed in indoor MIMO VLC. On the other hand, in terms of outdoor VLCs, the proposed RS-GBSM for VVLC MISO can be developed to consider MIMO scheme for VVLC channels. This is due to the fact that more Txs and Rxs can be equipped at the front and rear ends of vehicles, respectively. In the same context, more research directions need to be addressed such as weather conditions impact, temperature, multipath interference, SNR, and achievable BER.

7.2.3 Interference Measurements and Models

The SNR in (2.2) is used to evaluate link performance when disturbances are primarily related to noise that generated by the ambient light sources (the sun, fluorescence, etc). On the other hand, Signal to Interference Ratio (SIR) and Signal-to-Interference-plus-Noise Ratio (SINR) are metrics of interest for evaluation of systems in the presence of interference from neighboring transmitters. According to the central limit theorem, the interference should be normally distributed when there are no dominant interferers [159]. However, the directionality in VLC systems often leads to scenarios with dominant interferers. Furthermore, increasing the level of transmitting power is not an option to improve SINR since eye safety regulations will limit the amount of transmitting optical power. In terms of VLC link level, in [160] we have proposed the Light-Cell (Li-Cell) concept, by which we can incorporate visible light spectrum into the cellular system. The simulation results have shown that there is a significant benefit of employing single Li-Cell at and beyond macro cell-edge in terms of per-user average throughput. However, using more Li-Cell units requires an accurate interference model for VLC networks. Hence, it is important to develop accurate interference models in order to study the overall VLC system capacity, energy efficiency, and the throughput.

References

[1] S. Dimitrov and H. Haas, *Principles of LED light communications towards networked Li-Fi*, London: Cambridge University Press, 2015.

[2] C.-X. Wang, F. Haider, X. Gao, X.-H. You, Y. Yang, D. Yuan, H. Aggoune, H. Haas, S. Fletcher, and E. Hepsaydir, "Cellular architecture and key technologies for 5G wireless communication networks," *IEEE Commun. Mag.*, vol. 52, no. 2, pp. 122–130, Feb. 2014.

[3] R. C. Qiu and P. Antonik, *Smart Grid Using Big Data Analytics: A Random Matrix Theory Approach*, West Sussex, John Wiley & Sons, 2017.

[4] S. Wu, *Massive MIMO Channel Modelling for 5G Wireless Communication Systems*, Ph.D. Thesis, Heriot-Watt University, Oct. 2015.

[5] C.-X. Wang, S. Wu, L. Bai, X. You, J. Wang, and C.-L. I, "Recent advances and future challenges for massive MIMO channel measurements and models," *Sci. China Inf. Sci.*, vol. 59, no. 2, pp. 1–16, Feb. 2016.

[6] A. Gupta and R. K. Jha, "A survey of 5G network: Architecture and emerging technologies," *IEEE Access*, vol. 3, pp. 1206–1232, July 2015.

[7] T. S. Rappaport, S. Sun, R. Mayzus, H. Zhao,Y. Azar, K. Wang, G. N. Wong, J. K. Schulz, M. Samimi, and F. Gutierrez, "Millimeter wave mobile communications for 5G cellular: It will work!," *IEEE Access*, vol. 1, pp. 335–349, May 2013.

[8] M. Tilli, T. Motooka, V-M. Airaksinen, S. Franssila, M. Paulasto-Krockel, V. Lindroos, 2nd Ed., *Handbook of Silicon Based MEMS Materials and Technologies*, London: William Andrew, 2015.

[9] R. J. Drost and B. M. Sadler, "Survey of ultraviolet non-line-of-sight communications," *J. Semicond. Sci. Technol.*, vol. 29, no. 8, pp. 1–11, June 2014.

[10] Z. Xu and B. M. Sadler, "Ultraviolet communications: Potential and state-of-the-art," *IEEE Commun. Mag.*, vol. 46, no. 5, pp. 67–73, May 2008.

[11] L. Olof Bjorn, J. Moan, W. Nultsch, A.R. Young, 1st Ed., *Environmental UV Photobiology*, New York: Springer Science, 1993.

[12] Z. Ghassemlooy, L. N. Alves, S. Zvnovec, and M.-A Khalighi, *Visible Light Communications Theory and Applications*, New York: CRC press, 2017.

[13] M. S. Islim *et al.*, "Towards 10 Gb/s orthogonal frequency division multiplexing-based visible light communication using a GaN violet microLED," *Photonics Research*, vol. 5, no. 2, A35, Apr. 2017.

[14] R. Lenk, C. Lenk, 2nd Ed., *Practical Lighting Design with LEDs*, New York: John Wiley & Sons, 2017.

[15] World Health Orginization, "IARC Classifies Radio frequency Electromagnetic Fields as Possibly Carcinogenic to Humans" [Online]. Available: http://www.iarc.fr/en/media-centre/pr/2011/pdfs/pr208_E.pdf [Accessed Jan. 28, 2018].

[16] F. R. Gfeller and U. H. Bapst, "Wireless in-house data communication via diffuse infrared radiation," in *Proc. IEEE*, vol. 67, no. 11, pp. 1474–1486, Nov. 1979.

[17] United States Department of Energy, "Energy Savings Forecast of Solid-State Lighting in General Illumination Applications" [Online]. Available: http://energy.gov/eere/ssl/downloads/solid-state-lighting-2016-rd-plan [Accessed Jan. 28, 2018].

[18] P. H. Pathak, X. Feng, P. Hu, and P. Mohapatra, "Visible light communication, networking, and sensing: A survey, potential and challenges," *IEEE Commun. Surveys Tuts.*, vol. 17, no. 4, pp. 2047–2077, 4th Quart., 2015.

[19] N. Sklavos, M. Huebner, D. Goehringer and P. Kitsos, *System-Level Design Methodologies for Telecommunication*, London: Springer, 2014.

[20] Z. Ghassemlooy, W. Popoola, and S. Rajbhandari, 1st Ed., *Optical Wireless Communications: System and Channel Modelling with MATLAB*, New York: CRC press, 2013.

[21] M. A. Khalighi and M. Uysal, "Survey on free space optical communication: A communication theory perspective," *IEEE Commun. Surveys Tuts*, vol. 16, no. 4, pp. 2231–2258, 2014.

[22] H. Kroemer, "The double-heterostructure concept: How it got started," in *Proc. IEEE*, vol. 101, no. 10, pp. 2183–2187, Oct. 2013.

[23] G. Held, *Introduction to Light Emitting Diode Technology and Applications*, New York: CRC press, 2009.

[24] M. N. Khan, *Understanding LED Illumination*, New York: CRC Press, 2014.

[25] Y. Tanaka, S. Haruyama and M. Nakagawa, "Wireless optical transmissions with white colored LED for wireless home links," in *Proc. IEEE PIMRC'00*, London, UK, 2000, pp. 1325–1329.

[26] Visible Light Communication Consortium (VLCC) [Online]. Available: http://www.vlcc.net [Accessed Jan. 28, 2018].

[27] *IEEE Standard for Local and Metropolitan Area Networks-Part 15.7: Short-Range Wireless Optical Communication Using Visible Light*, IEEE Std. 802.15.7, Sept. 2011.

[28] PureLiFi [Online]. Available: http://www.purelifi.com [Accessed Jan. 25, 2018].

[29] R. V. Priyan, S. Dinesh, J. Ilanthendral and B. Ramya, "Communication system for underground mines using Li-Fi 5G technology," *IJLTEMAS'14*, vol. 3, no. 9, pp. 80–85, Sept. 2014.

[30] Visible Light Communications Association (2015, Oct.) Current Status of IEEE 802.15.7 r1 OWC Standardization [Online]. Available: http://www.vlca.net [Accessed Jan. 28, 2018].

[31] H. Ding, G. Chen, A. K. Majumdar, B. M. Sadler, and Z. Xu, "Modeling of non-line-of-sight ultraviolet scattering channels for communication," *IEEE J. Sel. Areas Commun.*, vol. 27, no. 9, pp. 1535–1544, Dec. 2009.

[32] Z. Xu, G. Chen, F. Abou-Galala, and M. Leonardi, "Experimental performance evaluation of non-line-of-sight ultraviolet communication systems," *Optical Engineering Journal*, vol. 6709, pp. 67090Y.1–67090Y.12, Sept. 2007.

[33] G. A. Shaw, A. M. Siegel, and J. Model, "Extending the range and performance of non-line-of-sight ultraviolet communication links," *Optical Engineering Journal*, vol. 6231, pp. 62310C.1–62310C.12, May 2006.

[34] FSONA [Online]. Available: http://www.fsona.com [Accessed Jan. 28, 2018].

[35] J. R. Barry, *Wireless Infrared Communications*, New York: Springer, 1994.

[36] J. M. Kahn and J. R. Barry, "Wireless infrared communications," in *Proc. IEEE*, vol. 85, pp. 265–298, Feb. 1997.

[37] Z. Ghassemlooy, "Indoor Optical Wireless Communications Systems-Part I: Review," School of Engineering, Northumbria University, Newcastle upon Tyne, UK, 2003.

[38] D. Wu, Z. Ghassemlooy, H. L. Minh, S. Rajbhandari, M. A. Khalighi, and X. Tang, "Optimisation of Lambertian order for non-directed optical wireless communication," in *Proc. IEEE ICCC'12*, Beijing, China, Aug. 2012, pp. 1–6.

[39] O. Bouchet, *Wireless Optical Communications*, London: John Wiley & Sons, 2012.

[40] Y. A. Alqudah and M. Kavehrad, "MIMO characterization of indoor wireless optical link using a diffuse-transmission conguration," *IEEE Trans. Commun.*, vol. 51, no. 9, pp. 1554–1560, Sept. 2003.

[41] J. M. Kahn, W. J. Krause and J. B. Carruthers, "Experimental characterization of non-directed indoor infrared channels," *IEEE Trans. Commun.*, vol. 43, no. 2, pp. 1613–1623, Feb. 1995.

[42] D. P. Young, J. Brewer, J. Chang, T. Chou, J. Kvam and M. Pugh, "Diffuse mid-UV communication in the presence of obscurants," in *Proc. ASILOMAR'12*, Pacific Grove, USA, 2012, pp. 1061–1064.

[43] R. Ramirez-Iniguez, S. M. Idrus and, Z. Sun, *Optical Wireless Communications: IR for Wireless Connectivity*, New York: CRC Press, 2008.

[44] V. Jungnickel, V. Pohl, S. Nonnig, and C. V. Helmolt, "A physical model of the wireless infrared communication channel," *IEEE J. Sel. Areas Commun.*, vol. 20, no. 3, pp. 631–640, Apr. 2002.

[45] D. R. Wisely, "A 1 Gbit/s optical wireless tracked architecture for ATM delivery," *IEE Colloquium on Optical Free Space Communication Links*, London, UK 1996, pp. 14/1–14/7.

[46] K. K. Wong, T. O'Farrell and M. Kiatweerasakul, "The performance of optical wireless OOK, 2-PPM and spread spectrum under the effects of multipath dispersion and articial light interference," *Int. J. Commun. Syst.*, vol. 13, pp. 551–576, Nov. 2000.

[47] H. Elgala, R. Mesleh, and H. Haas, "Practical considerations for indoor wireless optical system implementation using OFDM," in *Proc. ConTEL'09*, Zagreb, Croatia, June 2009, pp. 25–29.

[48] H. Kaushal and G. Kaddoum, "Underwater optical wireless communication," *IEEE Access*, vol. 4, pp. 1518–1547, 2016.

[49] H. Sasaoka, *Mobile Communications*, Tokyo: IOS Press, 1997.

[50] G. Wu and J. Zhang, "Demonstration of a visible light communication system for underground mining applications," in *Proc. IECT'16*, Shanghai, China, June 2016, pp. 1–7.

[51] F. J. López-Hernández, R. Pérez-Jiménez, and A. Santamaria, "Ray-tracing algorithms for fast calculation of the channel impulse response on diffuse IR wireless indoor channels," *Optical Engineering Journal*, vol. 39, no. 10, pp. 2775–2780, Oct. 2000.

[52] M. Pätzold, 2nd Ed., *Mobile Radio Channels*, Chichester: John Wiley & Sons, 2012.

[53] M. D. A. Mohamed and S. Hranilovic, "Optical impulse modulation for indoor diffuse wireless communications," *IEEE Trans. Commun.*, vol. 57, no. 2, pp. 499–508, Feb. 2009.

[54] D. Wu, Z. Ghassemlooy, S. Rajbhandari, and H. Le Minh, "Improvement of the transmission bandwidth for indoor optical wireless communication systems using a diffused Gaussian beam," *IEEE Commun. Lett.*, vol. 16, no. 8, pp. 1316–1319, Aug. 2012.

[55] J. Grubor, S. Randel, K.-D. Langer, and J. W. Walewsk, "Broadband information broadcasting using LED-based interior lighting," *Journal of Lightwave Technology*, vol. 26, pp. 3883–3892, Dec. 2008.

[56] X. Zhang, K. Cui, M. Yao, H. Zhang, and Z. Xu, "Experimental characterization of indoor visible light communication channels," in *Proc. IEEE CSNDSP'12*, Poznan, Poland, July 2012, pp. 1–5.

[57] J. R. Barry, J. M. Kahn, W. J. Krause, E. A. Lee, and D. G. Messerschmitt, "Simulation of multipath impulse response for indoor wireless optical channels," *IEEE J. Sel. Areas Commun.*, vol. 11, no. 3, pp. 367–379, Apr. 1993.

[58] F. Miramirkhani, O. Narmanlioglu, M. Uysal, and E. Panayirci, "A mobile channel model for VLC and application to adaptive system design," *IEEE Commun. Lett.*, vol. 21, no. 5, pp. 1035–1038, May. 2017.

[59] S. Dimitrov, R. Mesleh, H. Haas, M. Cappitelli, M. Olbert, and E. Bassow, "Path loss simulation of an infrared optical wireless system for aircrafts," in *Proc. IEEE Globecom'09*, Honolulu, USA, Dec. 2009, pp. 1–6.

[60] Y. Xiang, M. Zhang, M. Kavehrad, M. I. S. Chowdhury, M.-M. Liu, J. Wu, and X. Tanga, "Human shadowing effect on indoor visible light communications channel characteristics," *Optical Engineering Journal*, vol. 53, no. 8, pp. 086113–086113, Aug. 2014.

[61] S. Jivkova and M. Kavehrad, "Shadowing and blockage in indoor optical wireless communications," in *Proc. IEEE Globecom'03*, San Francisco, CA, USA, Dec. 2003, pp. 3269–3273.

[62] M. R. Pakravan, M. Kavehrad, and H. Hashemi, "Indoor wireless infrared channel characterization by measurements," *IEEE Trans. Veh. Technol.*, vol. 50, no. 4, pp. 1053–1073, July 2001.

[63] K. -R. Sohn and M. -S. Kim, "LED transceivers with beehive-shaped reflector for visible light communication," *JKOSME*, vol. 38, no. 2, pp. 169–174, 2014.

[64] R. J. Drost, T. J. Moore, and B. M. Sadler, "UV communications channel modeling incorporating multiple scattering interactions," *JOSA A*, vol. 24, no. 4, pp. 686–695, Apr. 2011.

[65] R. Yuan and J. Ma, "Review of ultraviolet non-line-of-sight communication," *China Communications*, vol. 13, no. 6, pp. 63–75, June 2016.

[66] N. Hayasaka and T. Ito, "Channel modeling of nondirected wireless infrared indoor diffuse link," *Electronics and Communications in Japan*, vol. 90, no. 6, pp. 10–19, 2007.

[67] F. J. López-Hernández and M. J. Betancor, "DUSTIN: Algorithm for calculation of impulse response on IR wireless indoor channels," *IEEE Electronic. Lett.*, vol. 33, no. 21, pp. 1804–1806, 1997.

[68] H. Hashemi, G. Yun, M. Kavehrad, and F. Behbahani, "Frequency response measurements of the wireless indoor channel at infrared frequencies," in *Proc. IEEE ICCC'94*, New Orleans, USA, 1994, pp. 1511–1515.

[69] R. Pérez-Jiménez, J. Berges, and M. J. Betancor, "Statistical model for the impulse response on infrared indoor diffuse channels," *IEEE Electronic. Lett.*, vol. 33, no. 15, pp. 1298–1300, July 1997.

[70] H. Hashemi, "The indoor radio propagation channel," in *Proc. IEEE*, vol. 81, no. 7, pp. 943–968, July 1993.

[71] G. W. Marsh and J. M. Kahn, "Performance evaluation of experimental 50-Mb/s diffuse infrared wireless link using on-off keying with decision-feedback equalization," *IEEE Trans. Commun.*, vol. 44, no. 11, pp. 1496–1504, Nov. 1996.

[72] Samsung Electronics. (2008, July). VLC channel measurement in indoor applications [Online]. Available: https://mentor.ieee.org/802.15/dcn/08/15-08-0436-00-0vlc-vlc-channelmeasurement-for-indoor-application.pdf [Accessed Jan. 28, 2018].

[73] K. Cui, G. Chen, Z. Xu and R. D. Roberts, "Line-of-sight visible light communication system design and demonstration," in *Proc. IEEE CSNDSP'10*, Newcastle, UK, 2010, pp. 621–625.

[74] J.B. Carruthers and P. Kannan, "Iterative site-based modeling for wireless infrared channels," *IEEE Trans. on Antennas and Propagation*, vol. 50, no. 5, pp. 759–765, May 2002.

[75] P. Chvojka, S. Zvanovec, P. A. Haigh, and Z. Ghassemlooy, "Channel characteristics of visible light communications within dynamic indoor environment," *Journal of Lightwave Technology*, vol. 33, no. 9, pp. 1719–1725, May 2015.

[76] H. Hashemi, G. Yun, M. Kavehrad, F. Behbahani, and P. Galko, "Indoor propagation measurements at infrared frequencies for wireless local area networks

applications," *IEEE Trans. Veh. Technol.*, vol. 43, no. 3, pp. 562–576, 1994 Aug. 1994.

[77] F. J. López-Hernández, R. Pérez-Jiménez, and A. Santamaria, "Monte Carlo calculation of impulse response on diffuse IR wireless indoor channels," *IEEE Electronic. Lett.*, vol. 34, no. 12, pp. 1260–1262, June 1998.

[78] K. Smitha, A. Sivabalan, and J. John, "Estimation of channel impulse response using modified ceiling bounce model in non-directed indoor optical wireless systems," *Wireless Personal Commun.*, vol. 45, no. 1, pp. 1–10, Apr. 2008.

[79] E. Sarbazi, M. Uysal, M. Abdallah, and K. Qaraqe, "Ray tracing based channel modeling for visible light communications," in *Proc. SPCA'14*, Trabzon, Turkey, Apr. 2014, pp. 23–25.

[80] A. Al-Kinani, C.-X. Wang, H. Haas, and Y. Yang, "A geometry-based multiple bounce model for visible light communication channels," in *Proc. IWCMC'16*, Paphos, Cyprus, Sept. 2016, pp. 31–37.

[81] S. J. Lee, J. K. Kwon, S. Y. Jung, and Y. H. Kwon, "Simulation modelling of visible light communication channel for automotive applications," in *Proc. IEEE ITSC'12*, Anchorage, USA, Sep. 2012, pp. 463–468.

[82] M. Uysal, C. Capsoni, Z. Ghassemlooy, A. Boucouvalas, and E. Udvary, *Optical Wireless Communications: An Emerging Technology*, Switzerland: Springer, 2016.

[83] J. B. Carruthers and J. M. Kahn, "Modeling of nondirected wireless infrared channels," *IEEE Trans. Commun.*, vol. 45, no. 10, pp. 1260–1268, Oct. 1997.

[84] K. Smitha A. Sivabalan, and J. John, "Modified ceiling bounce model for computing path loss and delay spread in indoor optical wireless systems," *IJCNS*, vol. 2, no. 8, pp. 754–758, Nov. 2009.

[85] T. Komine and M. Nakagawa, "Integrated system of white LED visible-light communication and power-line communication," *IEEE Trans. on Consumer Electronics.*, vol. 49, no. 1, pp. 71–79, Feb. 2003.

[86] T. Komine and M. Nakagawa, "Fundamental analysis for visible-light communication system using LED lights," *IEEE Trans. on Consumer Electronics.*, vol. 50, no. 1, pp. 100–107, Feb. 2004.

[87] Z. Wang and S. Chen, "Grouped DFT precoding for PAPR reduction in visible light OFDM systems," *Int. J. of Electronics Communication and Computer Engineering*, vol. 6, no. 6, pp. 710–713, 2015.

[88] M. D. Higgins, R. J. Green, and M. S. Leeson, "Optical wireless for intravehicle communications: Incorporating passenger presence scenarios," *IEEE Trans. Veh. Technol.*, vol. 62, no. 8, pp. 3510–3517, Oct. 2013.

[89] F. J. López-Hernández, R. Pérez-Jiménez, and A. Santamaria, "Modified Monte Carlo scheme for high-efficiency simulation of the impulse response on diffuse IR wireless indoor channels," *IEEE Electronic. Lett.*, vol. 34, no. 19, pp. 1819–1820, Sept. 1998.

[90] D.-Q. Ding and X.-Z. Ke, "A new indoor VLC channel model based of reflection," *Optoelectronics Lett.*, vol. 6, no. 4, pp. 295–298, July 2010.

[91] V. Pohl, V. Jungnickel, and C. von Helmolt, "Integrating-sphere diffuser for wireless infrared communication," *IEE Colloquium on Optical Wireless Communications*, London, UK, 1999, pp. 4/1–4/6.

[92] J. Ding, K. Wang, and Z. Xu, "Accuracy analysis of different modeling schemes in indoor visible light communications with distributed array sources," in *Proc. IEEE CSNDSP'14*, Manchester, UK, July 2014, pp. 1005–1010.

[93] S.-I. Choi, "Analysis of VLC channel based on the shapes of white-light LED lighting," in *Proc. IEEE ICUFN'12*, Phuket, Thailand, 2012, pp. 1–5.

[94] J. B. Carruthers and S. M. Carroll, "Statistical impulse response models for indoor optical wireless channels," *International J. Commun. Systems*, vol. 18, pp. 267–284, Apr. 2005.

[95] A. Al-Kinani, C.-X. Wang, H. Haas, and Y. Yang, "Characterization and modeling of visible light communication channels," in *Proc. IEEE VTC'16*, Nanjing, China, May 2016, pp. 1–5.

[96] F. Miramirkhani and M. Uysal, "Channel modeling and characterization for visible light communications," *IEEE Photonics Journal*, vol. 7, no. 6, pp. 1–16, Dec. 2015.

[97] J. B. Carruthers, "Wireless infrared communications," *Wiley Encyclopedia of Telecommunications*, vol. 27, no. 9, pp. 1–10, 2002.

[98] T. Komine, J. H. Lee, S. Haruyama, and M. Nakagawa, "Adaptive equalization system for visible light wireless communication utilizing multiple white LED lighting equipment," *IEEE Trans. Commun.*, vol. 8, no. 6, pp. 2892–2900, June 2009.

[99] G. Ren, S. He, and Y. Yang, "An improved recursive channel model for indoor visible light communication systems," *Information Technology Journal*, vol. 12, no. 2, pp. 1245–1250, Apr. 2013.

[100] K. Lee, H. Park, and J. Barry, "Indoor channel characteristics for visible light communications," in *IEEE Commun. Lett.*, vol. 15, no. 2, pp. 217–219, Feb. 2011.

[101] A. Sivabalan and J. John, "Modeling and simulation of indoor optical wireless channels: a review," in *Proc. TENCON'03*, Bangalore, India, Oct. 2003, pp. 1082–1085.

[102] W. Wiesbeck, "The mobile to mobile (C2C) communication channel," in *Proc. IEEE EuCAP'07*, Edinburgh, UK, 2007, pp. 1–1.

[103] W. R. McCluney, 2nd Ed., *Introduction to Radiometry and Photometry*, Boston: Artech House, 2014.

[104] V. Pohl, V. Jungnickel, and C. von Helmolt, "A channel model for wireless infrared communication," in *Proc. IEEE PIMRC'00*, London, UK, 2000, pp. 297–303.

[105] Zemax [Online]. Available: http://www.radiantzemax.com [Accessed Jan. 28, 2018].

[106] E. Sarbazi, M. Uysal, M. Abdallah, and K. Qaraqe, "Indoor channel modelling and characterization for visible light communications," in *Proc. ICTON'14*, Graz, Austria, July 2014, pp. 1–4.

[107] R. Ulbricht, *Das Kugelphotometer*, Berlin: R. Oldenbourg Verlag, 1920.

[108] J. B. Carruthers and P. Kannan. *IrSimIt* [Online]. Available: http://iss.bu.edu/bwc/irsimit [Accessed Jan. 28, 2018].

[109] S. M. Carroll, "Modeling Wireless Infrared Communications for Network Simulation," Ph.D. Dissertation, Boston University, Boston, 2004.

[110] X. Cheng, C.-X. Wang, D. I. Laurenson, S. Salous, and A. V. Vasilakos, "An adaptive geometry-based stochastic model for non-isotropic MIMO mobile-to-mobile channels," *IEEE Trans. Wireless Commun.*, vol. 8, no. 9, pp. 4824–4835, Sept. 2009.

[111] Y. Yuan, C. -X. Wang, X. Cheng, B. Ai, and D. I. Laurenson, "Novel 3D geometry-based stochastic models for non-isotropic MIMO vehicle-to-vehicle channels," *IEEE Trans. Wireless Commun.*, vol. 13, no. 1, pp. 298–309, Jan. 2014.

[112] X. Cheng, C.-X. Wang, Y. Yuan, D. I. Laurenson, and X. Ge, "A novel 3D regular-shaped geometry-based stochastic model for non-isotropic MIMO mobile-to-mobile channels," in *Proc. IEEE VTC'10-Fall*, Ottawa, Canada, Sept. 2010, pp. 1–5.

[113] A. Al-Kinani, C.-X. Wang, and H. Haas, "A novel 3D GBSM for indoor visible light communication channels,". Under final revision of co-authors, planned to be submitted in *IEEE Trans. Commun.*

[114] A. Al-Kinani, J. Sun, C.-X. Wang, W. Zhang, X. Ge, and H. Haas, "A 2D non-stationary GBSM for vehicular visible light communication channels," submitted for publication in *IEEE Trans. Wireless Commun.* Manuscript first submitted Nov. 20, 2017, accepted with major revisions, Feb. 9, 2018.

[115] A. Al-Kinani, C.-X. Wang, Q. Zhu, J. Sun, W. Zhang, and H. Haas, "A 3D non-stationary GBSM for vehicular visible light communication MISO channels," to be submitted in *IEEE Trans. Vehi. Technol.*

[116] M. Zhang, Y. Zhang, X. Yuan, and J. Zhang, "Mathematic models for a ray tracing method and its applications in wireless optical communications," in *Optical Express*, vol. 18, no. 17, pp. 18431–18437, Aug. 2010.

[117] S. R. Pérez, R. P. Jiménez, F. J. López Hernández, O. B. González Hernández, and A. J. Ayala Alfonso, "Reflection model for calculation of the impulse response on IR-wireless indoor channels using ray-tracing algorithm ," *Microwave and Optical Technology Letters*, vol. 32, no. 4, pp. 296–300, Feb. 2002.

[118] B. T. Phong, "Illumination for computer generated pictures," *CACM*, vol. 18, no. 6, pp. 311–317, June 1975.

[119] D. R. Biosca, P. López, and L. Jorge, "Generalization of Monte Carlo ray-tracing algorithm for the calculation of the impulse response on indoor wireless infrared channels," *Universidad, Cienciay Tecnología*, 2005.

[120] F. Miramirkhani, M. Uysal, and E. Panayircib, "Novel channel models for visible light communications," *Optical Engineering Journal*, vol. 9387, pp. 93870Q.1–93870Q.13, Feb. 2015.

[121] T. Yoshizawa, 2nd Ed., *Handbook of Optical Metrology: Principles and Applications*, New York: CRC press, 2015.

[122] D. S. Shiu, G. J. Foschini, M. J. Gans, and J. M. Kahn, "Fading correlation and its effects on the capacity of multielement antenna systems," *IEEE Trans. Commun.*, vol. 48, no. 3, pp. 502–513, Mar. 2000.

[123] www.hebeiltd.com.cn (model S12NW6C) [Accessed Jan. 31, 2018].

[124] J. Grubor, O.C. Gaete Jamett, J.W. Walewski, S. Randel, and K.-D. Langer, "High-speed wireless indoor communication via visible light," in *Proc. ITG'07*, Berlin, Germany, March 2007.

[125] DIALux [Online]. Available: http:// www.dial.de [Accessed Jan. 28, 2018].

[126] X. Cheng, C.-X. Wang, H. Wang, X. Gao, X.-H. You, D. Yuan, B. Ai, Q. Huo, L. Song, and B. Jiao, "Cooperative MIMO channel modeling and multi-link spatial correlation properties," *IEEE J. Sel. Areas Commun.*, vol. 30, no. 2, pp. 388–396, Feb. 2012.

[127] E. W. Weisstein, 2nd Ed., *CRC Concise Encyclopedia of Mathematics*, New York: CRC press, 2003.

[128] Annual Global Road Crash Statistics [Online]. Available: http:// www.asirt.org/initiatives/informing-road-users/road-safety-facts/road-crash-statistics [Accessed Jan. 28, 2018].

[129] World Health Orginization, [Online]. Available: http://www.who.int/mediacentre/factsheets/fs358/en [Accessed Jan. 28, 2018].

[130] S, Zeadally, R. Hunt, Y.-S. Chen, A. Irwin, and A. Hassan, "Vehicular ad hoc networks (VANETS): status, results, and challenges," *Telecommun. Syst.*, vol. 50, no. 4, pp. 217–241, August 2012.

[131] M. Uysal, C. Capsoni, Z. Ghassemlooy, A. Boucouvalas, and E. Udvary, *Optical Wireless Communications: An Emerging Technology*, Bern: Springer, 2016.

[132] European Commission, "Daytime running light," [Online]. Available: https://ec.europa.eu/commission/index_en [Accessed Jan. 28, 2018].

[133] I. Knight, B. Sexton, R. Bartlett, T. Barlow, S. Latham, I. Mccrae. (2007, Jan.). Daytime Running Lights (DRL): A review of the reports from the European Commission [Online]. Available: http:// www.gov.uk/government/organisations/department-for-transport [Accessed Jan. 28, 2018].

[134] M. Wada, T. Yendo, T. Fujii, and M. Tanimoto, "Road-to-vehicle communication using LED traffic light," in *Proc. IEEE Intelligent Vehicles Symposium*, Nevada, USA, June 2005, pp. 601–606.

[135] K. Cui, G. Chen, Z. Xu, and R. D. Roberts, "Experimental characterization of traffic light to vehicle VLC link performance," in *Proc. IEEE Globecom'11*, Houston, USA, 2011, pp. 808–812.

[136] S. Iwasaki, C. Premachandra, T. Endo, T. Fujii, M. Tanimoto, and Y. Kimura, "Visible light road-to-vehicle communication using high-speed camera," in *Proc. IEEE Intell. Veh. Symp.*, Eindhoven, The Netherlands, Jun. 2008, pp. 13–18.

[137] S. J. Lee, J. K. Kwon, S. Y. Jung, and Y. H. Kwon, "Evaluation of visible light communication channel delay profiles for automotive applications," *EURASIP J. Wireless Commun. Networking*, vol. 370, pp. 1–8, 2012.

[138] P. Luo, Z. Ghassemlooy, H.- L. Minh, E. Bentley, A, Burton, and X. Tang, "Performance analysis of a car-to-car visible light communication system," *Appl. Opt.* vol. 54, no. 7, pp. 1696–1706, March 2015.

[139] P. Luo, Z. Ghassemlooy, H. Le Minh, E. Bentley, A. Burton, and X. Tang, "Fundamental analysis of a car to car visible light communication system," in *Proc. IEEE CSNDSP'14*, Manchester, UK, 2014, pp. 1011–1016.

[140] Transport Canberra and City Services. (2016, Mar.). Design standards for urban infrastructure [Online]. Available: https://www.tccs.act.gov.au/ [Accessed Feb. 5, 2018].

[141] Alta Planning and Design. (2017, Jan.). Urban, Rural and Suburban Complete Streets Design Manual [Online]. Available: https://www.northamptonma.gov/DocumentCenter/View/6668 [Accessed Feb. 5, 2018].

[142] M. Fabian, E. Lewis, T. Newe, and S. Lochmann, "Optical fibre cavity for ring-down experiments with low coupling losses," *Meas. Sci. Technol.*, vol. 21, pp. 1–5, July 2010.

[143] M. L. Marceau and M. G. VanGeem. (2008, Aug.). Solar Reflectance Values of Concrete [Online]. Available: http://www.cement.org/docs/default-source/fc_concrete_technology/sn2982a-solar-reflectance-values-of-concrete.pdf [Accessed Feb. 5, 2018].

[144] B. Schoettle and M. J. Flannagan, "A Market-Weighted Description of Low-Beam and High-Beam Headlighting Patterns in the U.S.," University of Michigan, Michigan U.S.A. Rep.UMTRI-2004-23, 2004.

[145] B. M. Ayyub and R.H. McCuen, 1st Ed., *Probability, Statistics & Reliability for Engineers*, Boca Raton: CRC Press, 1997.

[146] Y. Yuan, C.-X. Wang, Y. He, M. M. Alwakeel, and H. Aggoune, "3D wideband non-stationary geometry-based stochastic models for non-isotropic MIMO vehicle-to-vehicle channels," *Proc. IEEE Trans. Wireless Commun.*, vol. 14, no. 12, pp. 6883–6895, Dec. 2015.

[147] D. Hynd, M. McCarthy, J. Carroll, M. Seidl, M. Edwards, C. Visvikis, M. Tress, N. Reed, and A. Stevens, "Benefit and feasibility of a range of new technologies and unregulated measures in the fields of vehicle occupant safety and protection of vulnerable road users," European Commission, Brussels, Belgium, 2015.

[148] J. L. Lindsey, 2nd Ed, *Applied Illumination Engineering*, Lilburn: Fairmont Press, 1997.

[149] K. V. Mardia and P. E. Jupp, *Directional Statistics*. London: John Wiley & Sons, 2000.

[150] Department for Transport. (2007, Jan.). Speed, Speed Limits and Stopping Distances [Online]. Available: http://www.brake.org.uk/rsw/15-facts-a-resources/facts/1255-speed [Accessed Feb. 5, 2018].

[151] J. Wang, A. Al-Kinani, W. Zhang, and C.-X. Wang, "A new VLC channel model for underground mining environments," in *Proc. IWCMC'17*, Valencia, Spain, June 2017, pp. 2134–2139.

[152] J. Wang, A. Al-Kinani, J. Sun, W. Zhang, and C.-X. Wang, "A path loss channel model for visible light communications in underground mines," in *Proc. IEEE ICCC'17*, Qingdao, China, Oct. 2017, accepted for publication at Aug. 3, 2017.

[153] X. Zhang, J. H. Cui, S. Das, M. Gerla and M. Chitre, "Guest Editorial: Underwater wireless communications and networks: theory and application: Part 1," *IEEE Commun. Mag.*, vol. 53, no. 11, Nov. 2015, pp. 40–41.

[154] G. Corbellini, K. Aksit, S. Schmid, S. Mangold, and T. R. Gross, "Connecting networks of toys and smartphones with visible light communication," *IEEE Commun. Mag.*, vol. 52, no. 7, pp. 72–78, July 2014.

[155] D. R. Dhatchayeny, W. A. Cahyadi, S. R. Teli, and Y.-H. Chung, "A novel optical body area network for transmission of multiple patient vital signs,.

[156] I.-C. Lu and Y.-L. Liu, and C.-H. Lai, "High-speed 2 × 2 MIMO-OFDM visible light communication employing phosphorescent LED," in *Proc. IEEE ICUFN'16*, Vienna, Austria, 2016, pp. 222–224.

[157] A. Nuwanpriya, S. W. Ho, and C. S. Chen, "Indoor MIMO visible light communications: Novel angle diversity receivers for mobile users," *IEEE J. Sel. Areas Commun.*, vol. 33, no. 9, pp. 1780–1792, Sept. 2015.

[158] F. Bohagen, P. Orten, and G. E. Oien, "Design of optimal high-rank line-of-sight MIMO channels," *IEEE Trans. Wireless Commun.*, vol. 6, no. 4, pp. 1420–1425, April 2007.

[159] M. Rahaim and T. D. C. Little, "Optical interference analysis in visible light communication networks," in *Proc. IEEE ICCW'15*, London, UK, 2015, pp. 1410–1415.

[160] A. Al-Kinani, C.-X. Wang, F. Haider, H. Haas, W. Zhang, and X. Cheng, "Light and RF dual connectivity for the next generation cellular systems," in *Proc. IEEE ICCC'17*, Qingdao, China, Oct. 2017, accepted for publication at Aug. 3, 2017.